

# Electronic Properties of Diamond Interfaces

Den Naturwissenschaftlichen Fakultäten  
der Friedrich-Alexander-Universität Erlangen-Nürnberg

zur

Erlangung des Doktorgrades

vorgelegt von  
**Florian Maier**  
aus Passau

2001

Als Dissertation genehmigt von den Naturwissenschaftlichen Fakultäten der  
Universität Erlangen-Nürnberg

Tag der mündlichen Prüfung:  
Vorsitzender der Promotionskommission:  
Erstberichterstatter:  
Zweitberichterstatter:

27. Juli 2001  
Prof. Dr. A. Magerl  
Prof. Dr. L. Ley  
Prof. Dr. Th. Fauster

*The most exciting phrase to hear in science is not “Eureka!”  
but rather, “hmm ... that’s funny ...”*

Isaac Asimov





# Contents

<b>1</b>	<b>Introduction and Motivation</b>	<b>1</b>
<b>2</b>	<b>Experimental Aspects and Characteristics of Diamond Surfaces</b>	<b>5</b>
2.1	Photoelectron Spectroscopy (PES) . . . . .	5
2.1.1	UV-induced photoelectron spectroscopy (UPS) and band structure . . . . .	9
2.1.2	X-ray induced photoelectron spectroscopy (XPS) and chemical shifts . . . . .	13
2.2	Work function measurements . . . . .	13
2.3	Low-energy electron diffraction (LEED) . . . . .	17
2.4	Hydrogen plasma treatment . . . . .	17
2.5	The three low-index surfaces of diamond - an overview . . . . .	19
2.5.1	C(111) . . . . .	19
2.5.2	C(100) . . . . .	19
2.5.3	C(110) . . . . .	20
<b>3</b>	<b>The diamond (110) surface</b>	<b>25</b>
3.1	General considerations . . . . .	25
3.2	Experimental aspects . . . . .	27
3.3	Results and discussion . . . . .	28
3.3.1	LEED investigations . . . . .	28
3.3.2	C1s core level spectroscopy . . . . .	31
3.3.3	Surface states . . . . .	33
3.4	Summary . . . . .	37
<b>4</b>	<b>Electron Affinities of Hydrogenated and Oxidized C(100) Surfaces</b>	<b>39</b>
4.1	Introduction . . . . .	39
4.2	Experimental . . . . .	41
4.3	Electron affinity of the plasma hydrogenated (100) surface . . . . .	43

4.4	Electron affinity of the chemically oxidized (100) surface . . . .	48
4.5	Summary . . . . .	55
<b>5</b>	<b>Diamond-Metal Interfaces</b>	<b>57</b>
5.1	Introduction . . . . .	57
5.2	Experimental details . . . . .	60
5.3	Results and discussion . . . . .	61
5.3.1	Gold on hydrogenated C(111) . . . . .	61
5.3.2	Magnesium on hydrogenated C(100) . . . . .	68
5.3.3	Aluminium on hydrogenated and hydrogen free diamond (111) . . . . .	75
5.4	Summary . . . . .	79
<b>6</b>	<b>Surface Conductivity of Hydrogenated Diamond</b>	<b>81</b>
6.1	General remarks concerning the surface conductivity of diamond	81
6.2	Investigation of the surface conductivity by transport measure- ments and spectroscopic methods . . . . .	83
6.3	An electrochemical model for the surface conductivity . . . . .	87
6.4	Some critical assessments of the electrochemical model . . . . .	91
6.5	Summary . . . . .	94
	<b>Summary</b>	<b>95</b>
	<b>Zusammenfassung</b>	<b>99</b>
<b>A</b>	<b>Low-threshold Electron Emission of Diamond (100)</b>	<b>105</b>
A.1	Total photoelectron yield spectroscopy and electron affinity: gen- eral remarks . . . . .	106
A.2	Total photoelectron yield spectra of the hydrogenated diamond (100) surface . . . . .	112
A.3	Total photoelectron yield spectra of the chemically oxidized di- amond (100) surface . . . . .	117
A.4	Summary . . . . .	120
	<b>Bibliography</b>	<b>121</b>

# Chapter 1

## Introduction and Motivation

In the current situation of our information society which is mainly based on silicon technology, new requirements in high speed and high power devices open the field for wide-band gap semiconductors like SiC or GaN. Due to the large band gap of 5.47 eV, its high carrier mobilities of 1000-2000 cm<sup>2</sup>/Vs for electrons and holes and its high breakdown field strength up to 10 MV/cm, diamond seems to be highly suitable for high power and high frequency applications working even at elevated temperatures where conventional semiconductors fail [1]. In addition, the combination of its unique high thermal conductivity, chemical inertness, and mechanical hardness provide further prospects for diamond applications [1–3].

A boom of activities in the field of diamond started in the late seventies with the development of low-pressure synthesis of diamond by *Chemical Vapor Deposition* (CVD) techniques. An historical overview in CVD is provided for example in Ref. [4]. In contrast to former high-pressure and high-temperature (HPHT) diamond synthesis the CVD process provides a relatively cheap way of depositing diamond films on a large variety of different substrates [1]. The application of diamond for electronic devices requires high quality films with atomically flat surfaces, low defect densities, and controlled doping levels [5]. Concerning crystal quality considerable success has been achieved for homoepitaxial films grown on HPHT diamond substrates [5]. State-of-the-art heteroepitaxial CVD films grown on (100) oriented silicon substrates were recently realized in our group by Janischowsky and co-workers [6, 7] by a combination of microwave and hot-filament assisted techniques. These films exhibit very smooth surfaces of closely packed and highly oriented (100) crystallites. Within a lateral extension over several mm<sup>2</sup>, these high quality CVD films show very

few grain boundaries and (111) facets, are virtually free of nondiamond carbon phases as judged by Raman spectroscopy, and are thus ideal substrates for further device fabrication. Fig. 1.1 depicts a Secondary Electron Micrograph (SEM) of one of those high-quality CVD films.

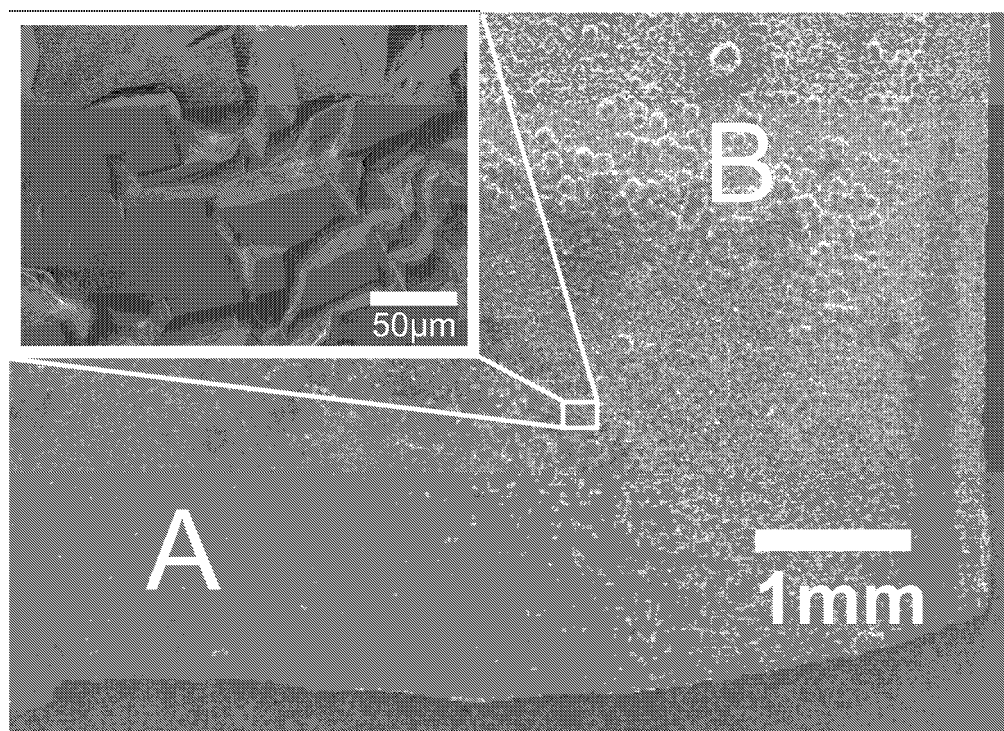


Figure 1.1: Secondary electron micrograph of a high-quality CVD diamond film grown on Si (100). Whereas region B is still of polycrystalline nature, the number of grain boundaries is considerably reduced in region A, and this part of the film exhibits electronic surface properties that are virtually indistinguishable from single crystal diamond surfaces. The insert shows the transition region where the small crystals start to grow together.

With respect to doping of diamond, a shallow donor is still missing; however, there are recent publications concerning phosphorus [8] and sulphur [9, 10] with promising n-doping properties. But those preliminary results still need further confirmation. The only acceptor dopant so far achieved is substitutional boron. Despite a fairly large activation energy of 0.36 eV, unipolar devices based on boron doping are already fabricated on homo- and heteroepitaxial CVD films such as Schottky diodes and field effect transistors working up to several hundred degree Celsius ([11] and references therein).

Moreover, a second type of conductivity exist for diamond which is unique among all known semiconductors: the surface conductivity of hydrogenated

diamond. Despite the fact that undoped diamond with a band gap of 5.47 eV is an excellent insulator even up to 2000°C, both, hydrogen terminated single crystals and CVD films exhibit a fairly high p-type surface conductivity at room temperature which is of the order of  $10^{-6}$  to  $10^{-4}$  A/V. First reported by Landstrass and Ravi in 1989 [12, 13], and investigated over the years [14–21], this unusual property is not completely understood. Carrier mobilities from Hall measurements range between  $30 \text{ cm}^2\text{V}^{-1}\text{sec}^{-1}$  and up to  $400 \text{ cm}^2\text{V}^{-1}\text{sec}^{-1}$  [20] and are thus comparable to those measured for boron doped diamond. Hence, there is general agreement that the conduction is carried by holes with a density in the range of  $10^{12} - 10^{13} \text{ cm}^{-2}$  residing in an accumulation layer right at the surface or extending into the bulk at maximum a few tens of nanometers [22]. The nature and the depth distribution of the corresponding acceptors is still controversially discussed [18, 23, 24]; in particular, the relationship between surface conductivity of diamond and hydrogenation is still under debate. The conductivity of the surface layer can even be controlled by a gate and thus forms the basis of a special kind of field effect transistors [25, 26]. These MES-

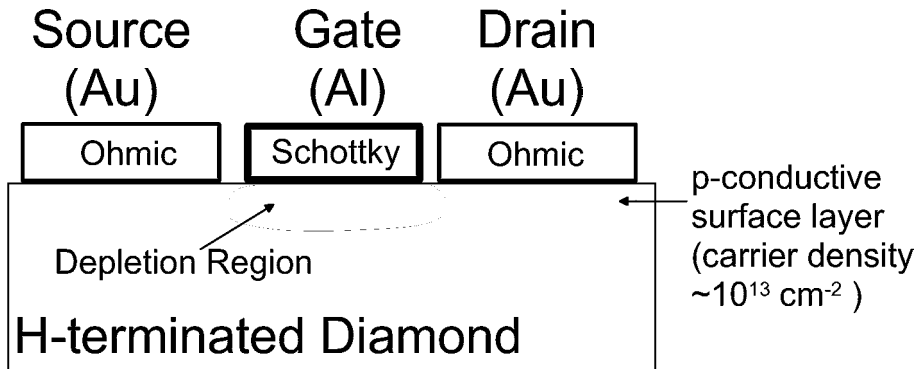


Figure 1.2: Layout of a MESFET device based on hydrogen terminated diamond (taken from Ref. [27]). Both, source and drain electrodes are obtained by evaporated gold exhibiting ohmic contacts on the hydrogenated diamond surface. The MESFET is driven in an enhancement mode - i.e. a depletion layer is formed at zero gate bias.

FETs operate with ohmic gold contacts as source and drain electrodes whereas the charge carrier density in the surface channel is controlled by the gate voltage. Since the surface accumulation layer is very thin, the depletion region that forms at zero gate bias for gate materials such as aluminium which exhibit a large Schottky Barrier Height (SBH) of  $0.8 \pm 0.1$  eV on hydrogenated diamond has already closed off the conducting channel. Hence, the transistor works in the enhancement mode [27]. This is shown in a schematic cross section view in Fig. 1.2. By the use of gate materials which exhibit low SBHs on hydrogenated diamond, the device can be driven into the depletion mode of operation as well [27]. The latter is also achieved for metal-insulator-semiconductor (MIS)

structures [28]. The MESFETs exhibit a transconductance of 0.11 A/(V mm) which is comparable to that of Si-nMOSFETs with similar gate lengths. Cut-off frequencies up to 2.2 GHz [28] demonstrate the capability of these diamond MESFETs in the field of high-frequency applications.

Furthermore, it is shown by Denisenko *et al.* [29] that the gate electrode of the MESFET can even be replaced by an electrolyte that controls the surface channel by the  $pH$ -value of the solution. In conjunction with the chemical inertness of diamond, these kind of devices are promising  $pH$ -sensors in the enormously growing field of bio-chemistry [30].

The surface-channel diamond MESFET can be considered as a leitmotif to the forthcoming chapters of this thesis. They deal with structural and electronic properties of diamond interfaces involved in the MESFET device. The experiments are carried out by surface sensitive techniques that are outlined in the first chapter. Since many different aspects of interface properties are considered here, the second chapter starts with the surface itself which represents the “natural” interface of the bulk material with vacuum. Therefore, the investigations on diamond (110) introduce the reader to the type of experiments performed. The influence of adsorbates on the electron affinity of diamond surfaces is presented in the following chapter. It will be shown for the hydrogenated and the oxidized (100) surface that diamond exhibits a large variation in electron affinity which is unknown for any other semiconductor. The electron affinity plays a decisive role for the formation of Schottky and ohmic contacts of metals in contact with a semiconductor. In Chapter 5, the role of hydrogen at the metal-diamond interface is thus investigated in the case gold, magnesium, and aluminium on hydrogenated and hydrogen free diamond surfaces. In the final chapter, the high surface conductivity of hydrogenated diamond is elucidated by a combination of spectroscopy and transport experiments. It will be shown that hydrogen termination is a necessary but not sufficient condition to obtain the high surface conductivity. Additionally, unknown adsorbates from the atmosphere are needed. On the basis of these results an electrochemical model is developed which can explain the effect of hydrogen termination and also shows why diamond is the only semiconductor with this p-type surface conductivity. Finally, a short chapter on the electron emission properties of diamond (100) single crystal surfaces with respect to the electron affinity of the surface round out this thesis.

## Chapter 2

# Experimental Aspects and Characteristics of Diamond Surfaces

This chapter is a short introduction in the experimental techniques used throughout this thesis. Further information that focuses on details is provided in the individual chapters. In addition, a good introduction in surface analysis techniques is given by Henzler and Göpel [31], Woodruff and Delchar [32], and Ertl and Küppers [33]. In the last part of this chapter a short description of the three low-index diamond surfaces that are of relevance here is presented.

### 2.1 Photoelectron Spectroscopy (PES)

A thorough description of PES is provided by Cardona and Ley [34], and Hüfner [35]. PES is based on the external photoeffect [36]. By the absorption of a photon an electron is expelled from an occupied electronic state into the vacuum. The energy of the impinging photon can be in the ultraviolet regime (UPS:  $h\nu \approx 5\text{-}100$  eV), in the soft X-ray regime (SXPS:  $h\nu \approx 100\text{-}1000$  eV), or in the X-ray regime (XPS:  $h\nu \geq 1000$  eV). Due to the short escape depth  $\lambda_e$  of excited electrons which do not suffer from energy losses this technique probes the very first atomic surface layers of  $3\text{\AA}$  up to about  $20\text{\AA}$  [35] thicknesses. The highest surface sensitivity is achieved for excited electrons of about 50 eV kinetic energy. Lower or higher kinetic energies  $E_{kin}$  increases the PES probe depth.

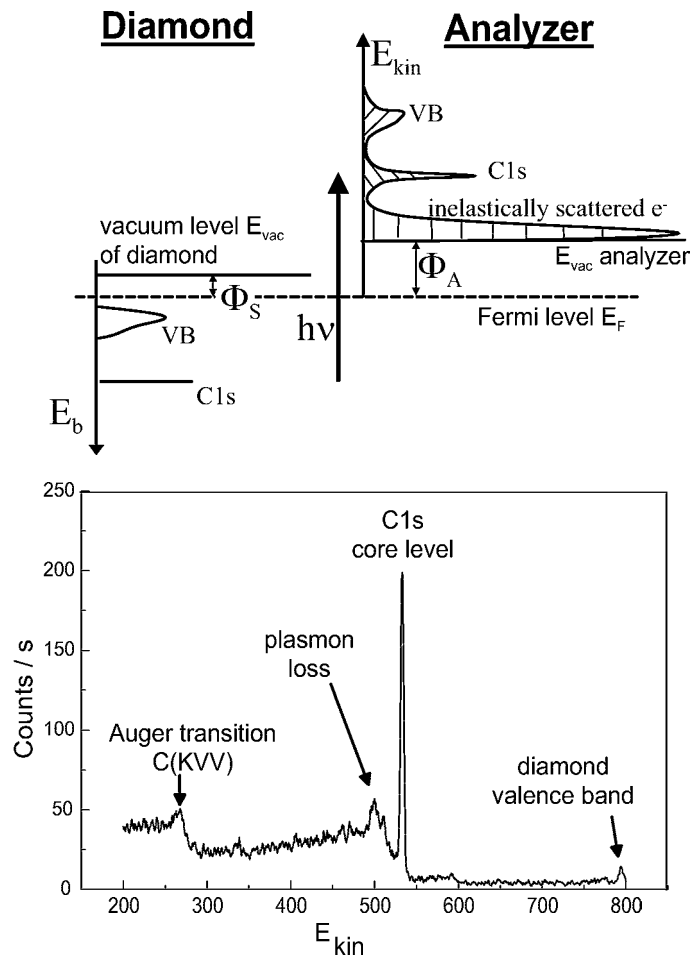


Figure 2.1: Top: Scheme of the photoemission process. An electron with a binding energy  $E_b$  of the valence band (VB) or the C1s core level in diamond is excited by a photon with an energy  $h\nu$  into the vacuum. The photoemission current is recorded as a function of the kinetic energy  $E_{kin}$  as measured with respect to the vacuum level of the electron analyzer. Bottom: Photoemission spectrum of diamond taken at 800 eV photon energy. In addition to the valence band and the C1s core level of diamond, loss features (such as plasmon excitations) and Auger transitions are visible.



From the difference between photon energy  $h\nu$  and electron kinetic energy  $E_{kin}$ , the initial binding energy  $E_b$  is extracted as follows

$$E_b = h\nu - E_{kin} - \Phi_A \quad (2.1)$$

where  $\Phi_A$  is the work function of the electron analyzer. In the case of PES of solid states the natural reference in binding energy is the common Fermi level  $E_F$  of the sample and the analyzer as shown in Fig. 2.1, provided that charging does not occur.

Recording not only the kinetic energy but the angular distribution of electrons emitted from the valence band provides an access to the initial wave vector  $\underline{k}$  of the electronic states as shown in the next section. Thus, angle-resolved valence band spectroscopy (ARUPS) is commonly used for band mapping of occupied states.

For laboratory photon sources like plasma discharges and X-ray sources the excitation energy  $h\nu$  is fixed and the photocurrent is recorded as a function of kinetic energy. In contrast to these so-called *energy distribution curves* (EDC), a synchrotron light source provides the possibility of changing the photon energy simultaneously to the kinetic energy of the electron transmitted through the analyzer in such way that the initial state which is characterized by  $E_b$  (Eq. 2.1) remains constant. This *constant initial state* (CIS) mode was used for the determination of the valence band maximum relative to  $E_F$  as shown below.

The band alignment of a semiconductor with respect to the Fermi level  $E_F$  at the surface is decisive for all electronic properties that involve charge transport at the semiconductor's surface or interface [37]. Since the band positions relative to  $E_F$  are determined in the bulk by doping and temperature, the energy position of electronic states at the surface is mainly a function of the density of surface states and interface states. The surface states are either formed by valence electrons of surface atoms of a perfectly ordered semiconductor surface (=intrinsic surface states) or originate from surface defects (=extrinsic surface states); interface states can be formed when the surface of the semiconductor is in junction with another material (an example are metal-induced gap states [37]). With the aim of a common Fermi level between bulk and surface in thermal equilibrium, electrons are exchanged between these surface/interface states and bulk states as long as the chemical potential, i.e. the Fermi level, is inhomogeneous. In thermal equilibrium, a space charge  $\rho(z)$  is established; the related electrostatic potential energy  $U(z)$  shifts all electronic states of the semiconductor with respect to  $E_F$  depending on the position  $z$  below the surface. This process is the so-called "surface band bending" and - as sketched Fig. 2.2 - includes all characteristic electronic levels such as the valence band maximum, the conduction band minimum, characteristic bulk and surface states and also core level states (such as the C1s core level of carbon). By

any modification of the semiconductor's surface, the density of surface states can also be changed yielding a change in surface band bending. Due to the

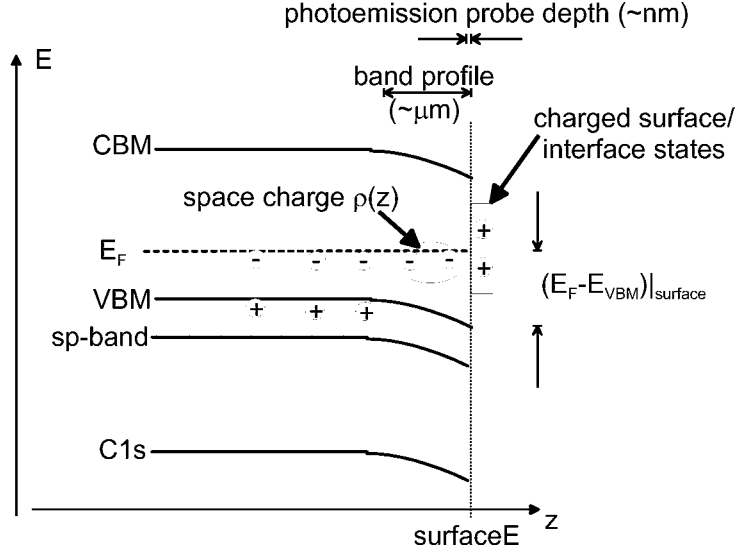


Figure 2.2: Scheme of downward band bending at the surface of p-type diamond. The exchange of charge transfer between bulk states and states located at the surface yields a space charge (negative excess charge in the boron acceptor levels) region in diamond (about 200 nm in depth) that is compensated by an excess charge (positive) in the surface states. Within the space charge region, all electronic levels of diamond relative to the Fermi level  $E_F$  are position dependent such as the valence band maximum (VBM), the conduction band minimum (CBM), the  $sp$ -band within the valence band, and the C1s core level of diamond, respectively (see next sections). On account of the short mean free path of electrons (3-20Å), photoemission only probes the energy (relative to  $E_F$ ) of these states right at the surface.

short mean free path of electrons which is orders of magnitude smaller than the band profile extension in diamond [38], PES provides a direct method for the investigation surface band bending. As it is shown in Fig. 2.2, **changes** in surface band bending during an experiment can be traced by any characteristic feature of the valence band or by the C1s core level of diamond, respectively. To quantify surface band bending, the difference in energy  $E_F - E_{VBM}$  between the valence band maximum (VBM) and the Fermi level  $E_F$  at the surface will be quoted throughout this thesis.

### 2.1.1 UV-induced photoelectron spectroscopy (UPS) and band structure

The investigation of valence band states by photoemission has a long and successful history [34, 35]. Here, the conceptional separation of the photoemission (PES) process in (i) optical excitation of the electron in the bulk, (ii) transport of the electron to the surface, and (iii) transmission of the electron from the solid into free space is sufficient for the interpretation of our data; commonly this model is known as *three-step-model* [34]. The absorption of a photon of energy  $h\nu$  leads to an interband transition between an occupied state 1 that is characterized by its initial state energy  $E_1(\underline{k}_1)$  and an unoccupied state 2 with  $E_2(\underline{k}_2)$ . In the photon energy range of UPS the wave vector of the incident photon can be neglected compared with the electron wave vectors  $\underline{k}_i$  and thus

$$\underline{k}_1 = \underline{k}_2 \quad \text{modulo a reciprocal lattice vector } \underline{G}. \quad (2.2)$$

All transitions that fulfill Eq. 2.2 and energy conservation

$$E_i - E_j = h\nu \quad \forall \text{occupied, } j \text{ empty states} \quad (2.3)$$

occur with a certain probability  $w_{i,j}(h\nu)$ <sup>1</sup>.

On the way to the surface, the vast majority of excited electrons lose their kinetic energy mainly by electron-electron interactions [35]: it is these loss processes that determine the short mean free path of electrons in the range of 3 – 20 Å, and thus provide the surface sensitivity of photoemission.

Finally, the electron escapes into the vacuum (third step). In the case of a well-ordered crystalline surface the wave vector component parallel to the surface  $k_{\parallel}$  is conserved for this step due to the in-plane translational symmetry of the surface [34]

$$\underline{k}_{2,\parallel}^{\text{outside}} = \underline{k}_{2,\parallel}^{\text{inside}} \quad \text{modulo a reciprocal vector of the surface lattice.} \quad (2.4)$$

The wave vector component in normal direction  $k_{\perp}$  is, however, changed by the potential step at the surface. From the measured kinetic energy  $E_{kin}$  and polar angle  $\vartheta$  relative to the surface normal, the length of the parallel wave vector along one azimuthal direction is derived for free electrons as follows

$$k_{\parallel} = \sqrt{\frac{\hbar^2}{2m_0} \cdot E_{kin}} \cdot \sin\vartheta = 0.516 \text{Å}^{-1} \cdot \sqrt{E_{kin}/\text{eV}} \cdot \sin\vartheta. \quad (2.5)$$

$\hbar$  and  $m_0$  are the Planck's constant divided by  $2\pi$  and the rest mass of the electron, respectively. The initial state energy of surface states does not depend

---

<sup>1</sup>The question of UPS intensities is not directly related to band mapping and is thus not discussed further. It should be mentioned that symmetry selection rules that provide vanishing transition probabilities  $w$  are very useful for extracting symmetry properties of the electronic states involved.

on  $k_{\perp}$  and therefore, the surface band structure  $E_i(k_{\parallel})$  is directly mapped by ARUPS using Eqs. 2.1 and 2.5, as will be demonstrated in Chapter 3. Due to the lack of  $k_{\perp}$  conservation during the PES process, additional knowledge concerning  $E(k_{\perp})$  is required in general to determine the band structure of bulk states. In Fig. 2.3 the bulk band structure along the high symmetry lines of the Brillouin zone is shown as calculated by Painter *et al.* [39].

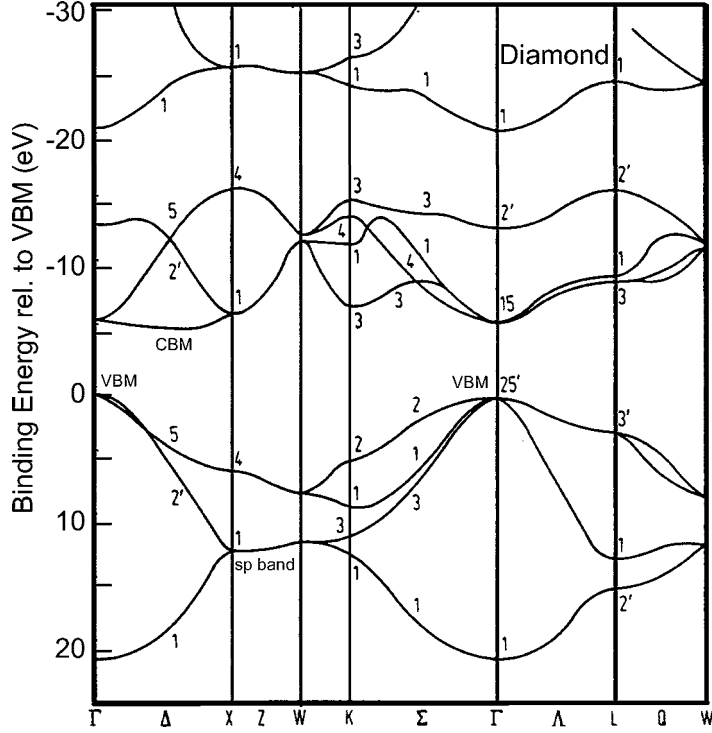


Figure 2.3: Bulk band structure of diamond as taken from Ref. [39] (for details, see text).

It was pointed out in the previous section that the difference between the energy position  $E_{VBM}$  of the VBM and the Fermi level  $E_F$  at the surface of a semiconductor is a function of corresponding surface state densities. Changes in surface state density (e.g. in a desorption experiment) may result in a different surface band bending. In principle, surface band bending can be immediately drawn from the binding energy of the VBM ( $E_F - E_{VBM}$  at the surface) measured with UPS on account of the short electron escape depth. In UPS, the position of the VBM is commonly estimated by the energy cut-off at high kinetic energies of energy distribution curves (EDCs) taken for an arbitrary excitation photon energy  $h\nu$ . However, this estimation only holds true for a well-ordered surface if transitions between the VBM as initial state  $i$  and unoccupied final states  $j$  do indeed occur, i.e. energy conservation (Eq. 2.3) and wave vector

conservation (Eq. 2.4) are fulfilled simultaneously. As it is demonstrated in Fig. 2.4a), the two spectra of a hydrogenated diamond (100) surface taken at 40 eV and 60 eV photon energy are considerably different in shape in the range of 0 eV and 3 eV binding energy, i.e. in the range of the VBM; in particular, an accurate estimation of the VBM position from the energy cut-off of the 60 eV-spectrum is not possible. Approximately, the minimum uncertainty in  $E_{VBM}$  as measured by the spectral cut-off amounts to  $\pm 0.3$  eV in the case of diamond.

As it was sketched in Fig. 2.2, the **relative** changes in  $E_F - E_{VBM}$  and thus in surface band bending can be traced with an accuracy of  $\pm 0.05$  eV determining the binding energy of characteristic valence band features of diamond in UPS or of the C1s core level in XPS, respectively. In UPS experiments on diamond (100), the sharp peak that is labelled “sp-peak” in Fig. 2.4a) was used for this purpose. This peak is located about 13 eV below the VBM and originates from the lowest p band and the s band which are degenerated between X and W [40]. It is thus referred to as “sp-band” (see Fig. 2.3 as well). For exciting photon energies between 50 eV and 100 eV the sp-peak exhibits no dispersion with emission angle; however, the spectra taken at 40 eV photon energy reveals a binding energy of the sp-peak that is 0.17 eV higher than measured at higher photon energies. This has to be taken into account when using HeII light ( $h\nu = 40.8$  eV).

To obtain **absolute** values for  $E_F - E_{VBM}$ , the binding energy of VBM (relative to  $E_F$ ) and the constant energy separation  $E_{VBM} - E_{sp-peak}$  for a fixed photon energy between VBM and the sp-peak was derived in a single calibration experiment as follows using angle-resolved constant initial state (CIS) spectroscopy (for details, see also Ref. [41]). In a first step, the binding energy of the VBM of a hydrogenated diamond (100) sample was deduced from the high energy cut-off of a conventional EDC yielding a value of 0.86 eV for  $E_F - E_{VBM}$ . In a second step, a whole series of CIS spectra were recorded between 22 eV and 44 eV photon energy for different initial state energies  $E_i$ . Starting with  $E_F - E_i = 0.86$  eV (spectrum a in Fig. 2.4b),  $E_i$  was changed in steps of 0.1 eV towards the Fermi level, i.e. towards the VBM. When  $E_i$  approached  $E_{VBM}$ , the intensity drastically dropped (spectra d-g in Fig. 2.4b) reflecting the decrease in density of initial states. Taking the finite energy resolution of our analyzer into account ( $\pm 0.15$  eV) spectrum e was in concordance with  $E_i = E_{VBM} \pm 0.08$  eV. In addition to the drop in intensity, the angular distribution of photoelectrons excited from  $E_F - E_i = 0.46$  eV showed the characteristic emission only in direction normal to the surface. Right at  $E_i = E_{VBM}$ , direct transitions occur at one point in the Brillouin zone, namely at the  $\Gamma$  point (see Fig. 2.3). Therefore, only transitions account for the corresponding CIS spectrum with  $k_{\parallel} = 0$  (remember  $k_{\parallel}$ -conservation in UPS, as given by Eq. 2.4!). Hence, photoelectrons are only emitted in the direction

normal to the surface normal at  $E_i = E_{VBM}$  which was indeed observed for spectrum *e*. In a final step, a conventional EDC was recorded with 40 eV and 60 eV photon energy for the same sample to obtain the binding energy of the sp-peak relative to  $E_F$ . With  $E_F - E_{VBM}$  from the CIS calibration and  $E_F - E_{sp-peak}$  from the EDC spectrum, an energy separation  $E_{VBM} - E_{sp-peak}$  of  $12.8 \pm 0.1$  eV for  $h\nu = 40$  eV and  $12.63 \pm 0.1$  eV for  $h\nu = 60$  eV was derived.

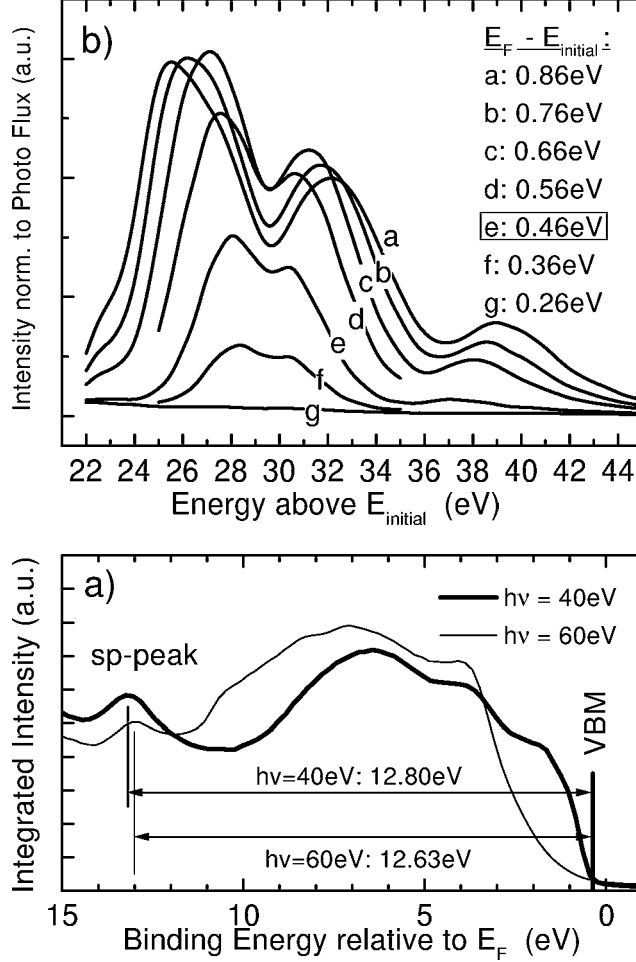


Figure 2.4: a) Angle integrated EDCs of C(100)-(2x1):H (azimuth [011]) taken at 40 eV (bold line) and 60 eV (thin line) photon energy. The energy difference of the sp-peak to VBM equals 12.80 eV for the 40 eV spectrum and 12.63 eV for the 60 eV spectrum, respectively. b) Constant initial state (CIS) spectra of hydrogenated diamond (100) as a function of initial state energy  $E_i$ . Spectrum *e* at  $E_F - E_i = 0.46$  eV corresponds to the CIS spectrum recorded with  $E_i = E_{VBM}$  (for details, see text).

## 2.1.2 X-ray induced photoelectron spectroscopy (XPS) and chemical shifts

In principle, X-ray induced PES (XPS) also provides a possibility for band mapping. However, due to the finite acceptance angle  $\Delta\vartheta$  of the electron analyzer the uncertainty in wave vector  $\Delta k_{\parallel}$  increases by the square root of the kinetic energy (Eq. 2.5) and thus by the exciting photon energy (Eq. 2.1). For typical XPS setups, the  $k$ -broadening is in the order of the Brillouin zone (BZ) dimensions and the measured spectra are thus strongly dominated by the density of states and not by direct transitions between energy bands at one  $k$ -point of the BZ [35]. In addition, the cross sections for valence band excitation drastically decrease with increasing photon energy [42], making XPS a very time-consuming method for valence band characterization.

XPS is thus used within this work to investigate core levels (in addition to the literature mentioned above, a good introduction in core level spectroscopy by means of XPS is provided by Egelhoff [43]). Due to the high photon energies (1486 eV in the case of Al  $K_{\alpha}$  X-ray sources), higher binding energies of core levels become accessible in XPS than in the case of UPS. By their characteristic series of core level binding energies, different elements and thus the chemical composition of the surface can easily be identified. Furthermore, the core level binding energies of an atom depend slightly on the surrounding charge distribution. For inequivalent sites these *chemical shifts* provide information concerning bonding partners of the atom of interest. In this context, XPS is also known as *electron spectroscopy for chemical analysis* (ESCA).

In addition to ESCA on diamond surfaces, XPS was used in this work to trace changes in surface band bending and to measure  $E_F - E_{VBM}$ . The energy difference  $E_{VBM} - E_{C1s}$  was obtained from the binding energy of the C1s core level ( $=E_F - E_{C1s}$ ) measured with XPS and from the binding energy of the sp-peak ( $=E_F - E_{sp-peak}$ ) measured with UPS in a single experiment. From  $E_{VBM} - E_{sp-peak} = 12.80 \pm 0.08$  eV as deduced in the preceding section,  $E_{VBM} - E_{C1s}$  amounted to  $283.9 \pm 0.1$  eV.

## 2.2 Work function measurements

A fundamental surface property of a solid is the work function  $\phi$ . In the case of metals,  $\phi$  can be defined as the minimum energy required (at T=0 K) to remove an electron from the bulk and bring it sufficiently far away from the surface. The final (potential) energy of this electron is then called the vacuum level  $E_{vac}$ . It is evident from this definition that  $\phi$  plays a decisive role in all processes that involve electron emission or electron transfer reactions that occur in the vicinity of interfaces and  $\phi$  is thus a major topic of this thesis. Despite the simple definition of  $\phi$ , work functions are difficult to calculate theoretically

and to measure experimentally [34, 44]. The first problem arises already from the term “sufficiently far away from the surface”. On the one hand, this means that the electron position is at a distance from the surface where the energy of the electron at  $E_{vac}$  becomes position independent. On the other hand, the vacuum level depends on the crystallographic orientation and the structure of the surface as seen in the following. Therefore, the electron’s position should be located close enough to the surface to account for these effects.<sup>2</sup>

Considering the definition of  $\phi$  more precisely,  $\phi$  represents the energy difference between two equilibrium states. In the initial state, the neutral crystal contains  $N$  electrons in its ground state with an energy  $E_N$ . In the final state, one electron is removed from the crystal to the state  $E_{vac}$ ; the crystal with its remaining  $N-1$  electrons is characterized by a final ground state  $E_{N-1}$ , and the work function is thus calculated to

$$\phi = (E_{N-1} + E_{vac}) - E_N = E_{vac} + (E_{N-1} - E_N). \quad (2.6)$$

$E_N - E_{N-1}$  is the electrochemical potential for electrons, namely the well-known Fermi energy  $E_F$ , and thus Eq. 2.6 can be written such as [44]

$$\phi = E_{vac} - E_F. \quad (2.7)$$

The truncation of the bulk yields in general a different charge distribution at the surface compared to that in the bulk. Due to the finite density of states of metals at  $E_F$ , these surface charges are screened by electrons within fractions of interatomic distances [45]. The related surface dipole layer modifies the potential energy. For conceptual reasons, one can thus subdivide the work function  $\phi$  in a surface dependent part  $\Delta\phi$  and a surface independent part  $\phi_{bulk}$ . Hence,  $\phi_{bulk}$  is considered as the minimum energy required for an electron at the Fermi energy  $E_F$  to leave the bulk if the potential  $U(z)$  remains unchanged at the surface as shown in Fig. 2.5. It is  $\Delta\phi$  that accounts for the different work functions of different surfaces of the same metal due to the crystallographic surface configuration.

To describe the change of potential energy between bulk and surface in the case of a semiconductor, not the work function  $\phi$  but the electron affinity  $\chi$

$$\chi := E_{vac} - E_{CBM} \quad (2.8)$$

and the ionization energy  $I$

$$I := E_{vac} - E_{VBM} \quad (2.9)$$

---

<sup>2</sup>It is plausible that all differences due to local surface structures are smoothed out when the electron is brought to infinity from the solid, and one may define one single vacuum level  $E_{vac,\infty}$  in this case. Therefore, one has to consider carefully the length scales under investigation and the sensitivity to microfields of the particular method used for work function measurements



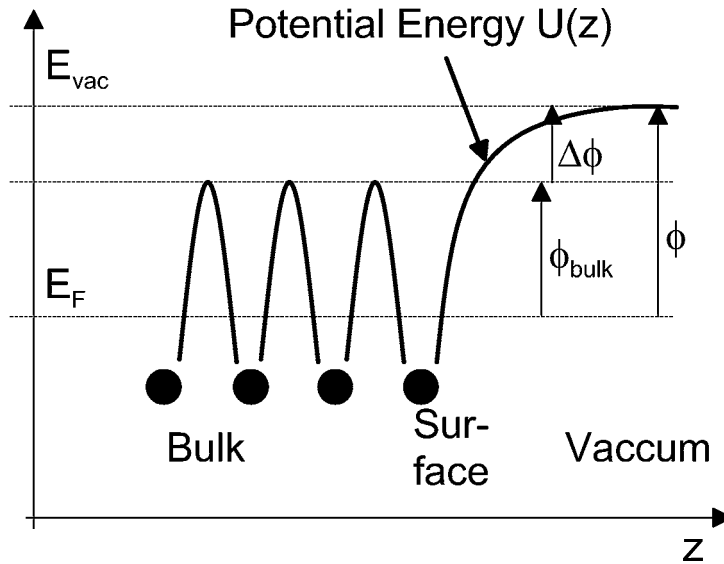


Figure 2.5: Schematic representation of the electrostatic potential energy  $U(z)$  near a metal surface in direction normal to the surface. The filled circles represent the atomic positions near the surface (for the definition of the energies shown, see text).

are the decisive parameters ( $E_{vac}$ ,  $E_{CBM}$ , and  $E_{VBM}$  are the energy positions of the vacuum level and of the band edges at the surface, respectively). Since  $I$  and  $\chi$  only differ from each other by the constant gap energy  $E_g$ , the following discussion is restricted to the electron affinity  $\chi$ . As it was discussed for the work function of metals,  $\chi$  can be subdivided into a bulk contribution  $\chi_{bulk}$  that characterizes the situation in the bulk and in a surface contribution  $\Delta\chi$  which takes the different charge distribution at the surface compared to that in bulk into account. Hence, the diagram shown in Fig. 2.5 describes the situation for semiconductors as well when  $\phi$  is replaced by  $\chi$  and  $E_F$  by  $E_{CBM}$ . Adsorbates bonded to the surface can induce charge displacements between the surface atoms of the semiconductor and the adsorbate within the bond length and thus modifies  $\Delta\chi$ ; the magnitude of the corresponding surface dipole layer depends mainly on the differences in electronegativity of the adsorbed atoms and of the semiconductor atoms as will be shown in Chapter 4 for hydrogen and oxygen terminated diamond (100).

It was emphasized in the previous sections that the density of (free) surface states can induce surface band bending by the in-built potential  $U(z)$ . Hence, to determine  $\chi$  of a semiconductor from its work function  $\phi$  that is defined by Eq. 2.7, one has to determine the energy positions of the band edges relative to  $E_F$  at the surface as well. The relevant quantities are summarized in Fig. 2.6.

There are numerous experimental ways of measuring  $\phi$  [34]. One of the most common and also most precise methods is the Kelvin method. It is based

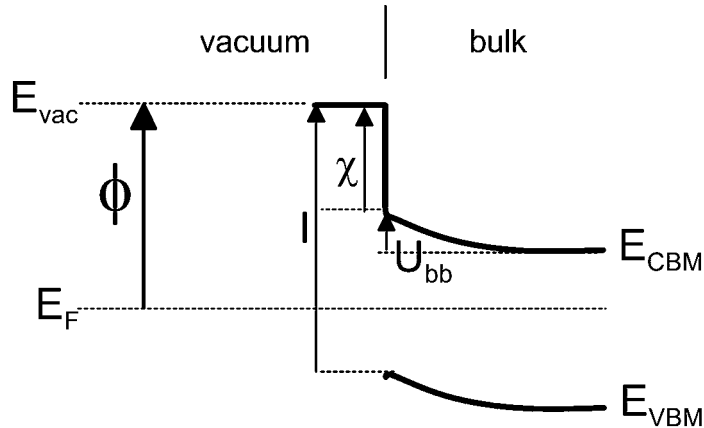


Figure 2.6: Work function  $\phi$ , ionization energy  $I$ , and electron affinity  $\chi$  of a semiconductor.  $U_{\text{bb}}$  represents the energy difference between the band edge positions in the bulk and at the surface on account of surface band bending.

on the contact potential difference (CPD) that exists between the surfaces of two materials when the corresponding Fermi energies of two connected conductors line up in equilibrium. The CPD is the difference in the corresponding workfunctions:  $CPD = \Delta\phi/e$ . For Kelvin probe measurements the surface of interest and the Kelvin probe form the plates of a condenser. The distance between these plates is varied periodically, and thus varies the capacitance  $C$  of the condenser. The induced current  $I(t) = \frac{dC}{dt} \cdot (CPD + U_{\text{comp}})$  is zero for any time  $t$  if the additional compensation voltage  $U_{\text{comp}}$  applied to the condenser plates equals the negative CPD. By this method, values of  $\Delta\phi$  averaged over the probe area are measured within an accuracy of a few meV [34]. In our experiment, the **absolute** work function of the probe is independently derived *in situ* from total photoelectron yield spectroscopy (TPYS) as proposed by Fowler [46]. He showed that the total photoyield of metals which equals the photocurrent per incident photon of energy  $h\nu$  is a universal function  $F(\phi_{\text{metal}} - h\nu)$ . On a logarithmic scale as depicted in Fig. 2.7 the Fowler function  $F$  is adapted to the measured yield spectrum of a gold reference film by a rigid shift of  $F$  in x- and y-direction, i.e. a shift in photon energy and in amplitude, respectively. The shift in photon energy thus provides the **absolute** value for  $\phi$  of the reference and of the work function of the Kelvin probe, respectively. By the combination of CPD and TPYS measurements the work function of the sample surface is obtained with an overall uncertainty in  $\phi$  of  $\pm 0.02$  eV.

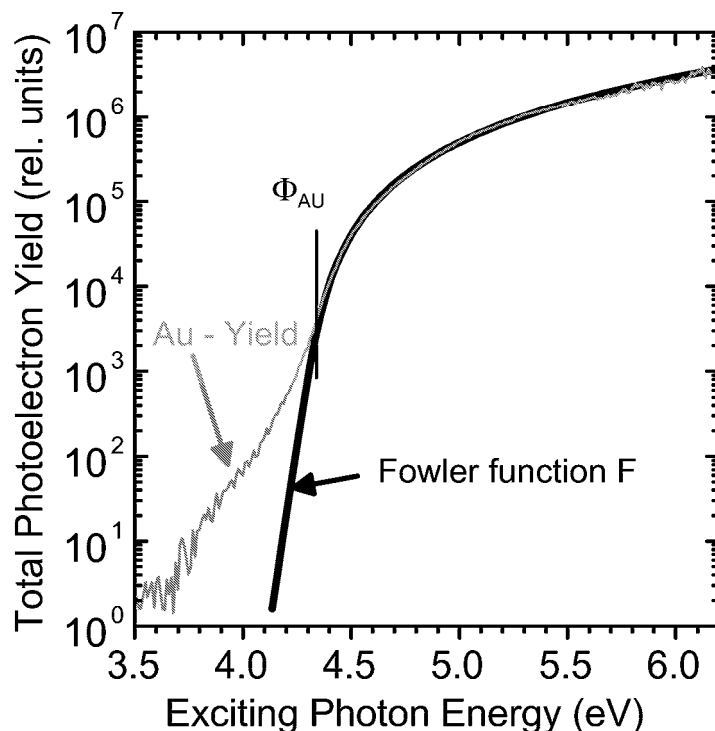


Figure 2.7: Total photoelectron yield spectrum (TPYS) from a gold reference (gray). The best coincidence with the Fowler function (black) is obtained for  $\phi_{Au} = 4.33$  eV (the TPYS experiments are carried out in the range of 2-6 eV photon energy using a setup that is described in detail in [47]).

## 2.3 Low-energy electron diffraction (LEED)

The diffraction of monochromatic electrons with low kinetic energy (30-300 eV) is a standard technique in surface analysis [33, 48]. Due to the short inelastic scattering length in this energy range, electrons are diffracted by the very first atomic layers only. In this work, LEED was used qualitatively as a tool to judge structural surface properties such as crystallographic surface orientation, surface reconstruction, and long-range surface order.

## 2.4 Hydrogen plasma treatment

Surface sensitive experiments such as UPS for valence band spectroscopy and LEED require “ideal” surfaces that exhibit long-range order. The investigation of diamond surfaces has been an obstacle for a long time due to the difficulty of surface preparations. Sputtering and annealing failed in the case of diamond because they led to a graphitization of the surface. Mechanically

polished surfaces were highly surface disordered as witnessed by high diffuse background intensity in LEED. In addition, the weak (1x1) LEED diffraction spots observed on polished diamond samples only reflected the symmetry of the underlying bulk material. Neither bulk nor surface states showed a dispersion with electron emission angle in ARUPS and only density of states was observed [49]. A breakthrough in surface preparation has been achieved with “hydrogen plasma polishing”. First observed by Thoms *et al.* [50] and Küttel *et al.* [51] the exposure of the surface to a microwave hydrogen plasma led to smooth and well-ordered surfaces that were terminated by hydrogen. The plasma conditions were very similar to those applied during microwave assisted CVD growth except for the lack of the carbon containing gas.

In this work, the mechanically polished diamond surfaces were exposed to the plasma at a partial hydrogen pressure of 50 mbar and a substrate temperature of  $800 \pm 50^\circ\text{C}$ . In the case of (111) and (100) oriented samples, the plasma treatment took 5-10 minutes whereas the duration was restricted to 3-5 minutes in the case of C(110) (see Chapter 3). These “plasma treated” diamonds might even be stored for a long time in ambient atmosphere without losing the hydrogen termination as witnessed by high resolution electron energy loss spectroscopy (HREELS) [52] and multiple internal reflection infrared spectroscopy [53]. After introduction in UHV and annealing at moderate temperatures ( $500^\circ\text{C}$ ), the surfaces were free of contaminants as measured by XPS [54] and HREELS [52]. In contrast to mechanically polished surfaces, typical LEED diffraction pattern of the plasma treated diamond surfaces showed bright reflexes with virtually no background intensity and in the case of diamond (100) a 2x1-reconstruction. Moreover, dispersion of occupied bulk states with photon energy and with emission angle were observed in angle-resolved UPS experiments on hydrogenated diamond [55, 56]. Both, LEED observations and ARUPS demonstrated that the long-range order of the plasma treated surface was within the coherence length of LEED and ARUPS ( $\approx 100$  nm [33]). Recently, scanning tunneling microscopy (STM) revealed in a temperature-dependent etching study [57] that atomically flat diamond (100) surfaces were indeed obtained at conditions similar to the plasma conditions used in this work.

## 2.5 The three low-index surfaces of diamond - an overview

Because the (100) and (111) oriented diamond surfaces have been thoroughly discussed by Graupner [40] and by Ristein [58], only a short overview is presented in this section.

The diamond lattice that is formed by the carbon atoms of the crystal consists of two interpenetrating face-centered cubic Bravais lattices which are displaced along the body diagonal of the conventional cubic cell by one quarter the length of the diagonal [45] (the lattice constant  $a$  of the conventional cubic cell is 3.567Å).

### 2.5.1 C(111)

The bulk terminated (111) surface can exhibit either one or three dangling bonds. Due to the high formation energy of breaking three bonds, only the (111) one-dangling bond surface is observed [59] which is the natural cleavage plane of diamond (Fig. 2.8a,b). The unreconstructed C(111) surface is obtained after plasma treatment where the single bonds are passivated by atomic hydrogen; this surface is further denoted C(111)-(1x1):H.<sup>3</sup> Above 800-1000°C annealing temperature in ultra-high vacuum (UHV) a (2x1)-reconstruction evolves after hydrogen desorption as shown by the LEED pattern in Fig. 2.8e. This reconstruction consists of three domains that are rotated by 120°. The accepted model for the clean (111) surface consists of  $\pi$ -bonded zig-zag chains as originally proposed by Pandey for the Si(111) surface [61]. The atomic configuration of the further denoted C(111)-(2x1) surface is sketched in Fig. 2.8c) and d).

### 2.5.2 C(100)

The bulk terminated (100) surface has two dangling bonds per surface carbon atom and is thus unstable. The clean surface lowers its surface energy by the formation of  $\pi$ -bonded dimers between nearest neighbors [62] and the surface exhibits two (2x1)-reconstructed domains that are rotated by 90° as shown in Fig. 2.9c) and d). Exposing the surface to atomic hydrogen does not remove the reconstruction in contrast to the hydrogenated (111) surface [63], and the hydrogen terminated C(100) surface remains 2x1 reconstructed as shown in Fig. 2.9a) and b). This so-called C(100)-(2x1):H surface is further discussed in the context of the electron affinity of diamond (see Chapter 4).

---

<sup>3</sup>It is still under debate whether higher hydrogen coverages exist [60].

### 2.5.3 C(110)

The C(110) surface is the only low-index diamond surface that does not reconstruct, whether in the hydrogenated (Fig. 2.10a) and b) ) or in the clean (Fig. 2.10c) and d) ) case. Moreover, the size of the surface unit cell remains unchanged independent of hydrogen coverage [56, 64]. The surface carbon atoms (shaded circles in Fig. 2.10a)-d) ) that form zig-zag chains running along  $[1\bar{1}0]$  are the characteristic element of the (110) surface. A typical LEED diffraction pattern of the hydrogenated and the clean (not shown) (110) surface is depicted in Fig. 2.10e).

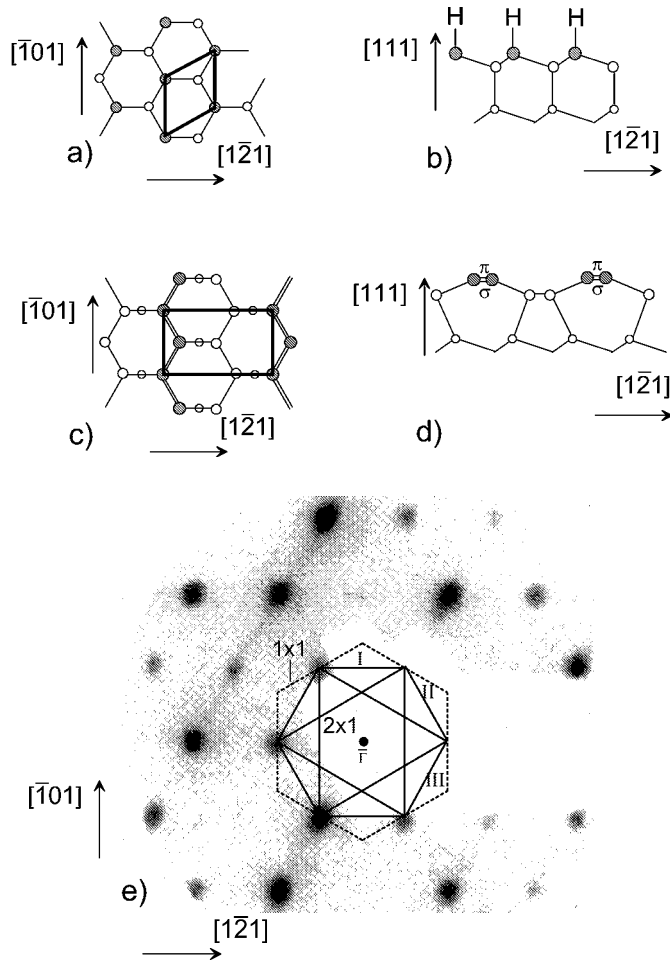


Figure 2.8: Schematic projection view (a) and cross section view (b) of the hydrogen terminated unreconstructed C(111) surface, further denoted as C(111)-(1x1):H. In addition, the surface unit cell is shown in Fig. a). The shaded circles indicate the position of surface carbon atoms (in Fig. a) the hydrogen termination is not drawn). Schematic projection view (c) and cross section view (d) of the clean, 2x1 reconstructed (111) diamond surface. The double bonds in c) and d) account for the  $\sigma$  and  $\pi$  bonding configuration of the surface carbon atoms (shaded circles) that form zig-zag chains. These chains are the characteristic structural elements of the further denoted C(111)-(2x1) surface. e) LEED pattern of the clean 2x1 reconstructed C(111) surface ( $E=153$  eV). The corresponding surface Brillouin zones (BZ) of the three domains (solid lines) are superimposed.

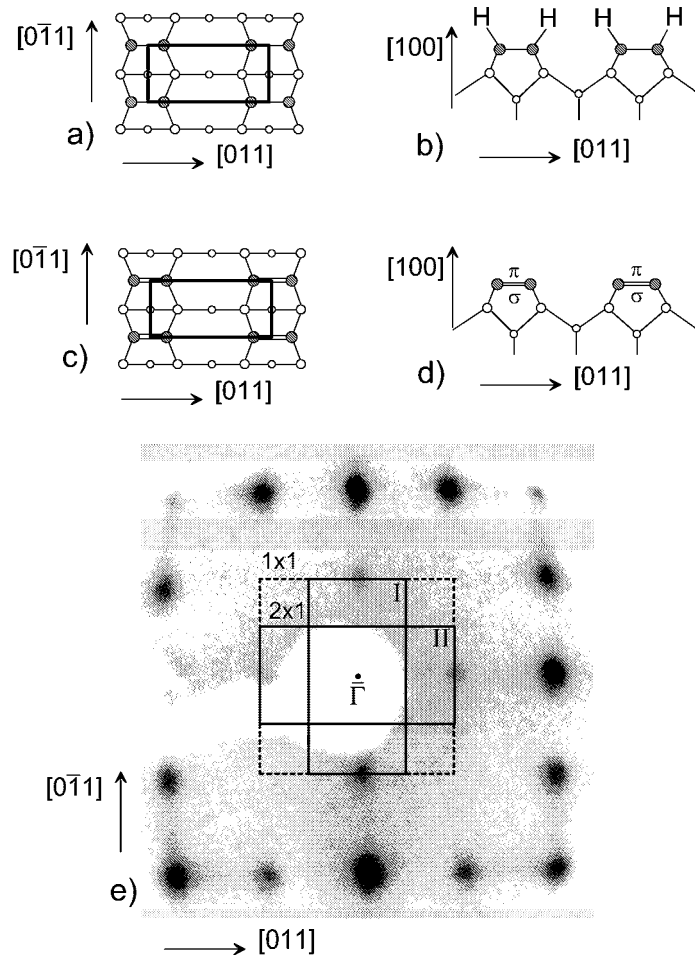


Figure 2.9: Schematic projection view (a) and cross section view (b) of the hydrogen terminated 2x1 reconstructed C(100) surface, further denoted as C(100)-(2x1):H. In addition, the surface unit cell is shown in Fig. a). The shaded circles indicate the position of surface carbon atoms forming dimer rows which are the characteristic structural element of the diamond (100)-(2x1) surface (in Fig. a) the hydrogen termination is not drawn). Schematic projection view (c) and cross section view (d) of the clean, 2x1 reconstructed (100) diamond surface. The double bonds in c) and d) account for the  $\sigma$  and  $\pi$  bonded dimers of the surface carbon atoms (shaded circles). e) Typical LEED pattern of the hydrogenated and the clean (not shown) 2x1 reconstructed C(100) surface ( $E=94$  eV). The corresponding surface Brillouin zone (solid lines) of the two domains are superimposed together with the unreconstructed (dashed lines) surface unit cell.



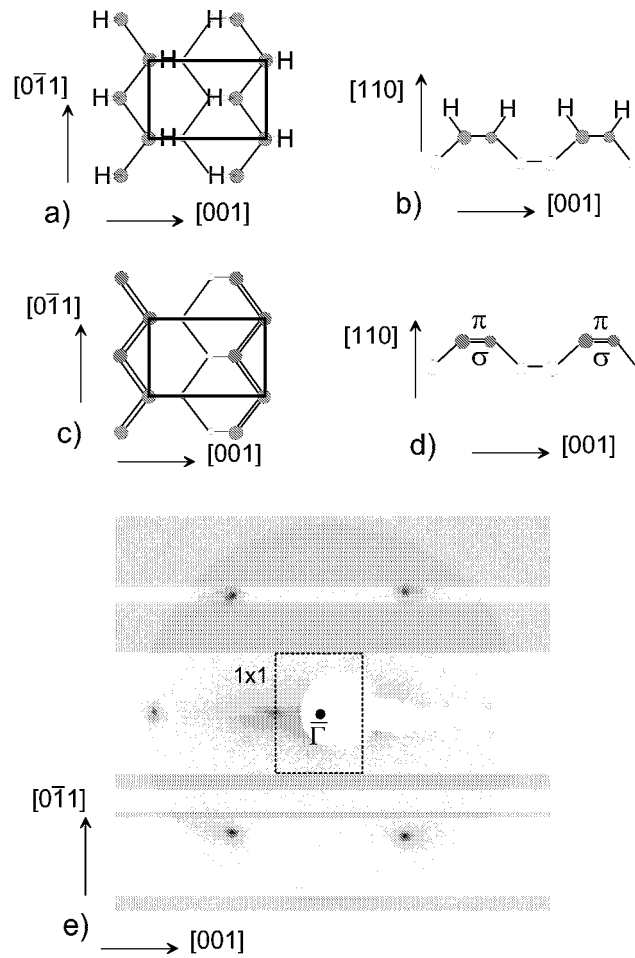


Figure 2.10: Schematic projection view (a) and cross section view (b) of the hydrogen terminated unreconstructed C(110) surface. In addition, the surface unit cell is shown in Fig. a). The shaded circles indicate the position of surface carbon atoms passivated with hydrogen. Schematic projection view (c) and cross section view (d) of the clean, unreconstructed (100) diamond surface. The double bonds in c) and d) account for the  $\sigma$  and  $\pi$  bonded zig-zag chains of the surface carbon atoms (shaded circles). e) Typical LEED pattern of the hydrogenated and the clean (not shown) C(110) surface ( $E=115$  eV). The corresponding surface Brillouin zone (solid lines) is superimposed.



# Chapter 3

## The diamond (110) surface

### 3.1 General considerations

In contrast to extensive experimental [27, 65, 66] and theoretical [63, 67] studies of diamond (100) and (111) surfaces there are only few investigations dealing with the C(110) surface. There is evidence that the (110) surface is quite unstable under CVD growth and etching processes [68–71]. In particular, it is demonstrated in Monte Carlo simulations performed by Battaile *et al.* that the (110) surface has a strong tendency to roughen due to the formation of (111) facets [72]. Nevertheless, this surface orientation may influence diamond growth. In theoretical studies dealing with growth processes on diamond (111) and (100) the role of (110)-like bonding configurations at steps has been emphasized for layer-by-layer growth modes [73, 74]. This is shown in Fig. 3.1b for the case of steps along  $[\bar{1}10]$  of a (111) surface. The bonding configuration of the atoms that are emphasized in Fig. 3.1b in the vicinity of a bilayer step corresponds to that of the (110) surface [72] which is shown in Fig. 3.1a.

Especially, it was shown that diffusion of atomic hydrogen during CVD growth is fast enough along the troughs between the  $[\bar{1}10]$  ridges to occur within typical lifetimes of the gasphase radicals [75]. In contrast to diamond CVD growth, (110) facets are often formed during high pressure high temperature (HPHT) diamond synthesis [76]. These growth sectors contain the minimum amount of nitrogen impurities [77] compared to other crystallographic orientations and therefore, the number of compensating donor impurities in p-type devices is drastically reduced for (110) facets. This was confirmed by measurements in our laboratory that the high p-type surface conductivity that is reported in Chapter 6 is only present on (110) sectors of (100) HPHT substrates [78].

Lurie and Wilson [74] examined the C(110) surface with low-energy electron diffraction (LEED) and observed a rectangular (1x1) diffraction pattern.

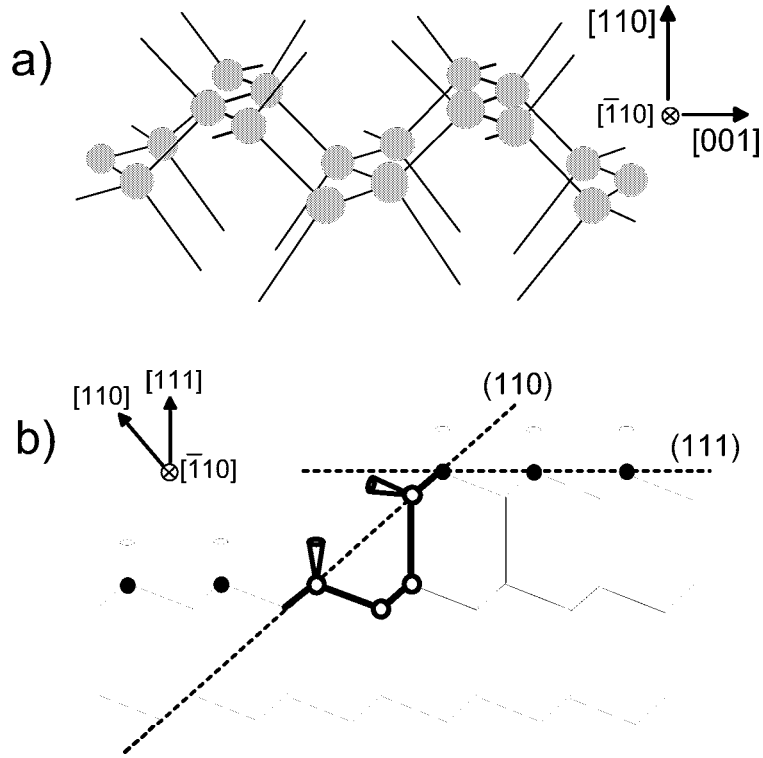


Figure 3.1: a) Sketch of the first two atomic layers of the bulk truncated (110) surface: It is characterized by zigzag chains running along  $[\bar{1}10]$ . The surface carbon ridges that are separated by monoatomic troughs demonstrates the high anisotropy of this type of surface. b) Steps along  $[\bar{1}10]$  of a (111) surface exhibit the bonding configuration of the (110) surface.

In contrast to diamond (111) and (100) no reconstruction has been reported based on LEED observations. The first theoretical investigation of the diamond (110) surface has been published by Davidson and Pickett [79]. Applying semiempirical tight-binding methods they predicted slightly dimerized zig-zag chains in the first atomic layer for the bare as well as the hydrogenated C(110) surface. In the framework of first principles molecular dynamics calculations Alfonso, Drabold and Ulloa [80] arrived at a bulk-like hydrogen-terminated (110) surface, i.e. one without dimerization of the zig-zag chains. For the clean C(110) surface they found a non-dimerized chain structure exhibiting a strong buckling with an amplitude of  $0.14\text{\AA}$  in the top layer. Finally, the clean and the hydrogen-covered C(110) surfaces were also investigated by Kern and Hafner [64] with self-consistent *ab initio* density-functional techniques. They, however, proposed for the bare C(110) surface an unbuckled top layer, again without dimerization, and a rigid inward relaxation of the first atomic layer by  $0.17\text{\AA}$ . The addition of hydrogen recovers essentially the bulk terminated struc-

ture. Concerning the electronic properties of the surface, electron energy loss spectra (EELS) by Pepper [81] were interpreted in terms of unoccupied surface states within the band gap which appear after annealing the diamond (110) sample above 900°C. At this temperature the hydrogen is expected to desorb. Angle-integrated ultraviolet photoelectron spectroscopy data by Francz *et al.* [82] showed an increase of the valence band density of states at 3.5 eV and 13.6 eV below the valence band maximum (VBM) on (110) natural diamond after annealing above 870°C. These additional intensity maxima disappeared after exposing the surface to hydrogen or deuterium.

## 3.2 Experimental aspects

The as-received crystal (type IIb) had a mechanically polished (110) surface of about 3x6 mm<sup>2</sup> area. Atomic force microscopy revealed that the (110) surface had macroscopic polishing grooves along [001] which is known to be the soft polishing direction [83]. The surface was highly contaminated by oxygen containing species as seen by XPS. The electronic valence band structure probed by ARUPS showed virtually no features dispersing with electron emission angle and we therefore considered this surface insufficiently ordered. As described in the previous chapter plasma hydrogenation was performed. To minimize etching damage the plasma exposure of the (110) surface was kept to 3-5 minutes which was considerably shorter than for the preparation of diamond (100) and (111) samples [54, 55]. The temperatures quoted were measured using an infrared pyrometer that probed the tantalum support underneath the sample. The XPS-measurements were performed with an energy resolution of 0.6 eV using monochromatized Al  $K\alpha$  x-rays. ARUPS was carried out at the storage ring of BESSY I in Berlin with photon energies between 30 eV and 120 eV using the Toroidal Energy Analyzer of Leckey and Riley [84]. This analyzer recorded spectra for polar emission angles throughout  $\pm 90^\circ$  relative to normal emission simultaneously with angular and energy resolution of  $\pm 2^\circ$  and  $\pm 0.15$  eV, respectively.

## 3.3 Results and discussion

### 3.3.1 LEED investigations

After cleaning with acetone and methanol the “as-polished” (110) surface exhibited weak (1x1)-LEED spots with a high background of diffuse scattering intensity. Some decrease in background was achieved by annealing the sample at about 800°C for 20 minutes. After the first hydrogen plasma treatment the LEED pattern was changed drastically towards bright (1x1)-spots with very low diffuse background. In [001] direction the width of the diffraction spots varied periodically with energy while it remained constant in the  $[1\bar{1}0]$  direction. This behaviour is demonstrated by a series of LEED patterns in Fig. 3.2 a) - d) which also shows a sketch of the bulk truncated first and second atomic layers of the (110) surface (Fig. 3.2 e) and the corresponding first surface Brillouin zone (Fig. 3.2 f). These LEED characteristics remained stable during subsequent annealing steps up to 1000°C; in particular, no reconstruction was observed. Only after annealing beyond 1000°C an intense diffuse background reappeared, most likely indicating a graphitization of the surface, which was also observed in the case of diamond (111) and (100) [54, 85]. The absence of any fractional order spots confirms the previous results of Lurie and Wilson [74] that no reconstruction of the (110) diamond surface can be induced by thermal annealing. However, in contrast to the work of Cheng *et al.* [69] and Mercer *et al.* [70] no spots corresponding to (111) facets were observed in this study. With increasing electron energy all diffraction maxima converged towards the (0,0) spot. Also, rotation of the sample relative to the LEED system to cover the whole hemisphere showed no diffraction maxima other than those of an unreconstructed (110) surface of an fcc crystal.

However, there were systematic extinctions of certain spots for normal incidence of the electron beam. In particular, spots of the type  $(0, 2n+1)$  ( $n$  integer) along  $[1\bar{1}0]$  were missing for all primary electron energies. This proves the persistence of the glide mirror symmetry of the (110) lattice planes of diamond shown in Fig. 3.2e. The extinction relies on the fact that the glide mirror operation involves a translation by half a unit vector along  $[1\bar{1}0]$  that superimposes the lower part of the surface unit cell in Fig. 3.2e onto the upper one. This symmetry is maintained as long as the surface carbon chains are not dimerized along  $[1\bar{1}0]$ . A particularly convincing example of the symmetry related extinction of beams is shown in Fig. 3.3 for the as-prepared C(110) surface. At a primary electron energy of 144 eV a pronounced streaking in the vicinity of the (0,1) spot occurred. However, right at the (0,1) position (arrow in Fig. 3.3) the intensity dropped to zero as required by symmetry. This is compelling experimental evidence for the absence of chain dimerization. For the dehydrogenated surface, reflexes of the type  $(0, 2n+1)$  were not detectable either.

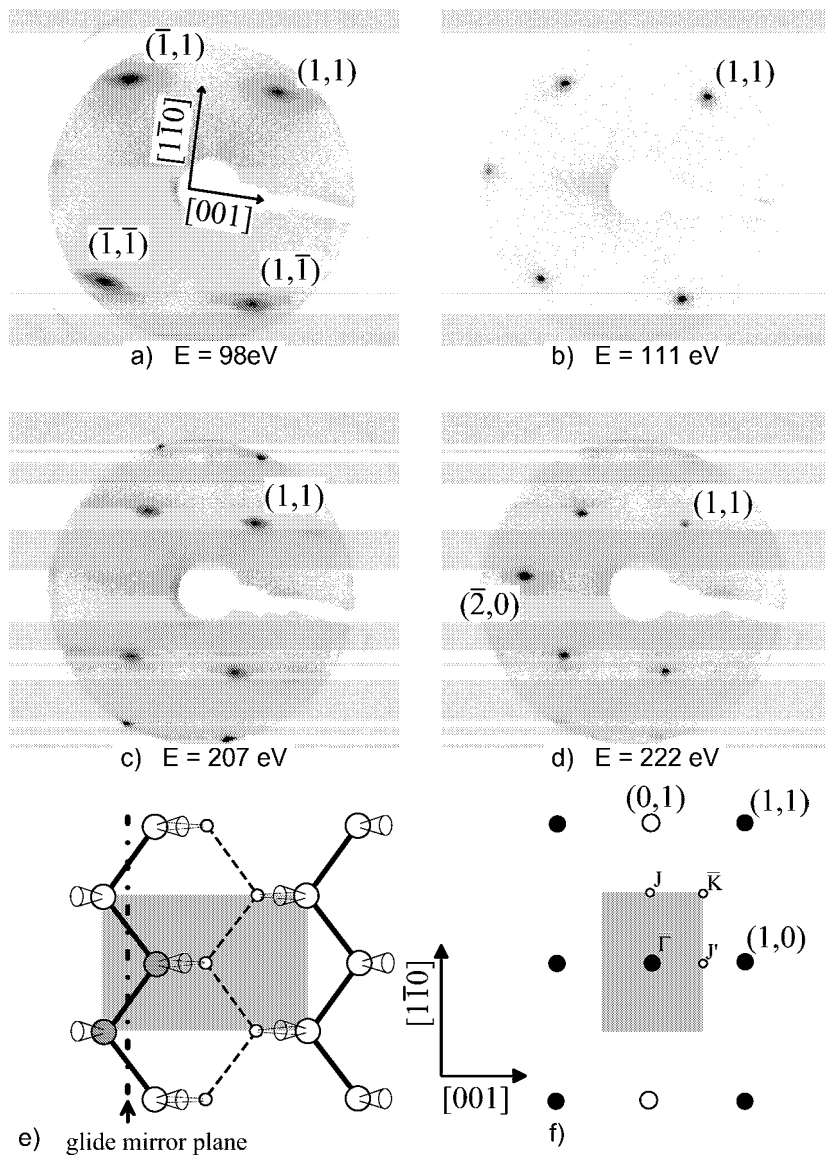


Figure 3.2: a) - d): Series of LEED patterns of the plasma hydrogenated diamond (110) surface obtained for selected primary electron energies. e), f): Schematic of the bulk truncated (110) surface in real space of the first (large circles) and the second atomic (small circles) layer and in reciprocal space. The shaded areas are the corresponding unit cells. The open circles in f) indicate reciprocal lattice points for which LEED reflexes are forbidden by the glide mirror symmetry of the lattice.

Therefore, the persistence of symmetric chains after dehydrogenation was also indicated by LEED. Since non-spherical contributions of valence electrons

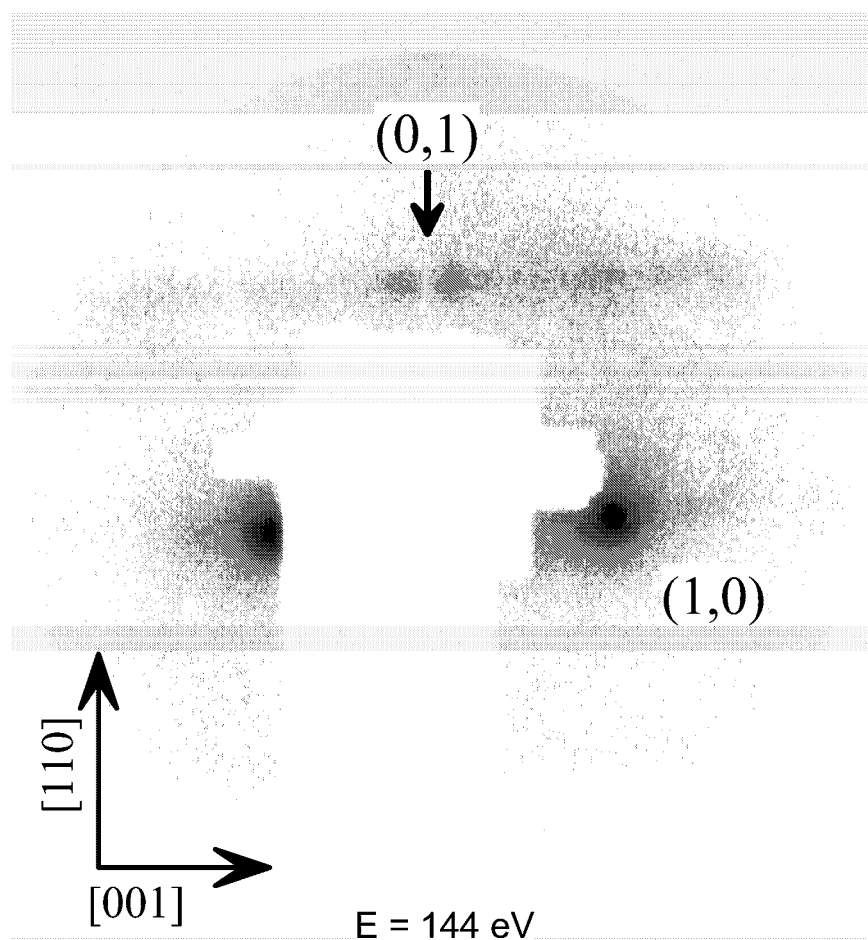


Figure 3.3: LEED pattern of the hydrogenated (110) surface; the arrow points towards the symmetry related extinction position of the (0,1) reflex.

can usually be neglected in LEED (muffin-tin approximation) [86], a more general extinction rule holds for spots of the kind  $(i,j)$  with  $i/2+j=2n+1$  ( $i, j, n$  integer) in the absence of any lateral relaxation of atoms within the (110) surface unit cell of diamond. In particular, this rule would apply to the  $(\bar{2},0)$  reflex which was nevertheless seen clearly in the LEED patterns (Fig. 3.2d). This violation of the selection rule requires in-plane relaxation of atomic positions along the [001] direction because that is the only relaxation process which preserves the glide mirror symmetry discussed above. The brightness of the  $(\bar{2}0)$  reflex was comparable to the allowed reflexes and indicated that the lateral relaxation of surface atoms was substantial. It is also rather likely that these surface displacements are transferred via lattice strain to subsurface



layers as well and thereby contribute to the diffraction intensity of an otherwise forbidden reflex. These conclusions are in qualitative agreement with the theoretical work of Kern *et al.* [64] who predict undimerized chains and a reduction of the surface C-C-bond length by 1.4% and 7.2% (compared to the bulk value) for the hydrogenated and the bare diamond (110) surface, respectively.

The absence of spot-splitting and the oscillatory intensity variation of the streaks as a function of electron energy (see LEED series in Fig. 3.2) is well compatible with an irregularly stepped surface [33, 87] with terraces of varying width separated by steps of well defined height  $H$ , running parallel to the  $[1\bar{1}0]$ -direction. Since LEED spot profiles are well described within the kinematic approximation [87], particularly sharp spots are observed when the Laue condition is met for the direction perpendicular to the surface as well as for the two-dimensional surface unit mesh. This yields the condition of constructive interference for the component of the scattering wave vector perpendicular to the surface:  $\Delta k_{\perp} = 2\pi n$  ( $n$  integer). For normal incidence of the primary electron beam, the step height  $H$  is thus readily calculated from the energies  $E_n, E_{n+1}$  at which two consecutive minima in the width of a particular LEED reflex are observed:

$$H = \frac{h}{(1 - \cos\theta_{n+1})\sqrt{m_e E_{n+1}} - (1 - \cos\theta_n)\sqrt{m_e E_n}} \quad (3.1)$$

where  $\theta_n, \theta_{n+1}$  are the corresponding diffraction angles and  $h$  and  $m_e$  are Planck's constant and the electron mass, respectively. For the C(110) surface this type of analysis led to a step height of  $1.3 \pm 0.1 \text{ \AA}$  which corresponds to one monoatomic step ( $1.26 \text{ \AA}$ ).

### 3.3.2 C1s core level spectroscopy

As measured by XPS, the "as-polished" surface showed significant silicon oxide contamination which was stable up to  $1000^{\circ}\text{C}$  annealing temperature but disappeared completely after the first plasma treatment. Fig. 3.4 represents the C1s core level spectra after plasma hydrogenation and three subsequent annealing steps. A consistent fit of the spectra required three components which are labelled  $B, S_A$  and  $S_C$  in Fig. 3.4 following the nomenclature of Graupner *et al.* where very similar spectra were reported for diamond (100) and (111) [54]. The spectrum of the freshly prepared C(110) surface (not shown in Fig. 3.4) was characterized by the bulk C1s line  $B$  and an additional component  $S_A$  which was shifted to higher binding energy by  $\Delta E = +0.78 \pm 0.05 \text{ eV}$ . Varying the detector angle for emitted photoelectrons, and thus the effective mean electron escape depth, the nature of  $S_A$  as emission from surface atoms was established. For annealing temperatures higher than  $600^{\circ}\text{C}$   $S_A$  started to decrease and the total spectrum shifted to higher binding energies. After  $750^{\circ}\text{C}$

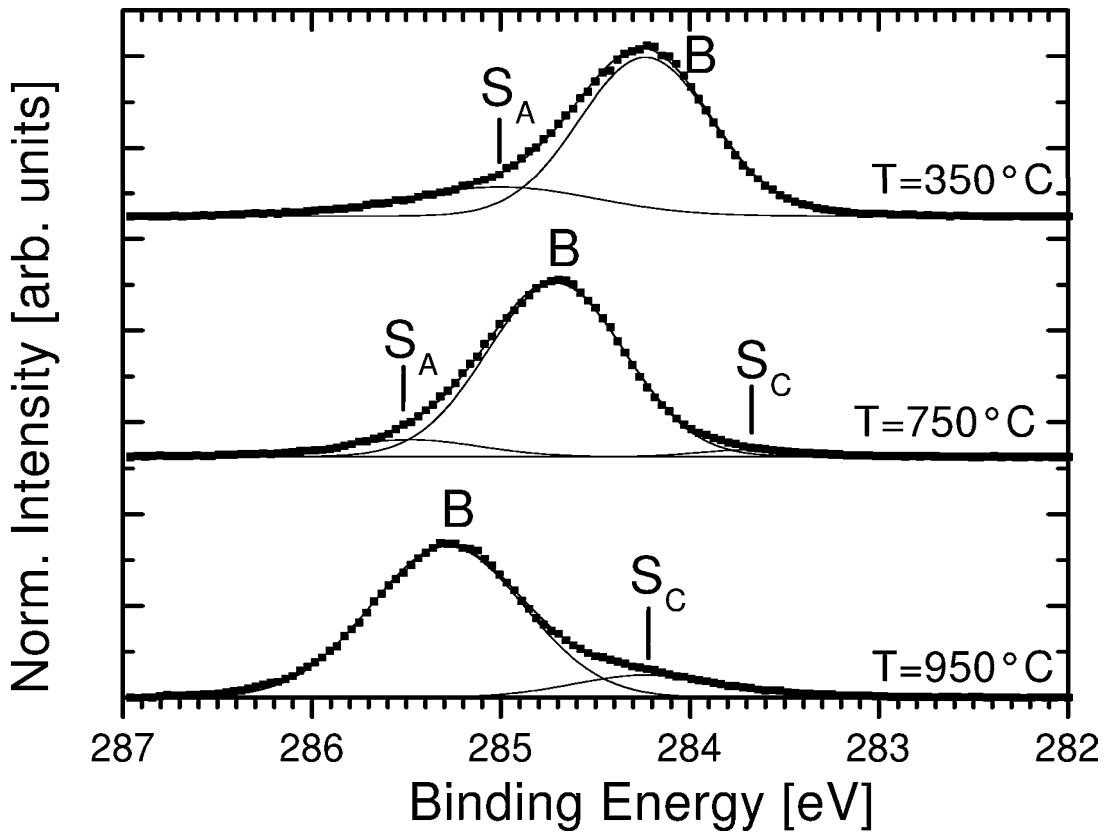


Figure 3.4: C1s core level spectra of the plasma hydrogenated diamond (110) surface after selected annealing steps.

a new component  $S_C$  appeared at the lower binding energy side of  $B$  shifted by  $\Delta E = -1.08 \pm 0.02$  eV while  $S_A$  was still visible (intermediate phase). Finally at temperatures above  $900^\circ\text{C}$   $S_A$  has vanished and the intensity of  $S_C$  has saturated (final phase). It should be mentioned that the C1s spectra of the “as-polished” surface exhibited a similar behaviour in the course of annealing.

Following our extensive XPS measurements of diamond (100) and (111) [54] the current XPS results are interpreted in light of the previous work. After hydrogen plasma treatment both diamond (100) and (111) exhibit a surface core level component  $S_A$  which is shifted to higher binding energies relative to the bulk C1s level by  $+0.50$  eV to  $+0.81$  eV on (100) and  $+0.70$  eV to  $+0.75$  eV on (111) depending on preparation conditions, and most likely originates from hydrocarbons adsorbed at the surface [54]. The detected shift of  $S_A$  of  $+0.78$  eV on C(110) lay in the same range as measured on (100) and (111) surfaces, and also the intensity of  $S_A$  varied dependent on the plasma preparation. After annealing at  $750^\circ\text{C}$  the surface component  $S_C$  appeared at the lower binding energy side of the bulk component  $B$ . Comparing the

first carbon layer of the bulk truncated C(110) surface with the Pandey chains of the (2x1) reconstructed (111) surface [54], a similar atomic arrangement with the possibility of  $\pi$  bonding between the dangling bonds of C(110) leaps to the eye. Therefore, a surface chemical shift of  $S_C$  in the same range is expected which was indeed observed:  $\Delta E = -1.02$  eV for diamond (111) as compared to  $\Delta E = -1.08$  eV for C(110). Note, that for the structurally different C(100)-(2x1) surface (dimer rows) the surface chemical shift amounted to only  $\Delta E = -0.90$  eV. The appearance of  $S_C$  consequently indicated the onset of hydrogen desorption accompanied by the formation of  $\pi$ -bonds. The diamond (110) surface did not show the distinct intermediate phase where only the bulk line  $B$  was seen as it was the case for (100) and (111) surfaces between 300°C and 800°C annealing temperature. For C(100) and C(111) this phase is attributed to surfaces where the dangling bonds are saturated with hydrogen [54]. In contrast, the simultaneous detection of  $S_A$  and  $S_C$  on diamond (110) indicated that regions covered with hydrocarbons and hydrogen and adsorbate free parts coexisted. This points towards a higher degree of disorder of the (110) surface as compared to the other crystal surfaces. In Fig. 3.4 binding energies are referred to the Fermi level  $E_F$ . The rigid shift of the spectra as a function of annealing temperature reflects thus an increase in downward surface band bending of about 1.1 eV. As demonstrated in Chapter 3.1 for the C(111) surface, this change in band bending is initially due to the desorption of adsorbates, and at higher temperatures also indicates an incipient graphitization as has been discussed elsewhere [85]. Further discussion of the phenomenon of band bending and Fermi level pinning is provided in Chapter 4.

### 3.3.3 Surface states

From the discussion of structural and chemical aspects of the C(110) surface we now turn to its electronic properties as probed by ARUPS. Figs. 3.5a and Fig. 3.5b show energy distribution curves (EDC's) taken along the  $\bar{\Gamma} - \bar{J}$  azimuth ( $[1\bar{1}0]$ -direction) at an excitation photon energy of 50 eV which turned out to yield least interference of bulk and surface states in the vicinity of the VBM. The change in energy due to band bending effects (see previous section) were corrected for the spectra of the dehydrogenated surface. The EDC's of the hydrogen plasma treated C(110) crystal after annealing at 800°C are depicted in Fig. 3.5a) over a wide energy range. This is the highest annealing temperature for which the absence of surface states ensures an essentially hydrogen terminated surface without further contamination [55]. The indicated VBM position of  $1.0 \pm 0.1$  eV below the Fermi level  $E_F$  was determined in a constant initial state (CIS) experiment similar to that described in Section 2.1.1.

In the case of the hydrogenated surface the spectral features (Fig. 3.5a) were well defined and strongly dispersive. All of them were located within the projected bulk band structure [64]; moreover, most of them showed dispersion

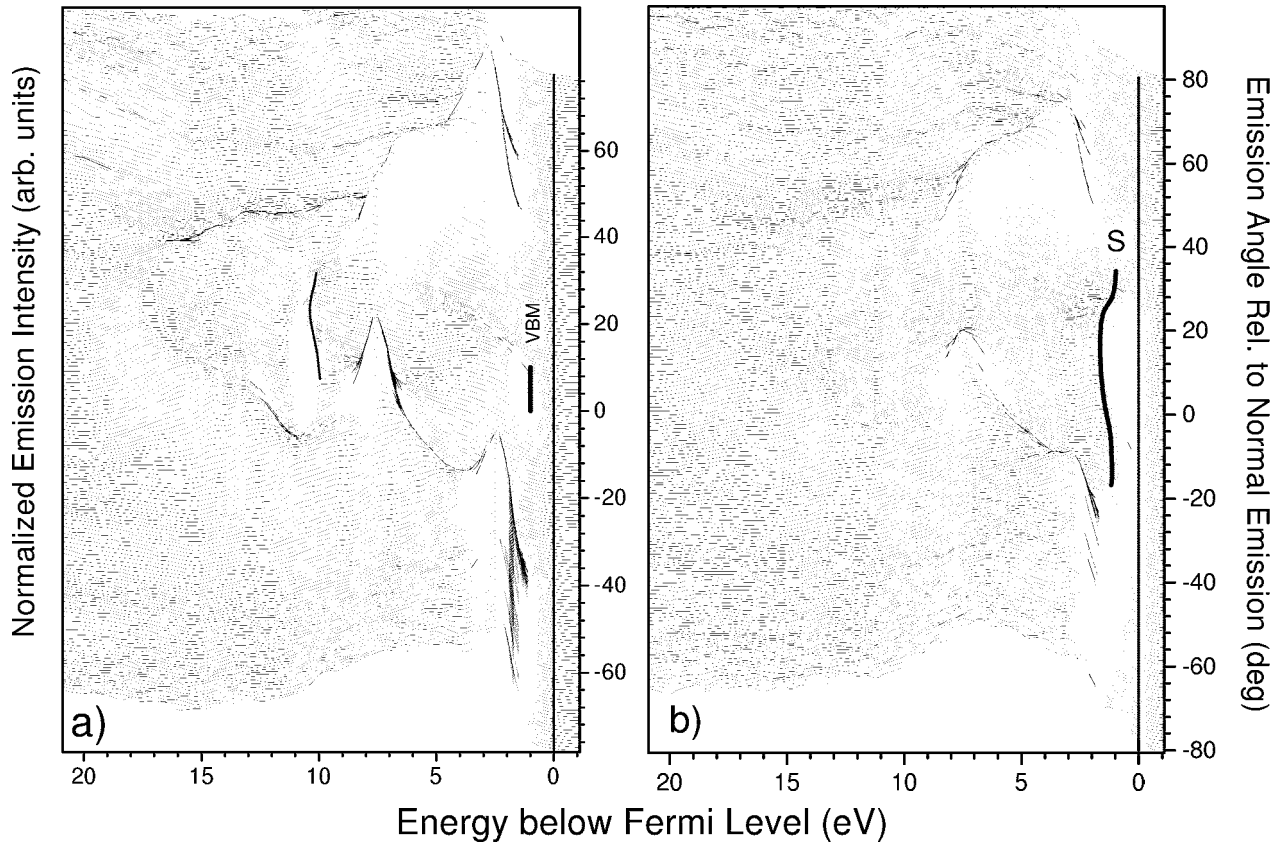


Figure 3.5: Angle resolved valence band spectra of the plasma hydrogenated diamond (110) surface after annealing at 800°C (a) and at 930°C (b):  $h\nu = 50$  eV; azimuth:  $\bar{\Gamma} - \bar{J}$  (the lines are guides to the eye).

with photon energy. Therefore, these states are attributed to bulk interband transitions. After dehydrogenation these features broadened which is in keeping with the decrease in surface ordering mentioned above. Only the marked state in Fig. 3.5a at about 10.5 eV binding energy seemed to disappear or broaden much more than the rest of the spectra. Additionally, this state did not disperse with photon energy. It is tempting to speculate that it indicates a hydrogen induced surface resonance. Theoretical studies do not predict any surface related features in this energy regime, however. Furthermore, a new state labelled S in Fig. 3.5b appeared 1.4 eV below  $E_F$ . S fulfills the requirements for a surface state, i.e. it shows no dispersion with photon energy, it is partially located in the energy gap of the projected bulk band structure, and it is quenched by adsorbates. The dispersion relation of state S along the  $\bar{\Gamma} - \bar{J}$  azimuth as shown in Fig. 3.6 was deduced, both from spectra at 45 eV and 50 eV.

In contrast to the  $\bar{\Gamma} - \bar{J}$  azimuth, the ARUPS measurements in the perpendicular direction  $\bar{\Gamma} - \bar{J}'$  (along [001]) showed very little dispersing features. For

the clean surface a shoulder at the high energy side of the spectra extended up to the VBM for all emission angles that would be in keeping with a non-dispersing surface state  $S'$ . All this pointed towards a substantial loss in  $k_{\parallel}$  conservation as a result of reduced long range order in this direction after annealing. Therefore, the non-dispersing state  $S'$  in Fig. 3.5 reflected not a surface state but mainly the density of states in this energy region. In comparison with the results of Francz *et al.* [82] the additional emission intensity 3 eV below  $E_F$  for the hydrogen free surface has not been confirmed here.

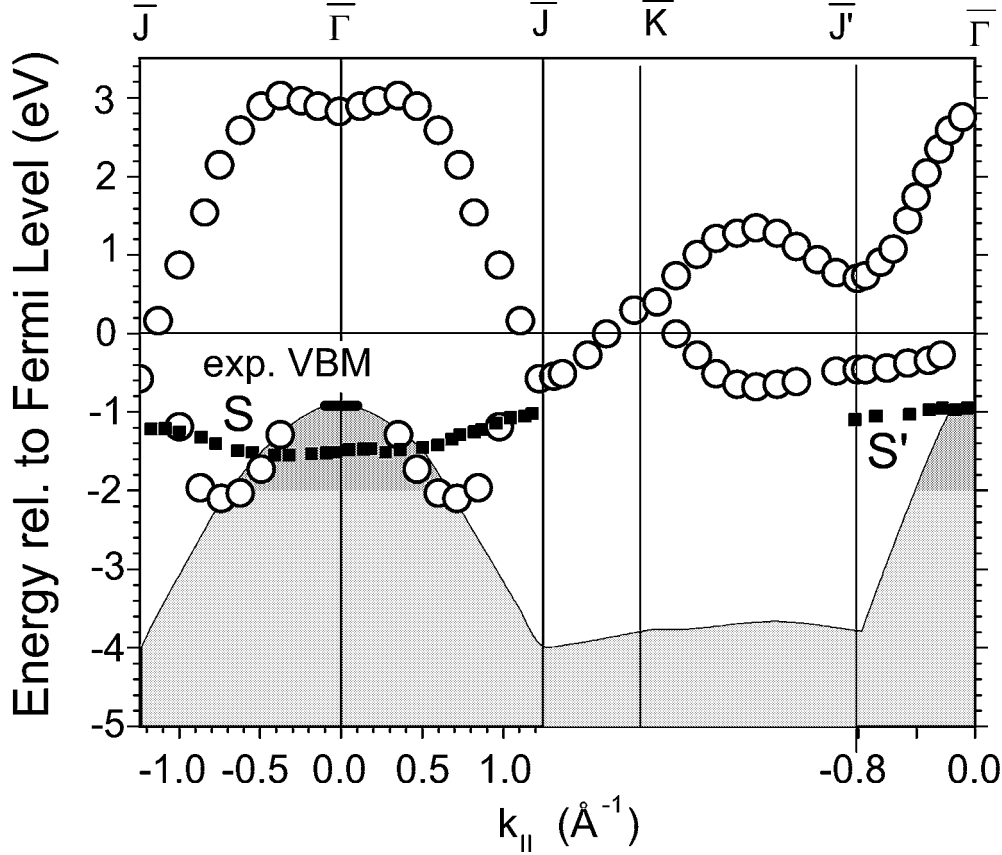


Figure 3.6: Band structure of the bare C(110) surface. The filled squares mark the experimentally determined dispersion of surface state  $S$  and  $S'$  along the  $\bar{\Gamma}-\bar{J}$  and the  $\bar{\Gamma}-\bar{J}'$  azimuthal direction, respectively. The open circles are taken from Ref. [64] and the shaded area indicates the projected bulk band structure.

Concerning the electronic surface structure of diamond (110) theoretical studies came to different conclusions for the clean surface. Davidson and Pickett [79] predicted a semiconducting surface with a small gap at  $\bar{J}$ . In contrast, two *ab initio* calculations obtained a metallic bandstructure. The surface states crossed the Fermi level near  $\bar{\Gamma}$  and near  $\bar{J}$  in the work of Alfonso *et al.* [80] and at the border of the Brillouin zone near  $\bar{K}$  and  $\bar{J}$  according to Kern *et al.* [64].

The measured dispersion relation for S in Fig. 3.6 was compared with the most recent theoretical results of Kern and Hafner [64]. Experiment and calculation were aligned at the VBM yielding the same position for  $E_F$  in theory and experiment. The latter observation might be fortuitous. In the direction of interest ( $\bar{\Gamma} - \bar{J}$ ) the calculations predict two surface states, a bonding and an antibonding one, that are degenerate at  $\bar{J}$ . The antibonding state crosses the Fermi level at about 90 % along the way from  $\bar{\Gamma}$  to  $\bar{J}$ . In our experiment the surface band state S presumably corresponded to the bonding state. S reached the Brillouin zone boundary at  $\bar{J}$ , 1.1 eV below  $E_F$  which is 0.3 eV lower than predicted by Kern and Hafner [64]. In addition, the band width of state S was significantly smaller than expected by all theoretical studies (0.35 eV vs 1-2 eV). Furthermore, the occupied portion of the antibonding state near  $\bar{J}$  was not observed in our experiment. For the sake of completeness, the position of the non-dispersing state S' that was ascribed to density of states of the disordered surface is also added in the band diagram.

Finally, a closer look at the angle integrated spectra along the azimuth directions  $\bar{\Gamma} - \bar{J}$  and  $\bar{\Gamma} - \bar{J}'$  (not shown here) did not reveal a Fermi edge characteristic for a metallic surface. However, there was very low intensity observed at  $E_F$ , which has also been detected at the annealed diamond (111) surface [55]. In our opinion, this additional intensity is due to emission from parts of the surface where graphitization occurs during the annealing process. Thus, the metallic character of the surface in the form predicted by Kern *et al.* [64] cannot be confirmed the ARUPS measurements. A closing of the gap in a different direction can, however, not be excluded.

## 3.4 Summary

Extending previous investigations on C(100) and C(111) [54, 55] to diamond (100), it turned out that this particular surface is of inferior quality to the (111) and the (100) surface. Mechanically polished samples always exhibit macroscopic grooves along [001] which are due to the high anisotropy of hardness that is typical for this surface orientation [83]. After hydrogen plasma polishing, the low-energy electron diffraction (LEED) pattern exhibits pronounced streaking in this direction, i.e. the direction perpendicular to the atomic zig-zag chains which are the characteristic structural element of the C(110) surface. Also, angle-resolved valence band spectroscopy (ARUPS) data show no dispersion of valence band states along [001], pointing towards a substantial loss in translation symmetry along this direction. Furthermore, the investigation of the local surface configuration by means of core-level photoemission spectroscopy (XPS) does not permit to distinguish clearly between a surface superficially covered by adsorbed hydrocarbons and a surface only terminated by hydrogen after annealing in UHV, as is the case for C(111) and C(100).

Despite these limitations a number of structural and electronic information has been deduced from LEED and ARUPS data.

(i) The (110) surface is not reconstructed, neither in its hydrogenated nor in its hydrogen free form.

(ii) The hydrogenated and the bare (110) surface exhibit zig-zag chains of C-atoms running along the  $[1\bar{1}0]$  that are clearly not dimerized as proven by symmetry related extinctions of definite LEED reflexes. There is, however, compelling evidence that the C-C bond length in the surface chains is substantially different from its bulk value. This is consistent with *ab initio* calculations which predict a reduced in-plane bond length.

(iii) The streaking of LEED spots in [001] direction is due to a high density of monoatomic steps running along  $[1\bar{1}0]$ .

(iv) By means of ARUPS, a weakly dispersing surface state S has been unambiguously detected between  $\bar{\Gamma}$  and  $\bar{J}$  in the surface Brillouin zone of the dehydrogenated (110) surface, i.e. the direction along the chains. Comparing the dispersion relation of S with *ab initio* calculations [64], the band width of S is considerably smaller than expected from theory. This surface state remains entirely below the valence band maximum (VBM).

(v) As in the case of diamond (111) the metallic nature of the (110) surface, as predicted by theory, is not confirmed experimentally.

(vi) In the perpendicular direction, however, an appreciable increase in density of occupied states has been detected by ARUPS after dehydrogenation. This is consistent with the high step density observed by LEED reflecting the disordered state of the surface. From that point of view, the fairly large band bending observed in XPS and UPS of more than 1 eV during hydrogen desorption may be ascribed to the high number of defect states.





# Chapter 4

## Electron Affinities of Hydrogenated and Oxidized C(100) Surfaces

### 4.1 Introduction

Two features of diamond surfaces are unique among all semiconductors [88]. One is the true negative electron affinity (NEA) of the hydrogenated surface making diamond a candidate in the field of cold cathode field emission [89]. Second, diamond shows under special circumstances a fairly high p-type surface conductivity which has already proven its potential for electronic devices [22, 90]. As will be shown in Chapter 6, this latter property is closely related to the first one [21]. Within the framework of an electrochemical model a negative electron affinity of diamond of about -1.3 eV is a prerequisite for the observed surface conductivity. Therefore, quantitative information about the electron affinity of clean and adsorbate covered diamond surfaces is essential.

The electron affinity  $\chi$  is the energy difference between the conduction band minimum  $E_{CBM}$  and the vacuum level  $E_{vac}$

$$\chi = E_{vac} - E_{CBM}. \quad (4.1)$$

$\chi$  can be modified by adsorbed surface atoms via the formation of a surface dipole layer (see Chapter 2.2). This situation is illustrated on top of Fig. 4.1 for the three surfaces of interest here. As hydrogen exhibits a lower electronegativity than carbon the C-H-bond is polarized with a positive charge  $\delta^+$  on the H-atom. The ensuing double layer provides a potential step that pulls the vacuum level below the CBM over a distance that corresponds to the C-H bond

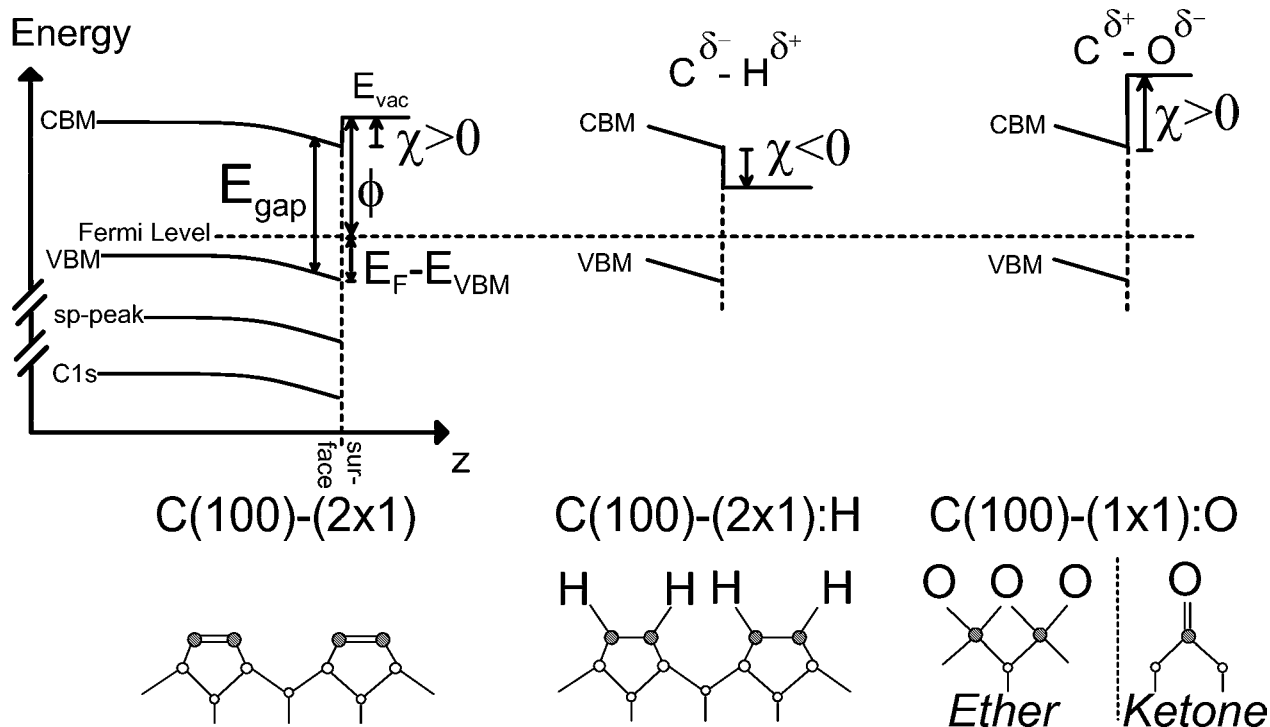


Figure 4.1: Top: Band scheme and electron affinity  $\chi$  for a bare, hydrogenated, and oxidized diamond (100) surface (for details, see text). Bottom: Sketch of the atomic arrangement of the bare, the hydrogenated and the oxidized diamond (100) surface.

length. By the same mechanism, adsorbates with a higher electronegativity than carbon raise  $\chi$  compared to the clean surface as is the case for oxygen.

The three surface configurations we are dealing with here are sketched at the bottom of Fig. 4.1. The accepted model for the clean  $C(100)$  surface is a  $(2 \times 1)$  reconstruction in the form of  $\pi$ -bonded dimers [55, 91]. Upon hydrogenation the dimer  $C-C$  double bond is converted to a single bond with one  $H$ -atom attached to each carbon [63] (see also Chapter 2.5.2). However, it is still under debate whether the  $(1 \times 1)$  oxidized surface is the result of an ether-like (oxygen in bridge position) or a ketone-like (oxygen on top) geometry [91].

Since the first report of NEA measurements on diamond by Himpsel and coworkers [92], a considerable number of publications have dealt with the electron affinity of bare and adsorbate-covered diamond surfaces. Salient experimental and theoretical results for the  $(111)$  and  $(100)$  surfaces of diamond are summarized in Table 4.1 at the end of this chapter. In all cases,  $\chi$  has been lowered by hydrogen and raised by oxygen relative to the bare surface. Nevertheless, absolute experimental values of  $\chi$  for the hydrogenated  $C(100)$  NEA surface has been still missing. For  $C(111)$  single crystal diamond surfaces a

detailed *in situ* study was performed by Cui *et al.* measuring simultaneously changes in work function and in band bending [93]. Here, these investigations were extended in a similar manner for the technologically more important (100) surface after hydrogenation and oxidation. Hydrogen and oxygen are the principal adsorbates to be considered for diamond films synthesized by chemical vapor deposition (CVD) [94] and in electronic applications [11]. The electron affinity  $\chi$  is derived from the work function  $\phi$  and  $E_F - E_{VBM}$  (see Fig. 4.1) according to

$$\chi = \phi + (E_F - E_{VBM}) - E_{gap}, \quad (4.2)$$

where  $E_{gap}$  is the band gap of diamond (5.47 eV). It will be shown that the electron affinity of diamond varies from -1.3 eV for the fully hydrogenated C(100)-(2x1):H up to +1.7 eV for the oxidized C(100)-(1x1):O surface. This covers a range of about 3 eV for the same semiconductor. I am not aware of a comparable variability of electron affinities in any other semiconductor system.

## 4.2 Experimental

The sample used in this study was a type IIb natural single crystal diamond with polished (100) faces of 3x5 mm<sup>2</sup> size. The boron concentration of about 10<sup>16</sup>cm<sup>-3</sup> provided a bulk conductivity that was high enough to avoid charging problems during the photoemission and work function measurements. In order to obtain oxygen termination the sample was boiled for one hour in a solution of *conc.* HNO<sub>3</sub>/H<sub>2</sub>SO<sub>4</sub> (1:3) at 350°C [95, 96] after a preceding annealing step in UHV at 1100°C that served to remove residual chemisorbed hydrogen. For hydrogenation the acid treated surface was exposed to a hydrogen plasma (see Chapter 2.4). Clamped to a tantalum foil the sample was heated from the back by electron bombardment in ultra-high vacuum (UHV). At each thermal annealing step the temperature was controlled using an IR-pyrometer that measures the temperature of the sample holder underneath the diamond. These are the temperatures given in the following. Comparing our values with typical desorption temperatures for hydrogen (800 – 1000°C [97]) the absolute surface temperature was estimated to be about 100 – 200°C lower than given by the IR-pyrometer while the relative temperatures were measured with an accuracy of ±5°C. The interpretation of the results, however, did not depend on the absolute temperatures.

At a base pressure of 10<sup>-10</sup> mbar core-level spectroscopy (XPS) and valence-band spectroscopy (UPS) measurements were performed (combined energy resolution:  $\Delta E_{XPS} \approx \pm 0.3$  eV,  $\Delta E_{UPS} \approx \pm 0.04$  eV). All energies were measured relative to the common Fermi level  $E_F$  that was determined from a reference gold foil.

According to Eq. 4.2, the energy position  $E_{VBM}$  of the VBM at the surface relative to the Fermi level  $E_F$  is required for the determination of  $\chi$ . This

has been done in the CIS calibration experiment that has been described in Chapter 2.1.1. Once determined  $E_F - E_{VBM}$ , the change in band bending was traced by the C1s core level (XPS) and by the sp-peak in UPS ( $h\nu = 40.8$  eV). Its energy separation to the VBM equals 283.9 eV and 12.80 eV, respectively, with an uncertainty of  $\pm 0.1$  eV.

Changes in work function were recorded as changes in the contact potential difference (CPD) between the diamond surface and a reference gold foil with an accuracy of  $\pm 5$  mV using the Kelvin method as described in detail in Chapter 2.2. The overall uncertainty in  $\phi$  was thus  $\pm 0.02$  eV. Finally, changes in surface reconstruction were checked by low-energy electron diffraction (LEED).

### 4.3 Electron affinity of the plasma hydrogenated (100) surface

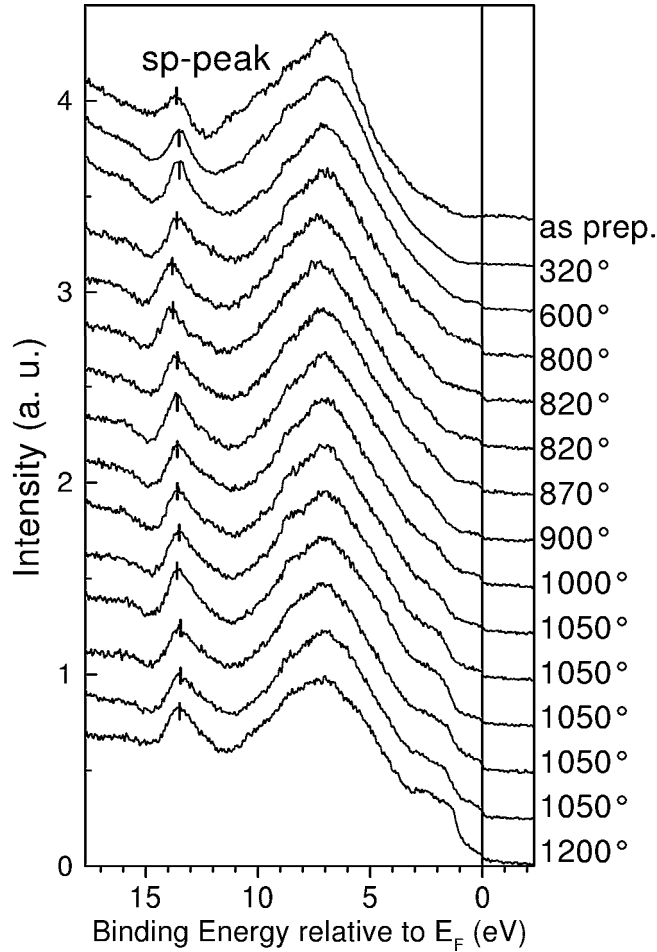


Figure 4.2: Valence band spectra of the plasma hydrogenated (100) surfaces during thermal annealing in UHV ( $\hbar\omega = 40.8$  eV, electron emission angle  $\vartheta = 55^\circ$ )

After acid treatment and hydrogen plasma exposure surface contaminants were below the detection limit of XPS ( $\leq 0.1$  monolayers). Furthermore, the LEED pattern revealed a (2x1) reconstruction with virtually no diffuse background intensity which is typical for a well-ordered, plasma hydrogenated (100) diamond surface. Fig. 4.2 depicts selected valence band spectra during an annealing sequence from nominally 320°C up to 1200°C. From the average binding energy of the sp-peak of 13.57 eV relative to  $E_F$  a position of the VBM of 0.77 eV below  $E_F$  was derived. With a bulk Fermi level at  $0.4 \pm 0.1$  eV above VBM for a boron doped diamond this corresponded to a downward band bending of 0.4 eV which was considerably larger than measured for the (100) sample

used in the CIS calibration experiment described in Chapter 2.1.1 (0.1 eV). At temperatures above 1000°C a shoulder at 2 eV binding energy appeared that is attributed to the formation of a surface state [55, 98] which is characteristic for the clean surface. The small Fermi edge in the spectra of Fig. 4.2 had nothing to do with the sample itself. It originated from the tantalum clamps that were illuminated by a small fraction of the UV light. Below 600°C the Ta was oxidized and thus exhibited no Fermi edge.

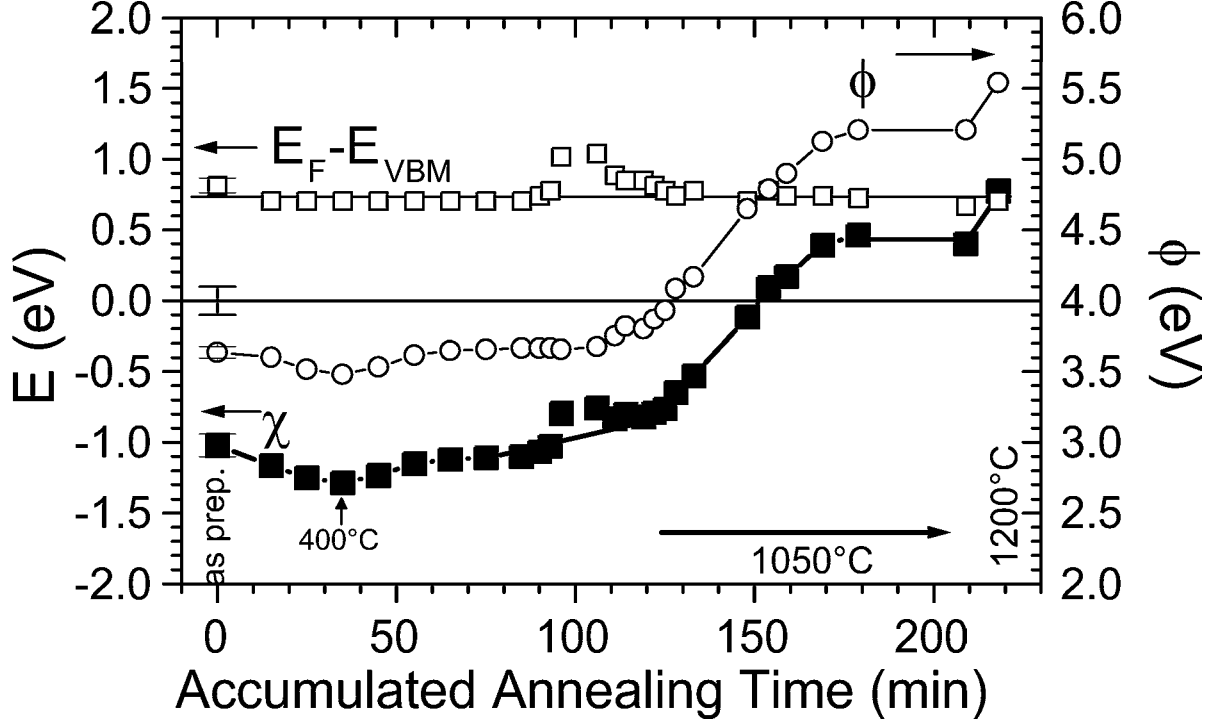


Figure 4.3: Evolution of band bending  $E_F - E_{VBM}$  (open squares), work function  $\phi$  (open circles), and electron affinity  $\chi$  (filled squares) of the plasma hydrogenated (100) surface during the annealing sequence.

In Fig. 4.3  $E_F - E_{VBM}$  (open squares), the work function  $\phi$  (open circles) and the electron affinity  $\chi$  (filled squares) are plotted versus the accumulated annealing time  $t_A$ . Up to  $t_A = 120$  min the temperature was raised in steps to nominally 1000°C. Beyond that point the temperature was kept constantly at 1050°C. Throughout the whole experiment the LEED pattern remained unchanged 2x1; after the final 1200°C step the background intensity increased slightly indicating the beginning of surface graphitization. Moreover, the lateral extension of well ordered domains was reduced as witnessed by weak streaking of the half ordered spots. The *statistical* error in  $\chi$  as determined by the uncertainty in the UPS and the CPD measurements was  $\pm 0.04$  eV; a *systematic* uncertainty of  $\pm 0.1$  eV originated mainly from the determination of the VBM

relative to the sp-peak as discussed in Chapter 2.1.1. From an initial value of -1.0 eV for the “as-prepared” state,  $\chi$  decreased for the first annealing steps reaching a minimum of -1.3 eV at 400°C and rose thereafter to -0.8 eV after 120 min of annealing. Starting the isothermal annealing sequence at 1050°C the main change in electron affinity took place until  $\chi = +0.5$  eV. For the last heating step at 1200°C a further increase of +0.3 eV to  $\chi = +0.8$  eV was measured.

Except for the initial value of  $\chi$  for the “as-prepared” surface, results similar to those of Fig. 4.3 have been reproduced several times.

Throughout the experiments the surface Fermi level was pinned at  $0.8 \pm 0.1$  eV above VBM. Experiments reported by other groups [99, 100] and performed on other (100) samples by us showed that hydrogen adsorption and desorption may influence the Fermi level position at the surface. Typical values of  $E_F - E_{VBM}$  between 0.3 eV and 1 eV have been observed [100]. The pinned Fermi level observed in this study was possibly due to *extrinsic* defects located in the near surface region which had not been removed by the hydrogen plasma or the acid treatment. For a weakly p-doped diamond as used in our case a graphite content of 0.1% of the surface was sufficient to pin the Fermi level between 0.7 and 0.8 eV above VBM [88]. The presence of surface contamination by graphite was supported by total photoelectron yield spectroscopy as will be discussed in the appendix of this thesis.

Before surface graphitization of the hydrogenated surface occurred as indicated by LEED above nominally 1100°C, the saturation value of  $\chi = +0.5$  eV was that of the clean (100)-(2x1) surface. This is in good agreement with theoretical predictions (see Table 4.1). However, higher values of +0.75 eV [101] and in particular +1.3 eV [102] were derived by others from the width of valence band photoemission spectra. As already mentioned in Chapter 2.1.1., the determination of the VBM of diamond with an accuracy better than 0.2 eV is difficult in UPS. In addition, a reliable value for the vacuum level is difficult to obtain from the low energy cut-off of the spectra because the spectral shape depends sensitively on the analyzer characteristic in this regime. Whether the higher values reported for the clean surface are thus due to experimental deficiencies or to different surface treatments is hard to say.

When graphitization occurred after the 1200°C step  $\chi$  increased by 0.3 eV to 0.8 eV. This situation was identical for the graphitized (111) diamond surface where a value of  $\chi = +0.80$  eV was observed [85].

The initial value of  $\chi$  of the plasma hydrogenated surface varied between -1.0 eV (Fig. 4.3) and -0.6 eV after nominally identical preparation conditions. However, the minimum value  $\chi_{min} = -1.3$  eV after 400°C annealing in UHV has been confirmed several times. In this temperature range, airborne hydrocarbon contaminations are known to desorb as reported by Graupner *et al.* [54]. We therefore attribute  $\chi_{min}$  to the contaminant-free C(100)-(2x1):H surface,

a value that is virtually identical to that of C(111)-(1x1):H [93]. Hence, the dipole-induced change  $\Delta\chi$  (see Fig. 4.1) of 1.8 eV is 0.1 eV larger for C(100) than for C(111) (Table 4.1). According to the lower surface carbon density and the tilt-angle of about  $25^\circ$  [63] of the C-H bonds the dipole density is about 20% lower on C(100) compared to C(111). Within the simplest electrostatic model of independent dipoles one would thus expect the same 20% difference in  $\Delta\chi$  of the two surface orientations. However, this is partially compensated by a smaller depolarization influence of adjacent C-H-dipoles at the less dense (100) surface as explained in the following.

The dipole-induced lowering of  $\chi$  is expressed by the areal density  $n$  of the C-H dipoles and their projected dipole moment  $p_z$  [103] according to

$$\chi = \chi_0 - \frac{e}{\epsilon_0} p_z n f(n). \quad (4.3)$$

$z$  is the direction perpendicular to the surface,  $\epsilon_0$  the dielectric constant of free space and  $e$  the elementary charge, respectively. The function  $f(n)$  accounts for the depolarization effects. In the mutual field  $\underline{E}$  of all dipoles the individual dipole moment

$$\underline{p} = \underline{p}_0 + \underline{\alpha} \underline{E} \quad (4.4)$$

is reduced<sup>1</sup> from its value  $\underline{p}_0$  at infinite dipole dilution by the bond polarizability  $\underline{\alpha}$  which is a tensor in general. In the case of a square or hexagonal plane network of dipoles oriented perpendicular to the plane, Topping [104] derived a simple expression for  $f(n)$  as

$$f(n) = \left( 1 + \frac{9}{4\pi\epsilon_0} \alpha n^{1.5} \right)^{-1} \quad (4.5)$$

where  $\alpha$  is the polarizability along the dipole axis and thus a scalar. With Eq. 4.5 the dependence of  $\chi$  with hydrogen coverage was successfully evaluated for the C(111) surface by Cui *et al.* [93]. As a first approximation, Eq. 4.5 was also used for the (100) configuration though the real geometry differed from that assumed by Topping. The solid line in Fig. 4.4 is a fit to the isothermal annealing sequence at  $1050^\circ\text{C}$  of Fig. 4.2 according to Eq. 4.3 and Eq. 4.5. Assuming first order desorption kinetics of hydrogen from diamond (100) [105] the time dependence of the H-coverage is given by  $n(t_A) = n_0 e^{-\nu t_A}$ , where  $n_0$  is the surface density of hydrogen atoms after hydrogen plasma preparation and  $t_A$  the annealing time, respectively. It is further assumed that the surface was fully hydrogenated after plasma preparation, i.e. each surface carbon atom was bonded to one hydrogen atom, and thus  $n_0$  equals the surface density of carbon atoms ( $1.57 \times 10^{15} \text{cm}^{-2}$ ) when a minimum of  $\chi = -1.3 \text{ eV}$  was measured.

---

<sup>1</sup> $\underline{E} \propto -\underline{p}_0$



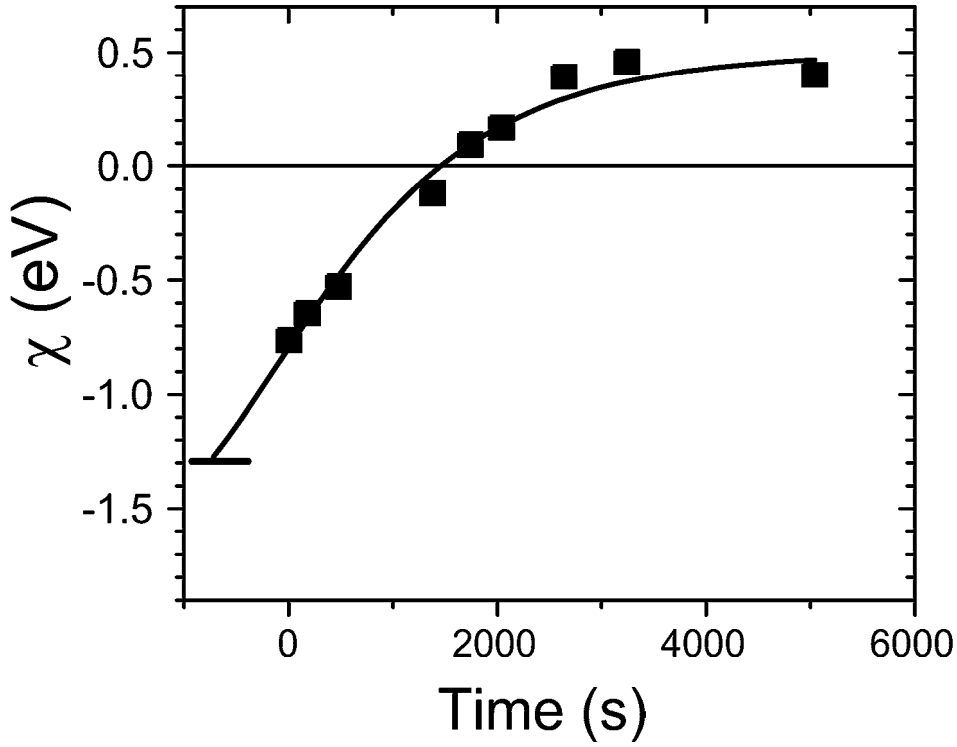


Figure 4.4: Electron affinity  $\chi$  versus annealing time at 1050°C during hydrogen desorption; the solid line is a fit to the data points with a dipole moment  $p = 0.08 \text{ e}\text{\AA}$  and a polarizability  $\alpha = 1.0 \times 10^{-30} \text{ Asm}^2/\text{V}$  (see text).

The desorption rate  $\nu$ , the coverage  $n(t = 0)$  at the beginning of the isothermal annealing sequence, and the dipole moment  $p_z$  are fit-parameters. The so derived C-H dipole moment of  $p_z = (1.32 \pm 0.04) \times 10^{-30} \text{ Asm}^2/\text{V}$  ( $0.08 \text{ e}\text{\AA}$ ) is 10% lower than on the hydrogenated C(111) surface as expected on account of the tilt angle. However, agreement with experiment requires a polarizability  $\alpha$  of  $(1.0 \pm 0.1) \times 10^{-30} \text{ Asm}^2/\text{V}$  which is about 30% lower than that given by Cui *et al.* for C(111)-(1x1):H [93]. This is not unreasonable because the polarization of the C-H bond is certainly smaller for any direction that does not coincide with the bond axis. Hence, the depolarization perpendicular to the surface that is considered in Eq. 4.5 is smaller for the (100) than for the (111) configuration on account of the tilted C-H axis on the (100) surface. Our findings corroborate *ab initio* calculations of Robertson *et al.* ([106] in Table 4.1). They also predict a larger variation of  $\chi$  between the clean and the hydrogen terminated C(100) surface compared to C(111).

## 4.4 Electron affinity of the chemically oxidized (100) surface

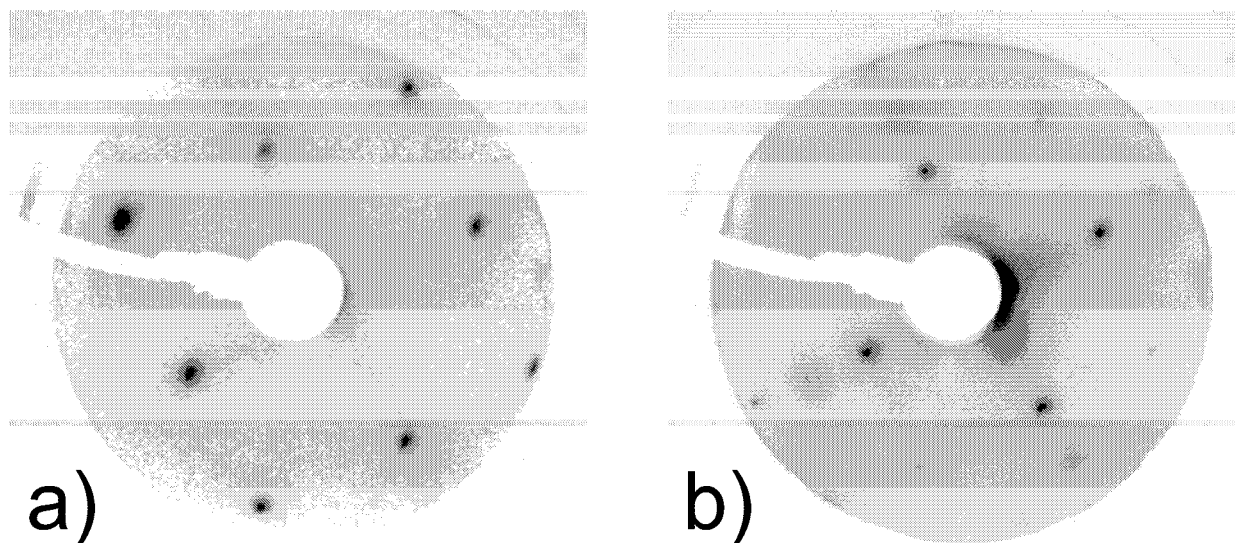


Figure 4.5: a) LEED pattern of the chemically oxidized C(100) surface ( $E=112$  eV).  
b) During annealing up to  $800^{\circ}\text{C}$  diffraction intensity in the vicinity of the half order spot positions has increased ( $E=170$  eV).

A similar experiment as it has been described in Section 4.3 was performed for the chemically oxidized diamond (100) surface. After UHV annealing for complete dehydrogenation the sample was boiled in  $\text{HNO}_3$  and  $\text{H}_2\text{SO}_4$ . LEED of the “as-prepared” surface showed a (1x1) pattern with a diffuse background intensity that was higher than in the case of the hydrogenated (100) surface. In addition, very weak streaking in the direction of the half-order spot positions as shown in Fig. 4.5a were observed. During annealing the half-order spot intensities increased with a diffuse background intensity that was higher than for the hydrogenated surface as shown in Fig. 4.5b.

XPS revealed oxygen as the only adsorbate.  $E_F - E_{VBM}$  was taken from the C1s binding energy relative to  $E_F$  by subtracting 283.9 eV as shown in Chapt. 2.1.1 and 2.1.2. As before, changes in work function and in band bending were monitored during annealing at different temperatures by Kelvin probe measurements and photoemission.

Fig. 4.6 summarizes the relevant quantities for the annealing sequence of the oxidized sample. No changes in band bending were observed up to nominally  $900^{\circ}\text{C}$  with a VBM position of about 0.8 eV below  $E_F$  which was virtually identical to that of the hydrogenated sample. From the CPD measurements the

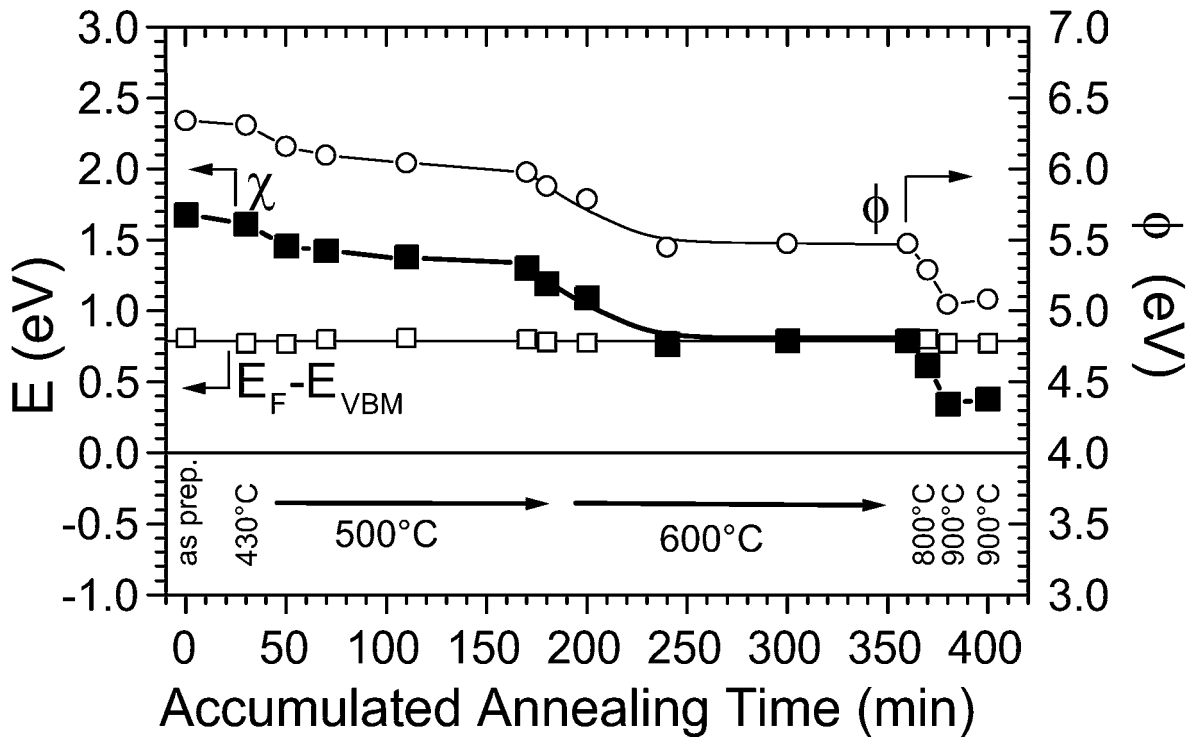


Figure 4.6: Evolution of band bending  $E_F - E_{VBM}$  (open squares), work function  $\phi$  (open circles), and electron affinity  $\chi$  (filled squares) of the chemically oxidized (100) surface during the annealing sequence.

work function  $\phi$  started to decrease from 6.3 eV within the 500°C isothermal annealing sequence. This trend was accelerated at 600°C until  $\phi$  reached a value of 5.5 eV. At higher temperatures (800 and 900°C)  $\phi$  dropped to its final value of 5.1 eV. On the basis of Eq. 4.2 the electron affinity  $\chi$  followed this behavior dropping from its initial value of +1.7 eV down to +0.4 eV.

The analysis for the oxidized sample differed from the hydrogenated case in that a direct correlation between changes in  $\chi$  and oxygen coverage was possible. The latter is obtained with an accuracy of about 10% from the ratio of the O1s to the C1s intensities taking the different cross sections for photoionization [42] and the effective sampling depth of 9Å [35] into account. The initial oxygen coverage after the acid treatment (first O1s spectrum in Fig. 4.7) corresponded to nominally 1.4 monolayer (ML). After a 430°C annealing step the oxygen coverage had dropped to about 0.8ML. However, the oxygen that was directly bonded to diamond did not change during the first annealing step. This part of oxygen gave rise to a C1s component in XPS that was shifted by 2.5 eV towards higher binding energies relative to the C1s level of bulk diamond (arrow in Fig. 4.7) and it remained unaffected up to 430°C annealing. The initially desorbed oxygen fraction is thus ascribed to a water layer

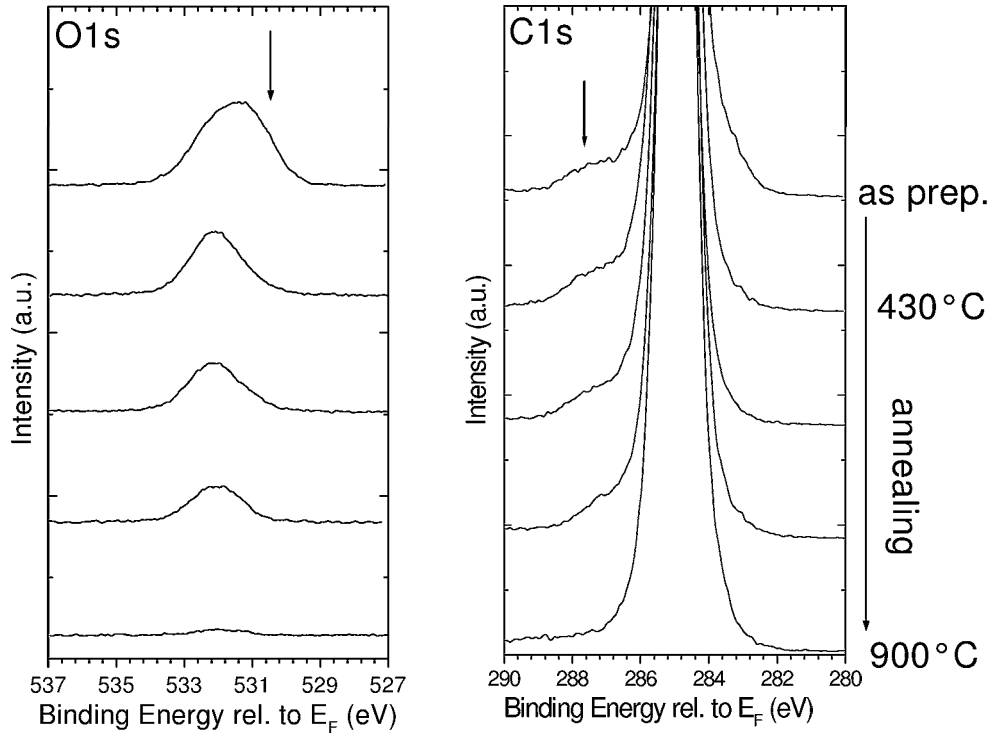


Figure 4.7: Selected O1s (left) and C1s (right) spectra of the *as prepared* sample after acid treatment and during annealing, respectively ( $\hbar\omega = 1486$  eV, electron emission angle  $\vartheta = 55^\circ$ ). The chemically shifted C1s component (arrow) decreases proportional to the main O1s line. The low-energy O1s shoulder (arrow) of the *as prepared* surface that has vanished after the first annealing step at nominally  $430^\circ\text{C}$  shows no correlation with the chemically shifted C1s component.

that was present after the acid treatment. This is in keeping with the observation that  $\chi$  did not change after this annealing step if we assume the water molecules to be randomly oriented at the surface. During the following annealing steps the O1s and the chemically shifted C1s component decreased in the same proportion. Consequently, the correlation between oxygen coverage and  $\chi$  in Fig. 4.8 started after the  $430^\circ\text{C}$  step. The solid line in Fig. 4.8 is a fit to the experimental values of  $\chi$  according to Eqs. 4.3 and 4.5 yielding a perpendicular dipole moment  $p_z = -(0.10 \pm 0.03) e\text{\AA}$  of the C-O bonds and a polarizability  $\alpha = (2.0 \pm 0.1) \times 10^{-40} \text{Asm}^2/\text{V}$  that is close to the polarizability of carbon monoxide ( $2.2 \times 10^{-40} \text{Asm}^2/\text{V}$  [107]). Based on the Pauling electronegativities [37] of carbon (2.55) and oxygen (3.44) a charge transfer  $\Delta q$  of  $0.17e$  is estimated, and thus our measured dipole moment corresponds to a thickness of the C-O dipole layer of  $0.6\text{\AA}$ . This is in excellent agreement with LEED-IV-studies

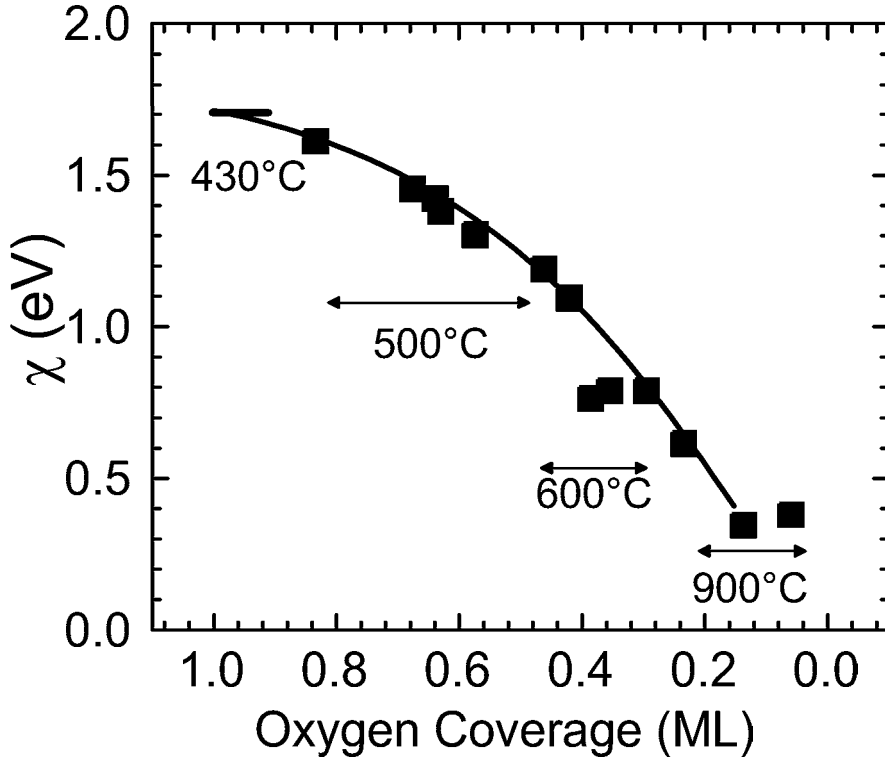


Figure 4.8: Dependence of  $\chi$  versus oxygen coverage as derived from the ratio of O1s to C1s core-level intensities; the solid line is a fit to the data with a dipole moment  $p_z = -0.10 e\text{\AA}$  and a polarizability  $\alpha = 2.0 \times 10^{-30} \text{Asm}^2/\text{V}$  (see text)

by Wang and co-workers [91]. They find on thermally oxidized (100) surfaces a C-O layer spacing of  $0.7\text{\AA}$  where the oxygen occupies the bridge position (see ether configuration in Fig. 4.1). A comparison of our experimental values of  $\chi$  with the theoretical results of Robertson and Rutter [106] (Table 4.1) also indicates that the bridge place of the chemically oxidized (100) surface is favored. Scaling the calculated electron affinity differences  $\Delta\chi_{theory}$  between the clean and the hydrogenated (100) and (111) surfaces by the factor 0.7 to fit the experimental values of this work and that of Cui *et al.* [93], the theoretical values provide an electron affinity of +2.0 eV for the (100)-(1x1):O<sub>ether</sub> surface and +3.0 eV for the (100)-(1x1):O<sub>ketone</sub> geometry. Thus, our experimental value of  $\chi = +1.7$  eV clearly favors bridge-oxygen as bonding configuration.

Extrapolating the fit curve of Fig. 4.8 to zero oxygen coverage one deduces an electron affinity of the bare surface of  $-0.1 \pm 0.1$  eV. This is considerably lower than the 0.5 eV obtained after hydrogen desorption and it was concluded that the acid treatment did leave some residual hydrogen chemisorbed at the surface which lowered the electron affinity by an offset of 0.5 eV throughout the whole annealing sequence. For that reason  $\chi$  increased again at the last 900°C

step when hydrogen started to desorb simultaneously with oxygen (Fig. 4.6). This was supported by the LEED pattern that exhibited from the beginning very weak diffraction intensity at the half order spot positions (Fig. 4.5) which are characteristic for the hydrogenated (100) surface. Consequently, a fully oxidized (100) surface should have an electron affinity of 2.2 eV which also agrees better with the theoretical value of 2.0 eV discussed above for the ether configuration. For reasons that are not clear at the moment such a high value had never been achieved in any of the experiments.

Finally, it should be mentioned that the chemical oxidation works quite effectively on the plasma hydrogenated surface as well which is shown in Fig. 4.9. After plasma treatment ( $\chi=-0.7$  eV) and mild annealing to desorb hydrocar-

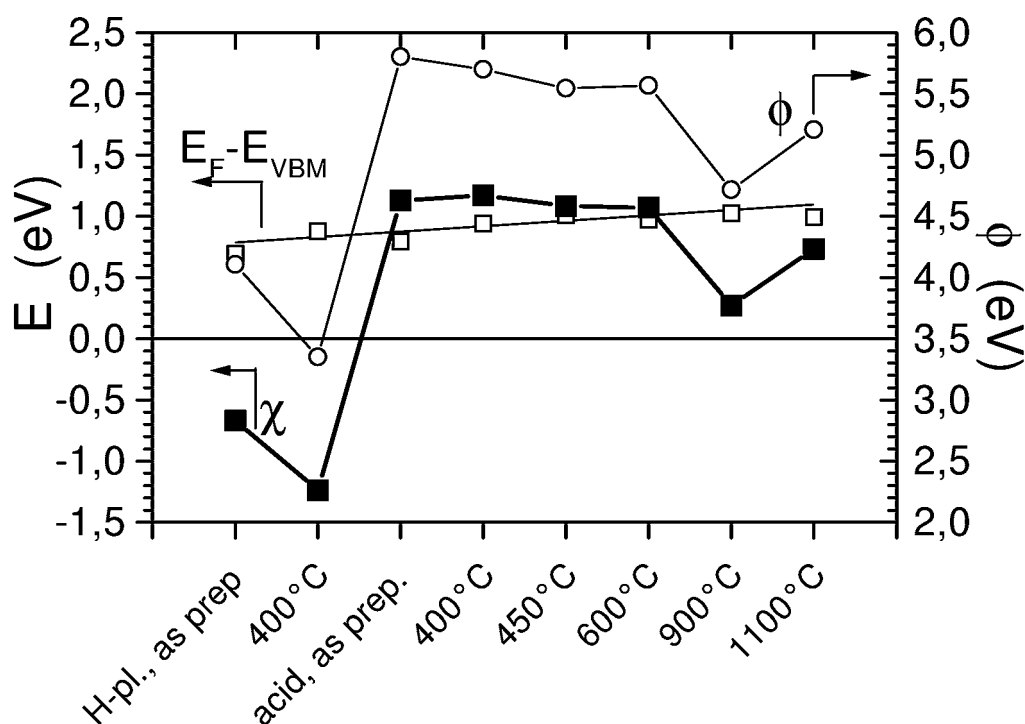


Figure 4.9: Band bending  $E_F - E_{VBM}$  (open squares), work function  $\phi$  (open circles), and electron affinity  $\chi$  (filled squares) of the plasma hydrogenated and additionally oxidized (100) surface (for details, see text).

bons ( $\chi=-1.3$  eV) the sample was removed from UHV and boiled in acid for half an hour. The resulting electron affinity of +1.2 eV proved a partial oxidation of the surface. Subsequently annealed up to 900°C the surface was free of oxygen but still partially covered with hydrogen ( $\chi = +0.3$  eV). For the last annealing step performed at 1100°C  $\chi$  increased again to its final value of +0.7 eV when the dehydrogenated surface was partially graphitized.

As demonstrated by this experiment, it should be possible to adjust quasi-continuously the electron affinity of the (100) diamond by combined hydrogen and oxygen adsorption. Starting from the hydrogenated surface a large variation of  $\chi$  from -1.3 eV up to 1.7 eV by the use of controlled oxidation parameters (time, temperature, acid concentration etc.) offers a simple way to manipulate  $\chi$ -related properties such as surface conductivity, Schottky barrier heights, and onset-field in fieldemission.

Table 4.1: Summary of electron affinities of clean, hydrogen and oxygen covered diamond surfaces.

(sc: natural single crystal type IIb; homo: homoepitaxial boron doped CVD-film; HF-H *in situ* hydrogenation via hot filament; P-H/P-O: *ex situ* plasma hydrogenation/oxidation; UHV-A: Annealing in UHV)

Diamond	Sample Preparation	$\chi$ in eV	Reference
(111)-(2x1)	sc UHV-A	$\approx 0.5$	[99]
	sc UHV-A	0.5	[101]
	sc UHV-A(1000K)	0.38	[93]
	sc UHV-A	1.5	[102]
(111)-(1x1):H	sc HF-H	$\leq -0.7$	[99]
	sc chem. oxidized, P-H	$< 0$	[101]
	sc P-H	$\leq -0.9$	[102]
	sc P-H	-1.27	[93]
(111) graphitized	sc UHV-A(1400K)	0.80	[85]
(111)-(2x1)	theory	0.35	[106]
(111)-(1x1):H	theory	-2.03	[106]
(100)-(2x1)	sc UHV-A	0.75	[101]
	sc UHV-A	1.3	[102]
(100)-(2x1):H	sc UHV-A	<u>0.5</u>	this work
	sc P-H	$\approx -0.8$	[108]
	sc HF-H	$\approx -0.4$	[109]
	sc P-H	$\leq -1.0$	[102]
	homo P-H	0.19	[91]
	sc P-H	<u>-1.3</u>	this work
(100)-(1x1):O	sc chem. oxidized	$\approx 1.0 - 1.5$	[101]
	homo P-O	$\approx 0.64$	[91]
	sc chem. oxidized	<u>1.7</u>	this work
	sc O-terminated	<u>2.2</u>	this work
(100)-(2x1)	theory	0.51	[106]
(100)-(2x1):H	theory	-2.05	[106]
(100)-(1x1):O <sub>ether</sub>	theory	2.61	[106]
(100)-(1x1):O <sub>ketone</sub>	theory	3.64	[106]



## 4.5 Summary

One of the outstanding properties of hydrogenated diamond surfaces is the negative electron affinity  $\chi$ . In contrast to C(111)-(1x1):H with  $\chi = -1.3$  eV [93] absolute values for the technologically more important C(100)-(2x1):H surface were missing. By studying the diamond (100) surface with photoemission and work function measurements we were able to measure values of the electron affinity of the clean C(100)-(2x1) (+0.5 eV) and the hydrogenated C(100)-(2x1):H (-1.3 eV) surface with an accuracy of  $\pm 0.1$  eV. An analysis of the electron affinity in the framework of adsorbate induced dipole layers shows good agreement with experimental findings when depolarization effects are taken into account. From the change of  $\chi$  during thermal annealing vertical dipole moments of the C-H ( $0.08 \pm 0.01$  eÅ) and the C-O ( $-0.10 \pm 0.01$  eÅ) bonds are derived. For the plasma hydrogenated surface it is shown that physisorbates (most probably hydrocarbons) increase the electron affinity by a few tenths of an electron volt compared to the contamination-free, hydrogenated surface. The measured electron affinity of the chemically oxidized C(100) of +1.7 eV represents a lower limit for a purely oxidized (100)-(1x1):O diamond surface because residual hydrogen provided by the acid treatment could not be avoided. From the magnitude of the C-O dipole the bridge-site bonding configuration of oxygen on the C(100) surface could unambiguously be determined. In addition, the influence of adsorbed hydrogen and oxygen on the electron emission properties of diamond (100) were investigated by total photoelectron yield spectroscopy. It is shown that electrons excited with sub-band gap light mainly originate from graphitic patches that develop during thermal annealing.



# Chapter 5

## Diamond-Metal Interfaces

### 5.1 Introduction

For technological applications the interface between semiconductors and metals is of vital importance. It is this interface region that determines whether the contact exhibits rectifying (finite barrier for charge transfer) or ohmic (vanishing barrier) properties. In particular, it was shown in Chapter 1 that both, rectifying contacts (=Schottky contacts) and ohmic contacts can be produced just by the choice of metals evaporated on hydrogenated diamond surfaces for metal-semiconductor field effect transistor (MESFET) devices.

For a p-type semiconductor as in the case of boron doped diamond, this energy barrier that is known as “Schottky barrier height” (SBH) is defined by the energy difference between the Fermi level and the VBM position at the interface of the semiconductor  $E_F - E_{VBM,interface}$ .

The general concept of metal-semiconductor barriers is discussed by Bardeen [110]. When both, the metal and the semiconductor, are well separated from each other the band alignment is defined by the common vacuum level as illustrated at the top of Fig. 5.1. When they are nearly joined a double layer is formed that consists of a space charge region extending into the semiconductor in the order of tens to hundreds of nanometers and an induced surface charge layer at the metal surface. Forming a junction, the two Fermi levels align as required for thermodynamic equilibrium as shown in the bottom part of Fig. 5.1. Within the Schottky-limit [111] the SBH is then determined by the work function  $\phi$  of the metal and the electron affinity  $\chi$  of the semiconductor, as illustrated in Fig. 5.1

$$SBH = E_g + \chi - \phi \quad (5.1)$$

where  $E_g$  is the gap energy of the semiconductor. This model relies on the fact that both surfaces remain unchanged when brought into contact and thus

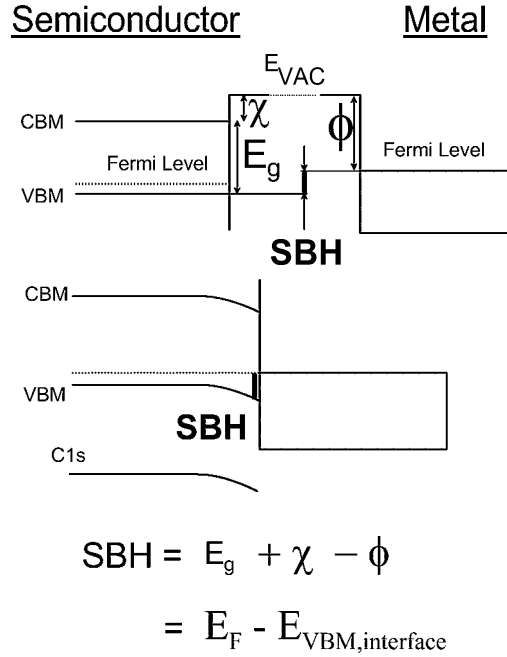


Figure 5.1: Band diagram illustrating the formation of a Schottky barrier for a p-type semiconductor in the framework of the Schottky-limit. Separating the semiconductor and the metal by a vacuum layer (top) yields the band alignment condition via the common vacuum level. A real semiconductor-metal interface exhibits a band profile similar to that sketched in the lower figure. Within the Schottky-limit, the value of the Schottky barrier height (SBH) is the same as derived for the case of the vacuum interface. The evolution of the band bending during Schottky barrier formation is being followed through the change in C1s core level binding energy measured relative to the Fermi level.

no modifications of the initial surface dipole densities occur. In this case, the full contact potential between metal and semiconductor as determined from the difference in initial work functions drops over the semiconductor by band bending; due to the small screening length of the order of Å in metals [45] the electric field does not penetrate into the metal. The linear correlation of the SBH in Eq. 5.1 with  $\phi$  and  $\chi$  is known also as “electron affinity rule” and was first proposed by Mott and Schottky in the late thirties of the last century [112, 113].

As already pointed out by Bardeen [110] intrinsic surface states or extrinsic defect states of the semiconductor strongly influence the surface Fermi level position of the semiconductor. Moreover, interface states in the gap region of the semiconductor can even be induced only by the presence of the metal. They are thus called *metal induced gap states* (MIGS) (an introduction in MIGS is

Table 5.1: Values of the SBH in eV of gold, magnesium, and aluminium on hydrogenated ( $\chi = -1.3$  eV) and clean ( $\chi = +0.5$  eV) expected for diamond surfaces in the framework of the electron affinity rule (work functions  $\phi_{poly}$  of the three polycrystalline metals are taken from Ref. [107]). In addition, the results of this work are provided to compare with the theoretical values.

		Au	Mg	Al
Affinity rule	$\phi_{poly}$ (eV)	5.1	3.7	4.3
	SBH ( $\chi = -1.3$ eV)	-0.9	+0.5	-0.1
	SBH ( $\chi = +0.5$ eV)	+0.8	+2.3	+1.6
		Metal	SBH (eV)	Contact
This work	Diamond			
	C(111)-(1x1):H	Au	$+0.3 \pm 0.1$	Ohmic
	C(100)-(2x1):H	Mg	$+0.8 \pm 0.1$	Schottky
	C(111)-(1x1):H	Al	$+0.7 \pm 0.1$	Schottky
	C(111)-(2x1)	Al	$+0.7 \pm 0.1$	Schottky

given in Refs. [37, 114]). In the extreme case of Fermi level pinning, the SBH becomes independent of the work function of the metal which is usually referred to as “Bardeen-limit”. For diamond surfaces it is shown by Ristein [38] that the density of states provided by a graphitic content of one percent of a monolayer is sufficient to pin the Fermi level 0.8 eV above VBM.

The SBH formation is always a compromise between the two extreme situations of the Schottky- and the Bardeen-limit: maintaining the interface dipole layer that is induced by the electron affinity of the semiconductor and the work function of the metal on the one hand, and, on the other hand, to weaken the dipole layer via charge transfer into available interface states. Only when this latter tendency is weak the affinity rule provides reasonable values for the SBH. Finally, it should be mentioned that there is still a controversial debate concerning real junctions. Among others, a detailed description of the effects involved is provided by Tung [115] and by Henisch [116]. Both authors emphasize the role of the individual semiconductor-metal system with its characteristic morphological and chemical contact properties, interdiffusion possibilities, oxide interlayers, and lateral inhomogeneous charge distributions. They can significantly influence the value of the SBH.

Nevertheless, the results in the forthcoming chapter will go some way to justify that the Schottky-limit is a good starting point to deal with gold, aluminium and magnesium on diamond - at least on hydrogenated diamond - surfaces.

From Eq. 5.1 a lower limit for the work function follows that yields a vanishing SBH on p-type diamond and thus an ohmic contact between diamond and the metal. On hydrogenated diamond ( $\chi = -1.3$  eV) this minimum work function equals 4.2 eV, and on hydrogen-free diamond ( $\chi \approx +0.5$  eV) it equals 5.9 eV. Therefore, all metals with work functions larger than 4.2 eV should

exhibit ohmic contacts on p-type diamond terminated by hydrogen. A number of metals that fulfill this condition has been investigated on hydrogenated diamond [117]. The experiments show that only noble metals (Pt, Au, Ag, Cu) follow this rule whereas more reactive metals (e.g. Ni, Al, Sn) form Schottky barriers on hydrogenated diamond surfaces despite the fact that their work functions are larger than 4.2 eV. A straightforward hypothesis is that noble metal deposition maintains the hydrogen termination at the interface in contrast to the more reactive metals. It is the purpose of the present investigation to test this hypothesis for the case of gold, magnesium, and aluminium. The SBHs expected for these three metals on the basis of Eq. 5.1 are listed in Table 5.1. In addition, the results of this work are shown, too. Gold and aluminium were chosen because they are used as source and drain contacts (Au) and as gate electrodes (Al) in field effect transistors that are based on the surface conductivity of hydrogenated diamond [22, 90]. Due to the high chemical reactivity of aluminium and magnesium, these metals are able to form carbides and hydrides [74, 118] and are thus good candidates to test our hypothesis of dehydrogenation of the diamond surface during metal deposition. In addition, Mg is the only metal among the selected three metals that is predicted to exhibit Schottky contacts even on hydrogenated diamond according to the affinity rule (see Table 5.1). Reported values of the SBH of magnesium on as-grown and thus hydrogen terminated CVD films (0.94 eV [119] and 0.73 eV [120]) are fairly large compared to other metals on hydrogenated diamond surfaces [117, 119, 121] corroborating the special role of Mg.

## 5.2 Experimental details

As shown in Fig. 5.1, PES is able to determine the SBH by the measurement of the VBM relative to  $E_F$  at the interface. This method requires *a priori* homogeneous metal overlayers with thicknesses that are in the order of the electron escape depth (typically 5-20 Å). The VBM position is inferred by the binding energy of the sp-peak in UPS or by the C1s core-level in XPS as it has been explained in Chapter 2.1.1 and 2.2.2.

Prior to metal evaporation, all mechanically polished (111) and (100) natural single crystals of type IIb (boron concentration  $10^{16}$  cm<sup>-3</sup>) were hydrogenated in a hydrogen plasma. The metals were deposited at evaporation rates of typically 3 - 6 ML/h at room temperature under ultra high vacuum (UHV) conditions and the photoemission measurements were performed without exposing the sample to air. For gold on C(111):H core level spectroscopy was performed at the PM5 beamline of the Berlin synchrotron source BESSY I taking advantage of the variable surface sensitivity that was achieved by adjusting the exciting photon energy. In the case of Mg on C(100):H ARUPS data were taken at the TGM-4 beamline at BESSY I. The Al experiments were car-

ried out using a monochromatized and microspot focussed Al-K $_{\alpha}$  X-ray source for core level spectroscopy (XPS). Except for gold on C(111):H a quartz crystal monitor was used to quantify the evaporated film thickness.

## 5.3 Results and discussion

### 5.3.1 Gold on hydrogenated C(111)

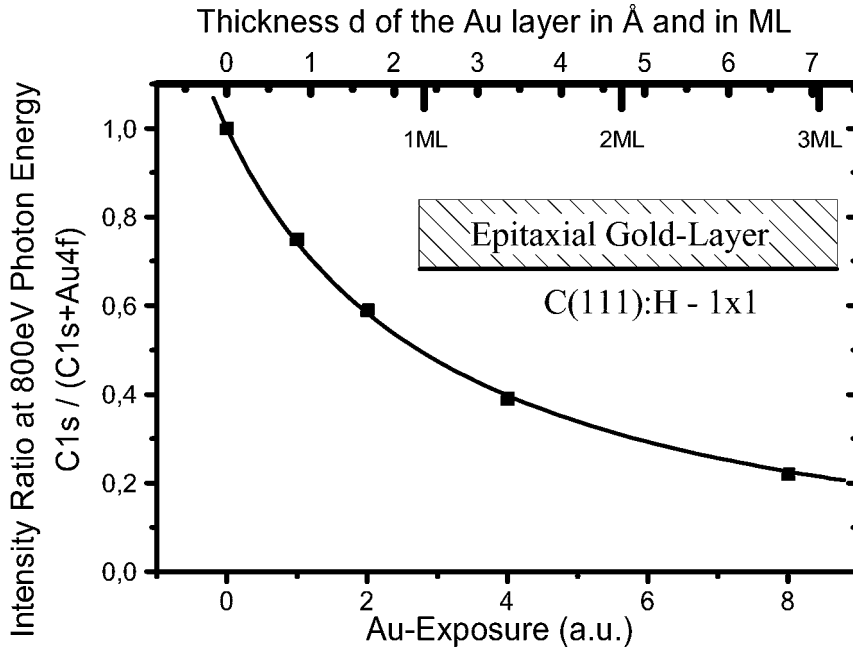


Figure 5.2: Ratio of the relative C1s core level intensities (taken at 800 eV photon energy) during gold deposition on a hydrogenated (111) single crystal diamond. The line represents the best fit to the data points using a layer-by-layer growth model (insert). On top, the derived Au coverages are given in Å and in monolayer equivalents (ML), respectively.

In Fig. 5.2 the intensity ratio of the C1s core level to the sum of the C1s and Au4f lines is plotted versus gold exposure (one unit represents 30 min at a constant evaporation rate). Under the assumption of layer-by-layer deposition the intensity ratio is described by

$$\frac{I_{C1s}}{I_{C1s} + I_{Au4f}} = \frac{1}{1 + \frac{\sigma_{Au4f}\rho_{Au}}{\sigma_{C1s}\rho_C} (\exp(d/\lambda) - 1)} \quad (5.2)$$

with the appropriate core level cross sections  $\sigma$  and the atomic densities  $\rho$  of diamond and gold, respectively [42]. The solid line in Fig. 5.2 is a fit of the

data to Eq. 5.2. On the basis of the excellent fit a layer-by-layer growth mode appears to be strongly favored in this deposition regime. Fitting parameter is the layer thickness  $d$  measured in units of the electron mean free path  $\lambda$  which is about 14 Å [35] for both core levels ( $h\nu = 800$  eV). The absolute film thickness so determined is indicated at the top of Fig. 5.2 in Å and in monolayer (ML) gold coverage, respectively. Our findings of layer-by-layer growth confirm the results of O. Küttel and co-workers [122] derived from X-ray photoelectron diffraction. They observed the formation of polycrystalline gold overlayers on hydrogenated (100) single crystals even at low metal coverages.

Next, we investigated the evolution of the Au induced band bending. Fig. 5.3 shows the C1s core level spectra taken at 330 eV photon energy ( $\lambda \approx 5$  Å [35]). The binding energies are referred to the Fermi level by recording the spectrum of a reference gold foil simultaneously after each preparation step. From the

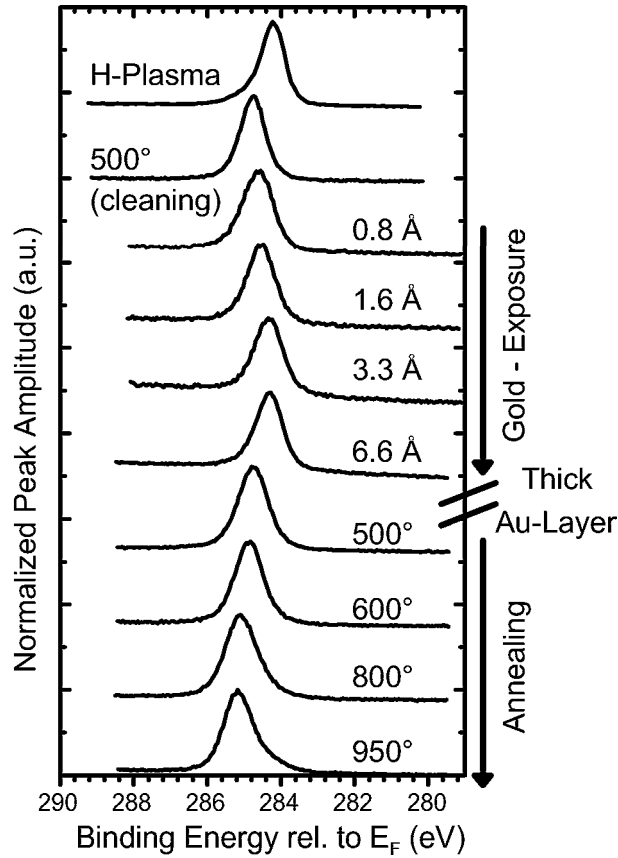


Figure 5.3: C1s core level spectra ( $h\nu = 330$  eV) recorded for the initial steps of gold deposition and after subsequent annealing steps of a thick gold film. The binding energy is referred to  $E_F$  of a reference gold foil.

C1s binding energies so determined,  $E_F - E_{VBM}$  was obtained by subtracting  $283.9 \pm 0.1$  eV which equals the C1s binding energy relative to VBM as was



shown in Chapter 2.1.2.  $E_F - E_{VBM}$  is plotted as a function of gold exposure and annealing on the right ordinate of Fig. 5.4. The freshly prepared diamond (top spectrum) exhibited a C1s binding energy of  $284.1 \pm 0.1$  eV corresponding to a position of the surface Fermi level of  $0.2 \pm 0.1$  eV above VBM. After a  $500^\circ\text{C}$  annealing step, the C1s binding energy increased by 0.6 eV signaling a downward band bending by the same amount. During the addition of Au up to 3ML (120 min evaporation step in Fig. 5.3) the C1s line moved gradually back towards lower binding energy as shown in the first half of Fig. 5.4.

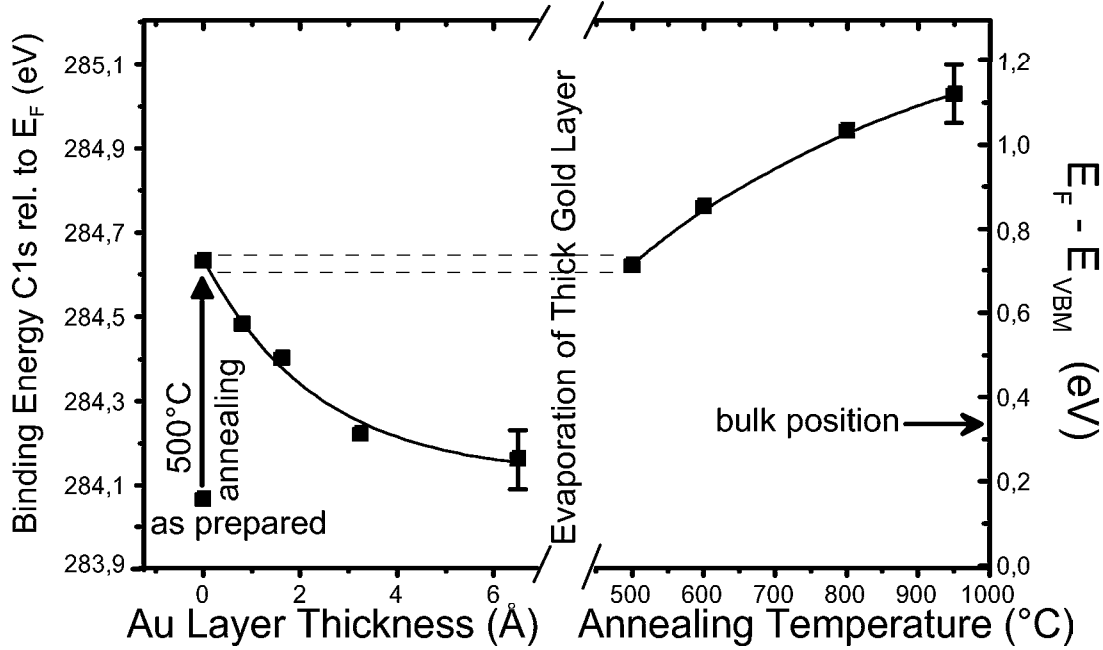


Figure 5.4: Evolution of band bending as a function of gold coverage and as a function of annealing temperature in the case of the thick gold film. The bulk Fermi level position of 0.32 eV of boron doped diamond is also indicated.

The absence of any chemically shifted components on the C1s line in Fig. 5.3 indicates that the shift is not related to the formation of chemical bonds between diamond and gold. The binding energy shift corresponds thus to a Au overlayer induced band bending. For 3ML Au coverage, the final interface Fermi level position is returned to  $0.3 \pm 0.1$  eV above VBM as shown in Fig. 5.4. In fact, this SBH does not constitute an actual barrier for hole transport because it is very close to  $E_F - E_{VBM}$  in the bulk for boron doped diamond (0.32 eV [38]). The ohmic contact characteristics derived from our spectroscopic investigations are in good agreement with transport measurements reported by other groups [117].

Finally, a thick gold film (about 50 nm) was deposited and the C1s core level could no longer be detected as demonstrated by the first spectrum in

Fig. 5.5. However, after a subsequent annealing step at 500°C, the C1s line was visible again by XPS at the same binding energy as it had been prior to gold deposition (second spectrum of Fig. 5.5). The following annealing sequence up to 950°C yielded C1s core level spectra (950°C spectrum in Fig. 5.5 and last four spectra in Fig. 5.3) which were in position and shape identical to those measured previously on merely hydrogenated and annealed diamond surfaces [54]. The weak shoulder at the lower binding energy side of the 950°C spectrum in Fig. 5.3 indicates the onset of  $\pi$ -bonding as hydrogen began to desorb. This has already been described for the C(110) surface in Chapter 3. Hence, no influence of gold was observed in the C1s core level spectra. The intensity of the Au4f line was also unaffected during the annealing sequence (Fig. 5.5).

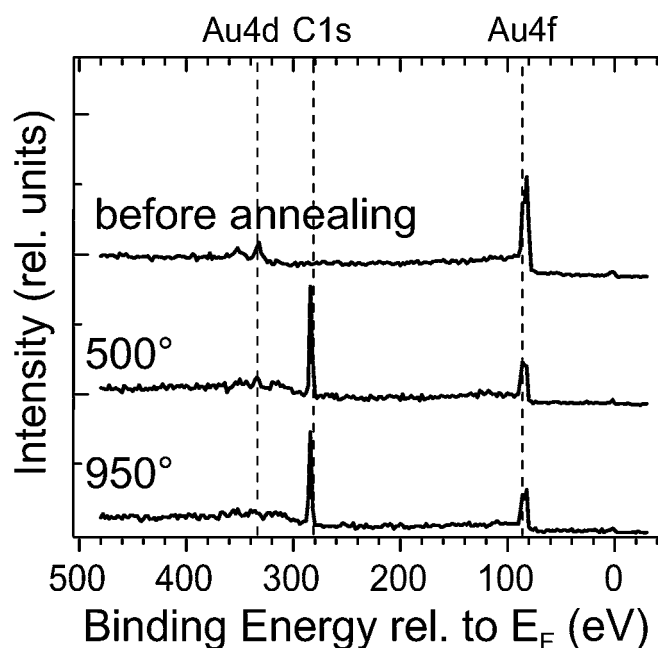


Figure 5.5: C1s and Au4f spectra during annealing of the thick ( $\approx 50$  nm) gold overlayer ( $h\nu = 800$  eV)

The reason for this behavior is the formation of gold islands after annealing at 500°C as demonstrated by the secondary electron micrographs (SEM) shown in Fig. 5.6. Although the gold covered area seemed to form a closed layer in the overview graph (Fig. 5.6a), it was obvious under higher magnification (Fig. 5.6b) that the gold layer consisted of islands of about 200 nm diameter and about 200 nm height as measured by Atomic Force Microscopy (AFM). From the ratio of the Au4f and C1s core levels a mean gold coverage of 15% of the diamond area was calculated which was similar to the ratio of the gold covered area to the total area in Fig. 5.6b. The area between the islands

appeared brighter in SEM on account of the higher yield in secondary electrons of diamond compared to that of the Au islands. Indeed, the non covered area exhibited about the same brightness as the parts that were protected from gold by the fixing clamps.

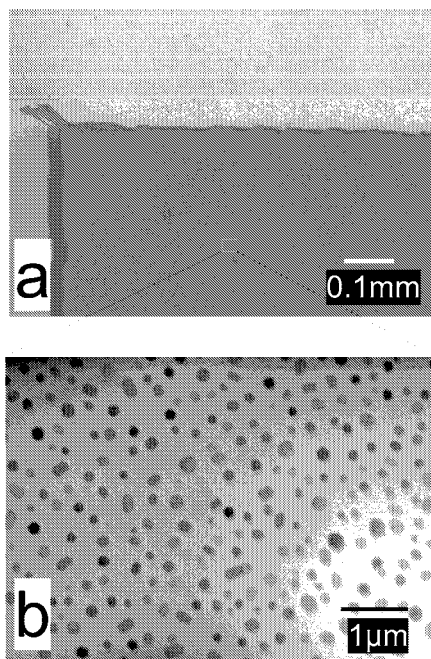


Figure 5.6: Secondary electron micrograph overview (a) of the gold covered diamond sample after  $950^{\circ}\text{C}$  annealing. The bright border region is non-covered diamond that has been protected by Ta clamps during gold deposition. At higher magnification (b), the bright diamond area in between the gold islands (dark spots) reveals that hydrogen still exists at the surface (b).

A very high secondary electron yield is characteristic for hydrogenated diamond surfaces with negative electron affinity as was demonstrated in Ref. [123]. It is reasonable to assume that hydrogenation has remained intact under the Au overlayer, a conjecture that is supported by the results of an annealing step at  $1100^{\circ}\text{C}$  in UHV, a temperature at which hydrogen is known to desorb completely [85]. At this point, the SEMs in Fig. 5.7a) and b) do indeed show a reversal in brightness between diamond with now positive electron affinity and the Au islands (b); the size of the islands was reduced by about a factor of two and the intensity of the Au4f line relative to that of the C1s line was reduced accordingly. Also, the islands were highly mobile. Scratching the sample surface with tweezers left traces free of gold at the surface and large gold clusters at the borders without damaging the diamond surface otherwise (Fig. 5.7c).

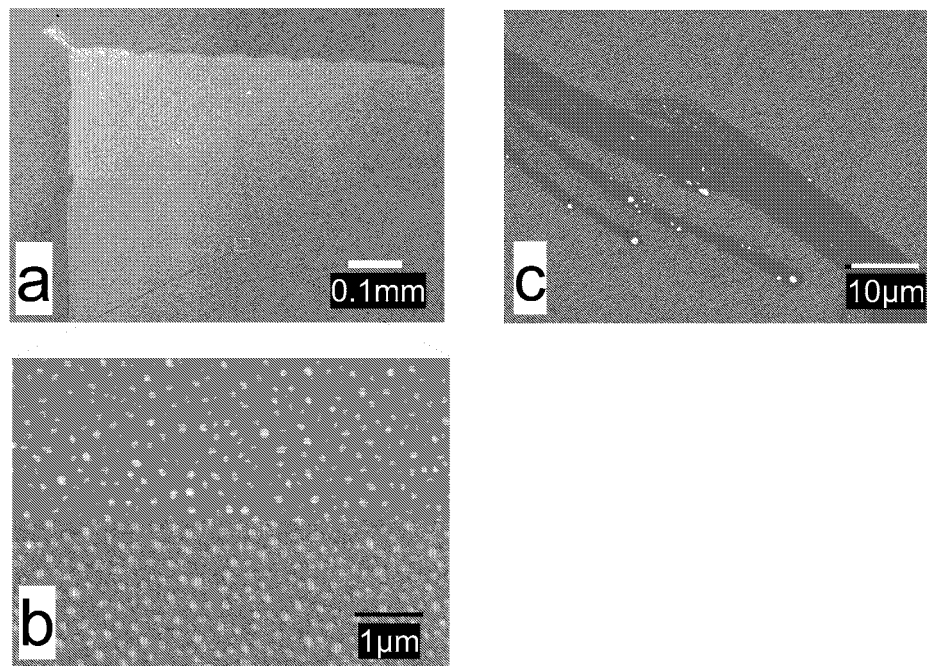


Figure 5.7: The reversal in SEM contrast after the 1100°C annealing step reveals that hydrogen had been desorbed (a,b). The SEM in part c was taken after scratching the surface with tweezers.

In order to remove the residual gold contamination, the diamond was boiled for 10h in *aqua regia* under conditions where a massive gold wire was dissolved within seconds. This treatment reduced the XPS gold signal to about 0.1% of its initial value but it was not possible to remove it completely. SEM and AFM both showed indeed the existence of some residual islands which were in some cases massive; in the majority of the cases, however, they were forming ring-like structures of 100-200 nm diameter as shown in Fig. 5.8. Whether this unexpected passivation of gold against the attack of *aqua regia* was induced by the diamond, by the annealing process, or both is not clear at present.

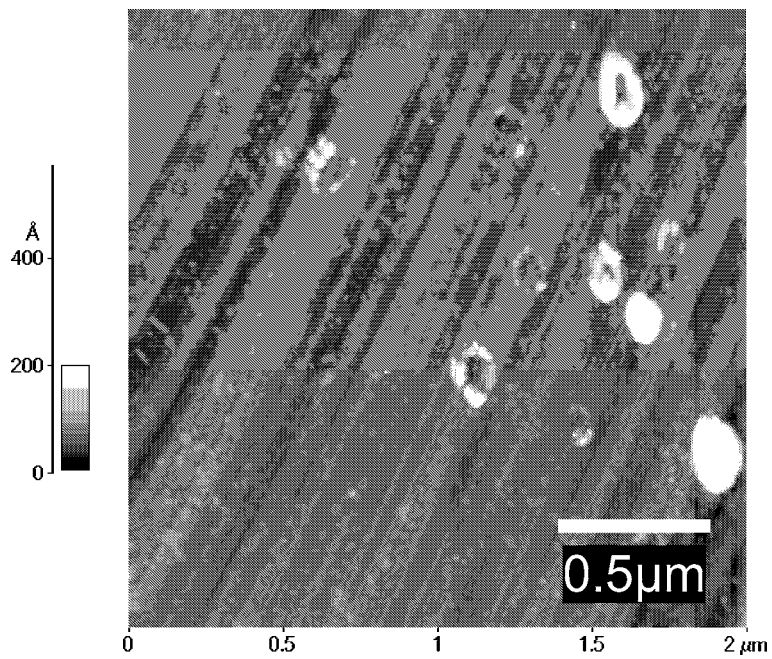


Figure 5.8: The atomic force micrograph of the surface after boiling in *aqua regia* for 10 hours still shows gold contamination in the form of massive islands and rings (typical size: 100-200 nm).

### 5.3.2 Magnesium on hydrogenated C(100)<sup>9</sup>

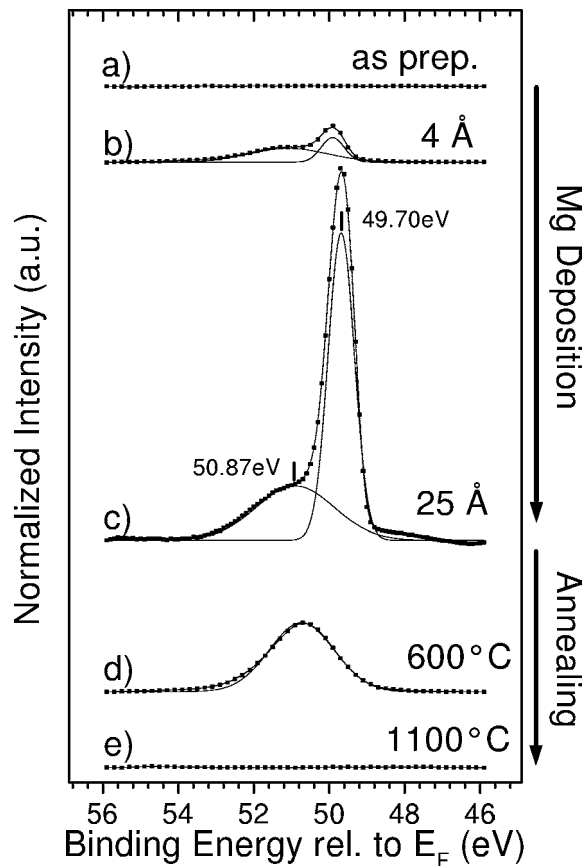


Figure 5.9: Magnesium 2p core level spectra before (a), during Mg deposition (b, c), and subsequential annealing at 600°C (d) and 1100°C (e), respectively ( $h\nu = 100$  eV). All spectra are normalized to the incident photon flux.

The hydrogen plasma treated C(100)-(2x1) surface was first annealed in UHV at 500°C to desorb physisorbates. Magnesium was then evaporated from a Knudsen cell in two steps. The amount of deposited Mg of 4Å and 21Å Mg was estimated from the quartz thickness monitor. Fig. 5.9 depicts the corresponding Mg 2p core level spectra (a-c). Although the chamber pressure never exceeded  $1 \times 10^{-9}$  mbar during deposition time, a fairly high magnesium-oxide contribution was identified by the broad component shifted +1.2 eV towards higher binding energies compared with the main line. At a nominal Mg coverage of 25Å the binding energy of 49.7 eV of the metallic Mg component relative to  $E_F$  is that of bulk magnesium [124]. Thereafter, the sample has been annealed for half an hour at 600°C and 1100°C (spectrum d and e in Fig. 5.9). Already after annealing at 600°C, the metallic Mg component had vanished whereas the oxide component remained unaffected. The latter was

also desorbed at 1100°C. At this temperature hydrogen was expected having desorbed as well. In all cases, the Mg2p core level spectra did not show shifted components that could be interpreted as due to a chemical interaction of Mg with the surface.

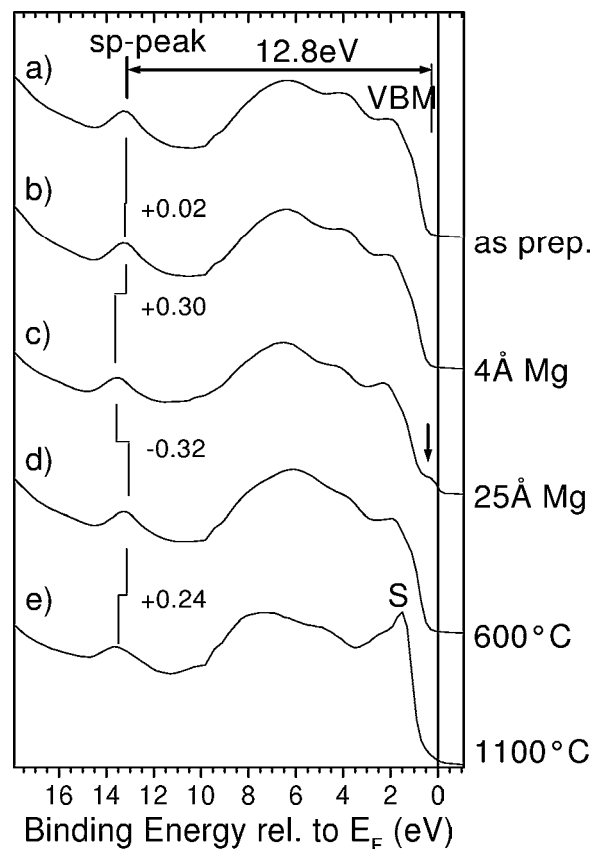


Figure 5.10: Angle-integrated valence band spectra during deposition (the nominal Mg coverage is indicated on the left side) and annealing of the magnesium film ( $h\nu = 40$  eV). All spectra are normalized to their maximum intensity. The arrow at spectrum c) indicates the Fermi edge, and thus the metallic character of the thick Mg film.

An indication of hydrogen preservation at the interface is derived from UPS. Taken at 40 eV photon energy the angle-integrated valence band spectra in Fig. 5.10 indicate band bending effects only. After the second evaporation step the Fermi edge in spectrum c) in Fig. 5.10 shows the metallic character of the Mg overlayer. At this point, the diamond valence band intensity has decreased to about half its original value as estimated from the maximum intensity at about 6.5 eV binding energy (not shown). When the metallic Mg component has been removed in the 600°C annealing step, the characteristic Fermi edge vanished as well, and spectrum d) of Fig. 5.10 is shifted back to the initial position before Mg deposition. Finally after the 1100°C annealing step the

surface state that is labelled S in Fig. 5.10 indicated the formation of  $\pi$ -bonded dimers after hydrogen desorption. Concurrently, an additional band bending of 0.24 eV towards higher binding energy occurred. Eventually, spectrum e) in Fig. 5.10 is identical to that of a dehydrogenated C(100) surface [55]. The position of the VBM relative to  $E_F$  as traced by the sp-peak is summarized in Fig. 5.11 for the whole sequence (right scale).

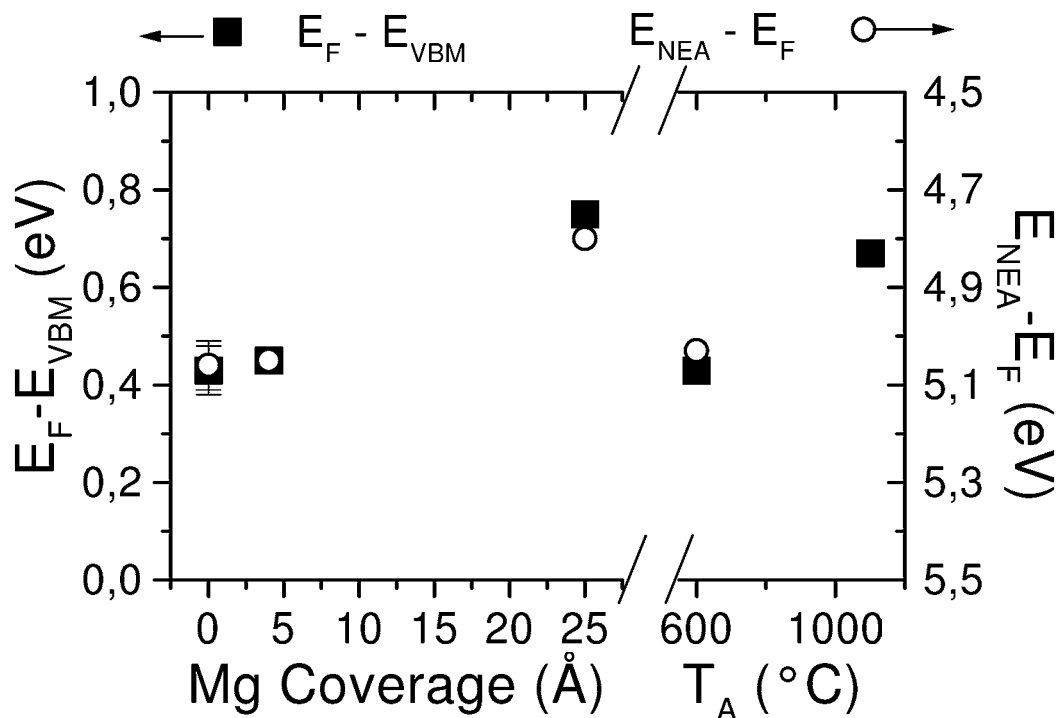


Figure 5.11: Evolution of band bending  $E_F - E_{VBM}$  as traced by the sp-peak in Fig. 5.10 (solid squares, left energy axis) and of the NEA-peak position  $E_{NEA} - E_F$  in Fig. 5.13 (open circles, right energy axis) during magnesium deposition and subsequential thermal annealing ( $T_A$ : annealing temperature).

In Fig. 5.12 angle-resolved spectra taken at 60 eV photon energy are shown. Remember electrons emitted from valence band states exhibit an escape depth  $\lambda$  lower than 10 Å [35]! However, even at a nominal coverage of 25 Å Mg angular dispersion of diamond valence band states were clearly visible. This contradicted the expected loss of  $k_{||}$ -conservation in ARUPS when a polycrystalline Mg overlayer has formed as pointed out in Chapter 2. These findings clearly point towards the formation of Mg islands rather than to the formation of a homogeneous Mg overlayer. Therefore, the valence band spectra of diamond originated from a surface between the metal islands that was uncovered by magnesium.



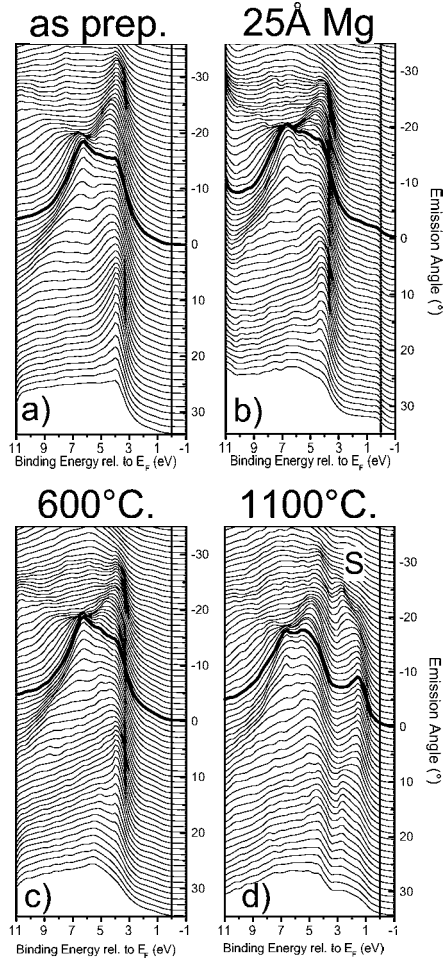


Figure 5.12: Angle-resolved spectra ( $h\nu = 60$  eV, azimuth: [011]) of the “as-prepared” surface (a), after the 25Å Mg deposition step, and after thermal annealing (c, d). All spectra show the dispersion of bulk states (a-c) and in addition that of surface states (labelled S in d).

Returning to the main subject of this chapter of hydrogen preservation during magnesium deposition, the absence of surface states after the 600° annealing step make the presence of large dehydrogenated areas unlikely. However, partial dehydrogenation cannot be excluded. In the work of Cui *et al.* [85] it is demonstrated that about 10% of hydrogen prevents reconstruction of the (111) surface. Nevertheless, the low-energy cutoff of the photoemission spectra may serve as a fingerprint for the remaining hydrogen coverage. Demonstrated by Himpsel and co-workers [92] and investigated in detail by Diederich *et al.* [100] the intense peak of secondary electrons on hydrogenated C(100) is a signature of the negative electron affinity state of the surface. On a NEA surface, thermalized electrons from the bottom of the CBM easily escape into the vacuum and thus give rise to the strong increase in electron intensity. This so-called

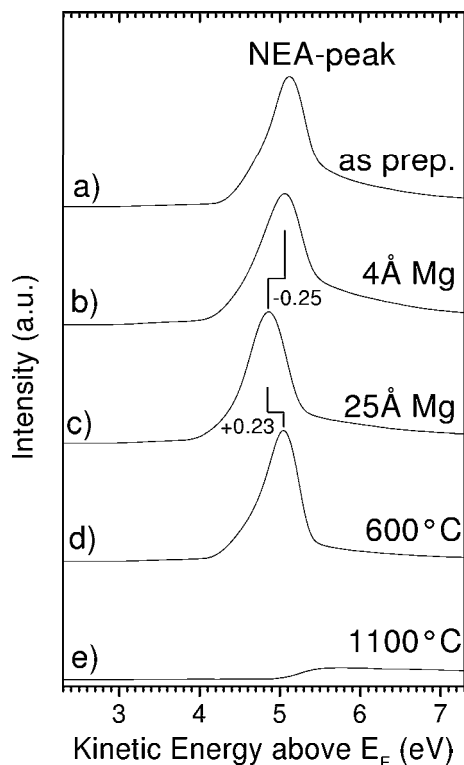


Figure 5.13: Spectra of the inelastically scattered electrons in the kinetic energy range of 2.3 to 7.3 eV during magnesium deposition and thermal annealing (excitation energy  $h\nu = 60$  eV). The “NEA-peak” at 5 eV indicates that the hydrogen coverage is mainly maintained until the last annealing step has occurred (Spectrum e).

“NEA-peak” of the spectra is visible as long as the electron affinity of the surface remains negative, i.e. as long as a considerable amount of hydrogen is still present.<sup>1</sup> As shown in Fig. 5.13, the NEA-peak remained clearly visible during Mg deposition and after the 600°C annealing step, respectively, indicating that the NEA-state of the surface was not affected by magnesium, i.e. the hydrogen termination was maintained as well. The rigid shift of the NEA-peak in energy (between spectrum b and c, and between c and d) occurred simultaneously to surface band bending as traced by the sp-peak in Fig. 5.10. In Fig. 5.11 the position of the NEA-peak  $E_{NEA}$  relative to  $E_F$  is plotted as well as  $E_F - E_{VBM}$ . The energy difference  $E_{NEA} - E_{VBM}$  equals  $5.5 \pm 0.07$  eV which is virtually identical to the band gap of diamond (5.47 eV); this is a confirmation that the majority of secondary electrons originated from the conduction band minimum of diamond.

After the desorption temperature of hydrogen, the NEA-peak vanished when

<sup>1</sup>The contribution of thermalized electrons at the conduction band minimum to the NEA-peak is thoroughly discussed in the appendix

the electron affinity changed its sign from negative to positive as indicated from the last spectrum in Fig. 5.13. Again: the disappearance of the NEA-state and thus of the hydrogen termination of the diamond surface, respectively, was not correlated to the presence or absence of magnesium.

From the position of the sp-peak in Fig. 5.10, a position of the VBM relative to  $E_F$ , and thus a SBH of 0.75 eV is obtained for the thick magnesium layer<sup>2</sup>. This value confirms results of other groups obtained by transport measurements [119,120] which is, at a first glance, surprising. On account of the three-dimensional island growth mode as deduced from the unchanged ARUPS data, the lateral metal-semiconductor contact is highly inhomogeneous. If the value of 25Å Mg as taken from the quartz thickness monitor is approximately correct, the reduction of the UPS intensity of diamond by the factor of two at this stage would suggest that half of the diamond was not covered by islands while the Mg islands had an average height of 50Å. This was at least a factor of 4 higher than the mean electron escape depth and diamond underneath Mg was thus not seen by photoemission. Therefore, the change in band bending that was traced by the sp-peak in UPS and the SBH of 0.75 eV deduced from  $E_F - E_{VBM}$  were measured on the surface part that was free of Mg and not at the interface between diamond and magnesium as required. There are, however, good arguments that  $E_F - E_{VBM} = 0.75$  eV measured inbetween the islands was only 0.1 eV smaller than the position of the VBM relative to  $E_F$  at the interface, i.e. the real SBH.

The situation of highly inhomogeneous Schottky contacts is not unusual. Depending on processing of real Schottky diodes, the ideality factor  $n$  of current-voltage curves measured can be significantly greater than unity ( $n = 1$  is required for an ideal Schottky diode) even when the SBH is not affected. These findings are - among other theoretical considerations - ascribed to the inhomogeneities of the Schottky barrier (see [115] and references therein). Working on laterally inhomogeneous Schottky barriers, Sullivan *et al.* [125] solved numerically the Poission equation in three dimensions in the case of a metal exhibiting a SBH= $E_{CBM} - E_F$  of 0.8 eV on n-type silicon with a donor density  $n_D$  that equals  $10^{16}\text{cm}^{-3}$ . This situation is comparable to our case of boron doped diamond where the acceptor concentration is  $10^{16}\text{cm}^{-3}$  as well [38]. Therefore, the results of Sullivan *et al.* that are shown in Fig. 5.14 are easily rescaled with respect to lateral and vertical dimensions by a factor of 1.4 taking the different Debye lengths of silicon and diamond into account<sup>3</sup>. Let's focus on the change of potential at the free surface which is shown on top of Fig. 5.14.  $E_F - E_{VBM}$  decreases laterally from the edge of the metal contact to the asymptotic value of the free surface which equals 0.32 eV in the case of diamond (flat band situa-

---

<sup>2</sup>The energy distance of the sp-peak to the VBM of 12.8 eV is taken from our previous work as shown in Chapter 4.

<sup>3</sup> $\lambda_{Debye,Diamond} = \sqrt{\epsilon_{Silicon}/\epsilon_{Diamond}} \cdot \lambda_{Debye,Silicon} = 1.4 \cdot \lambda_{Debye,Silicon}$

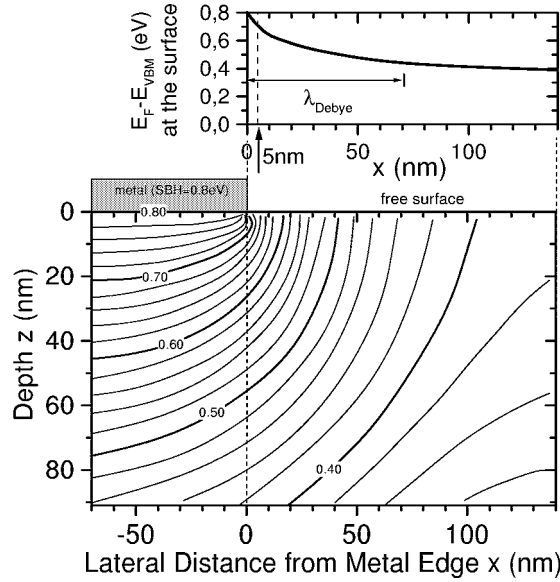


Figure 5.14: Bottom: Equipotential contour lines of a Schottky contact (SBH=0.8 eV) on p-type diamond (acceptor density:  $10^{16} \text{cm}^{-3}$ ) at room temperature as taken from Ref. [125]. Top: Position of the surface VBM  $E_{VBM}$  relative to  $E_F$  as a function of lateral distance to the metal edge according to [125].

tion). If the separation of the Mg islands on the surface is considerably smaller than the Debye length the change of  $E_F - E_{VBM}$  would also be small (the Debye length is the typical length over which charge screening occur [45]). Assuming a mean height of the islands that does not exceed their widths a mean height of the islands of  $50 \text{\AA}$  and a mean distance between them of the same order of magnitude, one could explain the decrease of the UPS intensity by the factor 0.5 for a film thickness of  $25 \text{\AA}$ . From Fig. 5.14 it is obvious that the lateral band bending from one island to its nearest neighbors at a mean distance of 5 nm cannot vary by more than  $0.1 \pm 0.05 \text{ eV}$  (see arrow in Fig. 5.14). Therefore, the lateral VBM position changes only slightly as sketched in Fig. 5.15 b, and  $E_F - E_{VBM}$  measured by means of UPS at the free surface is estimated to be at maximum 0.1 eV smaller than  $E_F - E_{VBM}$  at the interface. Taking all together,  $E_F - E_{VBM} = 0.75 \text{ eV}$  measured for nominally  $25 \text{\AA}$  Mg deposited on hydrogenated C(100) thus corresponds to a SBH of  $0.85 \pm 0.15 \text{ eV}$  which is in good agreement with values from the literature [119, 120].

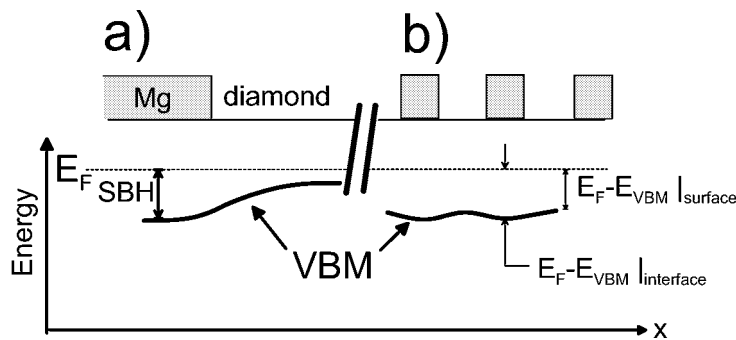


Figure 5.15: Sketch of the variation in lateral VBM position relative to  $E_F$  in the case of a single semi-infinite Mg island on a infinite boron doped diamond surface (a) and for isolated islands which are separated by a mean distance of 5nm (b). For details, see text.

### 5.3.3 Aluminium on hydrogenated and hydrogen free diamond (111)

In order to study the influence of hydrogen termination on the formation of the Al-diamond Schottky barrier, Al was evaporated on a diamond (111) surface that was partly hydrogenated while half of it was hydrogen-free. To this end, one half of a hydrogen plasma polished and thus hydrogen terminated surface, the crystal was masked, and on the unmasked half hydrogen was removed in UHV by electron beam induced desorption (2h at 0.8 keV, 0.6 A/cm<sup>2</sup>) as shown in Fig. 5.16. This method yields, unlike thermal desorption, a hydrogen-free

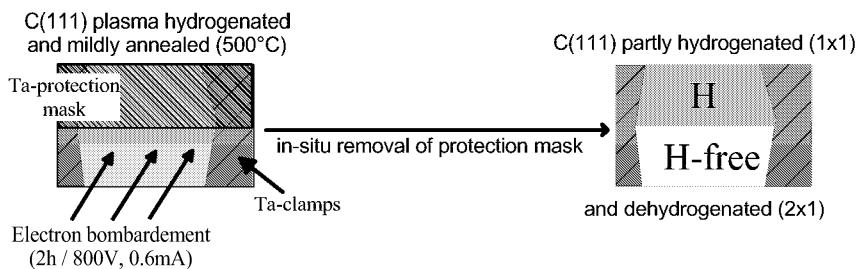


Figure 5.16: Experimental set up for partial hydrogen desorption that is induced by electron bombardment. Before electron bombardment, the sample has been annealed at 500°C to desorb contaminants.

surface without creating electrically active surface defects [85, 88]. The successful dehydrogenation of the unmasked half of the sample was indicated by a change from an unreconstructed (1x1) LEED pattern to a (2x1) pattern being characteristic for the hydrogen-free diamond (111) surface (see first LEED pat-

tern of series a) and b) in Fig. 5.17). After irradiation the mask was removed in UHV and Al was evaporated.

The (2x1) LEED pattern of the irradiated surface vanished after 3.3Å aluminium deposition whereas the (1x1) LEED pattern of the masked area was still weakly visible after a nominal coverage of 6.5Å as depicted in Fig. 5.17. Since the same amount of metal was deposited on both halves of the sample, these differences point towards island formation of Al on the hydrogenated part leaving parts of the diamond surface uncovered by the metal compared to the situation on the dehydrogenated one.

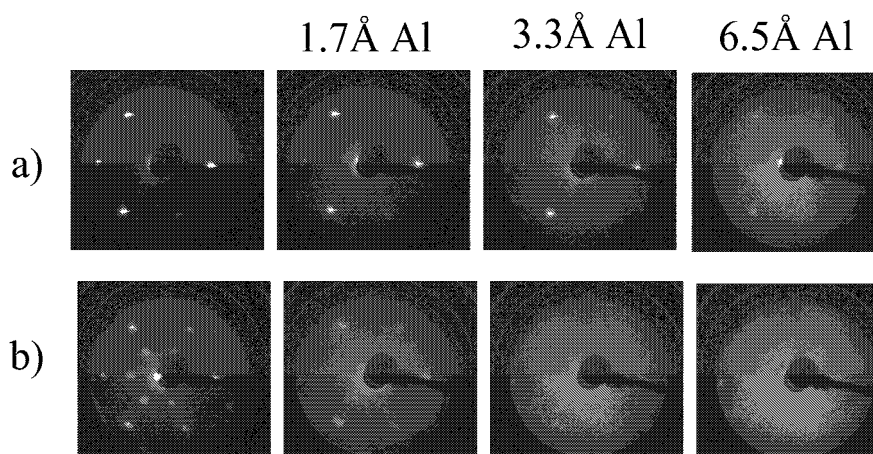


Figure 5.17: Evolution of the LEED pattern of the protected (series a) and the irradiated (series b) part of the sample during Al deposition ( $E=120$  eV).

Fig. 5.18 shows the C1s and Al 2p core level spectra as a function of overlayer thickness. Despite a base pressure below  $10^{-10}$  mbar, about half of the aluminium deposited on both parts of the sample has oxidized (see Al<sub>2</sub>O<sub>3</sub>-component in Fig. 5.18b) which has to be taken into account when interpreting the data. Most probably, this oxide contribution was due to the very low deposition rate of 4ML/h which gave sufficient time for the attack of residual oxygen within the chamber.

The existence of Al islands as indicated by LEED was supported by the relative core level intensities of C1s and Al2s which did not follow a layer-by-layer growth model as it was the case for gold on C(111):H in Section 5.3.1. However, similar to gold, no chemically shifted C1s components were observed (Fig. 5.18 a), neither on the masked nor on the dehydrogenated area, and thus there was no indication for carbon aluminium bonds at the interface. The small shifts of the C1s line as a function of Al coverage on both halves of the sample revealed only little surface band bending between diamond and the metal (metal/oxide) layer and were within the error margin of 0.2 eV independent

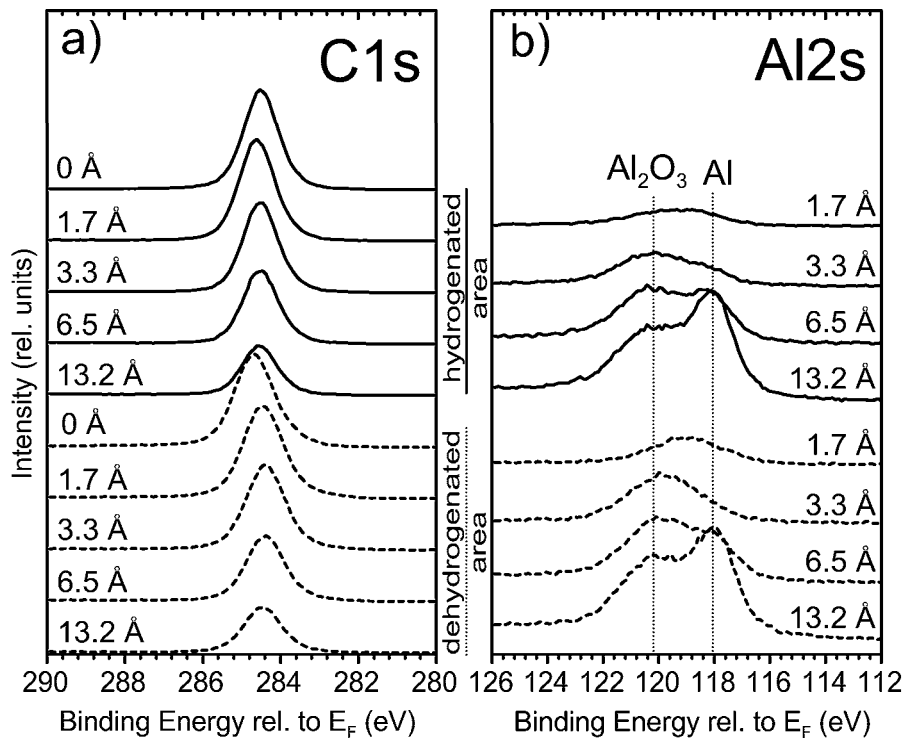


Figure 5.18: C1s (a) and Al2s (b) core level spectra ( $h\nu = 1486$  eV) during aluminium deposition on the hydrogenated (solid lines) and the dehydrogenated (dashed lines) part of a (111) single crystal. The nominal Al coverages are taken from the quartz microbalance situated next to the sample.

of the initial hydrogen coverage. As it was observed on C(100) in Chapter 4 the pinning of the Fermi level is most probably related to residual defects at the surface. However, the identical Fermi level position of both parts of the sample would also be consistent with our initial contention that Al might have removed hydrogen; but more direct evidence is needed here. From the mean C1s position at 284.6 eV a SBH of  $0.7 \pm 0.1$  eV follows which is smaller than the values between 0.8 and 1.5 eV published in literature [126]. Since most of the high SBH values were obtained on Al-diamond contacts prepared under inferior vacuum conditions the partial oxidation of Al is unlikely to be the cause of the discrepancy.

The SEM image of Fig. 5.19 taken after Al evaporation and exposure to air shows three regions of differing secondary electron yield. As expected, the brightest part of the sample (labelled “as prepared”) was that which was still fully hydrogen covered because it was protected from electron beam bombardment and Al deposition by tantalum clamps that fixed the sample. Al covered the central parts of the sample that are labelled “masked area” and “irradiated

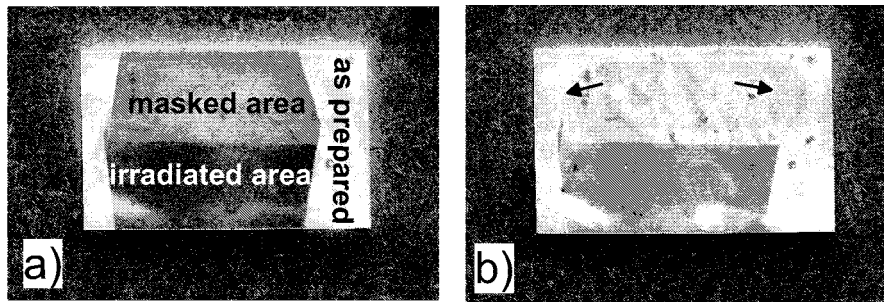


Figure 5.19: SEM images of the gold sample before (a) and after (b) removing the deposited Al layer. For details, see text.

area”. The irradiated and thus hydrogen-free area exhibited a lower secondary electron yield than the masked area which again pointed towards island growth of Al on hydrogenated diamond. However, no isolated islands were detected in SEM at higher magnification. After etching the aluminium layer completely away (10 min in 10% HCl-solution) the only contrast in SEM was observed between the irradiated and non-irradiated region of the sample (Fig. 5.19b). Especially at the borders of the tantalum clamps (arrows in Fig. 5.19b), no differences between hydrogenated areas were observed whether they were covered by Al or not.

As already mentioned in Section 5.3.1, secondary electron yield contrast on differently treated diamond surfaces is mainly related to the electron affinity of diamond. Therefore, the SEM image of Fig. 5.19b) strongly suggests that the hydrogen coverage at the surface was not significantly modified by the deposited aluminium / aluminium oxide layer.

The contradictory findings of photoelectron spectroscopy and SEM do thus not answer the question whether hydrogen is maintained at the Al-diamond interface.



## 5.4 Summary

In the context of electronic devices, the interface between a semiconductor and a metal is of decisive importance. The surface MESFETs that are based on the surface conductivity of hydrogenated diamond are realized by the evaporation of gold (as ohmic source and drain contacts) and of aluminium (as gate electrode exhibiting Schottky characteristics) on hydrogenated diamond surfaces [90]. In particular, the role of hydrogen at the interface between diamond and gold, magnesium, and aluminium and its effect on Schottky barrier heights has been investigated by photoemission.

Summarizing the main result for gold on hydrogenated diamond (111) surfaces, we find that all experiments clearly point towards the preservation of hydrogen at the gold-diamond interface under the conditions of our investigation. Gold evaporation at room temperature leads to layer-by-layer growth. The measured value of 0.3 eV for the Schottky barrier height (SBH) of gold on C(111)-(1x1):H does not constitute an energy barrier for hole transport from diamond to the metal, which is in agreement with transport measurements [117]. Annealing at moderate temperatures (500°C) transforms the Au layer into islands, re-exposing the hydrogenated diamond surface in between. The islands themselves are highly mobile and do suffer from good adhesion to the substrate. Nevertheless, they are highly inert against the attack of *aqua regia* in contrast to isolated gold.

As in the case of gold, we have no indication that the interface C-H dipole layer is attenuated by magnesium on C(100)-(2x1):H. Whether this fact is related to the presence of magnesium oxide as witnessed by the Mg 2p core levels has not been unambiguously resolved yet. Furthermore, the formation of three-dimensional islands is apparently favored, which points towards a low interface tension between C(100)-(2x1):H and magnesium. Taking the lateral inhomogeneous distribution of magnesium into account, a Schottky barrier height of  $0.85 \pm 0.15$  eV was deduced for a magnesium film of nominally 25Å thickness which matches the data from the literature [119, 120].

In order to study the influence of hydrogen termination on the formation of the aluminium-diamond Schottky barrier, aluminium was evaporated on a diamond (111) surface that was structured by electron bombardment and thus partly hydrogenated while half of it was hydrogen-free. A three-dimensional growth mode is likely for aluminium on diamond for the hydrogenated surface in particular. As it is the case for gold and magnesium no chemical interaction of aluminium with carbon has been detected by core level spectroscopy. In addition, no influence of aluminium on the interface hydrogen was observed in electron yield microscopy. The small shift of the spectra reveal minor charge transfer, both for the hydrogenated and the dehydrogenated surface. The measured value of the SBH of 0.7 eV is smaller than obtained by other groups [126].



## Chapter 6

# Surface Conductivity of Hydrogenated Diamond

In the final chapter of this thesis the phenomenon of the high p-type surface conductivity of hydrogenated diamond will be presented. As pointed out in Chapter 1, it is not only of fundamental interest to understand why diamond is the only semiconductor which exhibits this property. The surface conductivity can even be controlled by a gate and has been thus utilized to realize the metal-semiconductor field effect transistors (MESFET) [22, 90] presented in Chapter 1. It should be emphasized that this type of MESFET that is based on the surface conductivity is realized on undoped diamond, i.e. on a perfect insulator at room temperature. Furthermore, it is shown by Ri *et al.* [127] and by Denisenko *et al.* [29] that the surface conductivity is pH-sensitive.

It will be shown that the unique property of surface conductivity of hydrogenated diamond surfaces is related to charge transfer processes which occur at the interface of diamond in contact with a “natural” electrolyte.

### 6.1 General remarks concerning the surface conductivity of diamond

Undoped diamond with a gap of 5.5 eV is a *bona fide* insulator. Yet in 1989 Ravi and Landstrass reported a substantial surface conductivity of hydrogenated diamond surfaces, both of single crystals and of films prepared by CVD, respectively [12, 13]. These observations have been confirmed over the years [14–17, 20] and the current understanding is as follows [18, 19]. The surface conductivity of hydrogenated diamond is of the order of  $10^{-4}$  to  $10^{-5}\Omega^{-1}$  at room temperature (RT). The areal density of the p-type carriers responsible for

the conductivity is about  $\rho_S = 10^{12} - 10^{13} \text{ cm}^{-2}$  and it is hardly temperature dependent between 150 K and 500 K. The Hall mobility of the carriers varies also little with temperature ( $\sim T^{1.2}$ ) [23] and is of the order of  $30 \text{ cm}^2 \text{ V}^{-1} \text{ sec}^{-1}$  with a maximum value of  $400 \text{ cm}^2 \text{ V}^{-1} \text{ sec}^{-1}$  reported for a carrier density of  $2 \times 10^{12} \text{ cm}^{-2}$  [20]. These mobilities are not too different from those measured for B-doped diamond and there is thus general agreement that the carriers are holes residing in an accumulation layer at the surface [22].

The depth distribution of the acceptors responsible for the hole accumulation is discussed controversially, ranging from species at the surface [22, 23] over layers extending up to 10 nm into the diamond [18] (see Fig. 6.1a and b). It has even been suggested that the acceptors form a layer buried 30 nm below the surface [24] (Fig. 6.1c). Except for the latter scenario, the observed

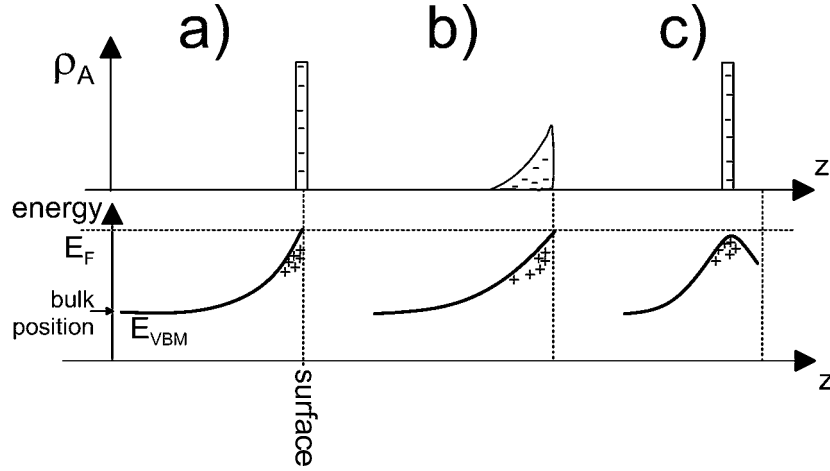


Figure 6.1: Top: Sketch of the three models discussed for the distribution  $\rho_A(z)$  of (negatively charged) acceptor states that are responsible for p-type surface conductivity of hydrogenated diamond: a surface layer (a), an extended surface layer (b), and a buried layer (c) of acceptors. In all cases, the depth integrated density  $\int \rho_A(z) dz$  amounts to  $10^{13} \text{ cm}^{-2}$  to account for the observed areal hole density in the accumulation layer of  $10^{13} \text{ cm}^{-2}$  holes.

Bottom: Sketch of the corresponding band profiles (for details, see text).

areal density of  $10^{13} \text{ cm}^{-2}$  holes requires a band profile such that the surface Fermi level position lies within a few  $kT$  at the valence band maximum (VBM) [22, 128] as shown in Fig. 6.1a) and b). Because the surface conductivity is only observed on hydrogenated diamond surfaces and disappears after dehydrogenation or oxidation of the surface, it has been assumed that hydrogen is directly responsible for the hole accumulation layer by forming particular but as yet unspecified defects that act as acceptors [18]. In addition, it has been

proposed recently that protons themselves are the main charge carriers causing the surface conductivity [129]. Due to the observed mobilities, however, the latter model seems to be highly unlikely, and is not considered further.

## 6.2 Investigation of the surface conductivity by transport measurements and spectroscopic methods

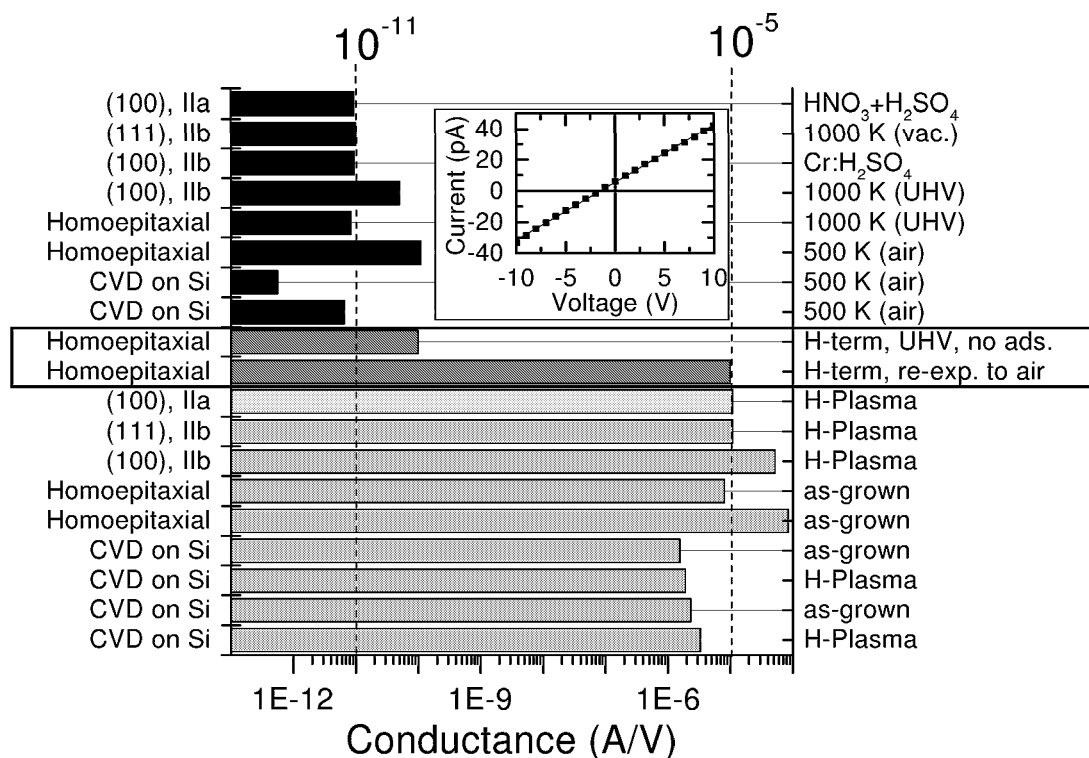


Figure 6.2: Surface conductance (SC) of a variety of diamond samples (left scale) after different types of surface treatments (right scale). It is measured by placing two gold tips on the samples; the values are derived from the slope of ohmic current-voltage curves. The insert depicts a typical I-V curve of a sample in its low conducting state ( $SC=4 \cdot 10^{-12} \text{ A/V}$ ). The framed data in the center refer to a undoped homoepitaxial diamond layer on a type Ib (100) substrate used for the UHV experiments described below.

The conductivity of altogether 10 diamond samples were investigated, namely, four undoped CVD films of variable crystalline quality on silicon substrates,

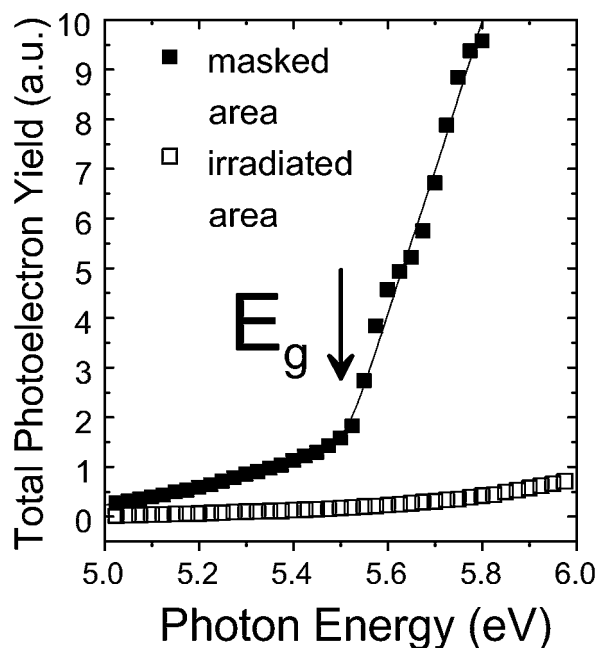


Figure 6.3: Total photoelectron yield spectra of the masked (filled squares) and the irradiated (hollow squares) part of the sample after electron bombardment. The protected area still shows a strong increase in yield intensity at the gap energy of diamond  $\hbar\omega = 5.5$  eV which is characteristic for NEA and thus for hydrogen termination whereas the flat spectrum of the irradiated part proves positive electron affinity and thus hydrogen desorption.

two undoped homoepitaxial layers on single crystals with (100) orientation of type Ib and IIb, respectively, two IIb (100) and (111) single crystals, and one IIa (100) single crystal. The conductivities were measured in air and under ultra high vacuum (UHV) by placing two gold tips with a distance of 2 mm onto the surface. The quantity quoted was the conductance that was determined from the slope of I-U measurements for  $-10 \text{ V} \leq U \leq +10 \text{ V}$ . Ohmic characteristics were measured in all cases (insert of Fig. 6.2). Irrespective of the kind of diamond all samples exhibited conductances between  $10^{-6}$  and  $10^{-4}$  A/V in the hydrogenated state whereas the low conductance after annealing in air above  $300^\circ\text{C}$  or after oxidation in  $\text{HNO}_3 + \text{H}_2\text{SO}_4$  was always below  $10^{-10}$  A/V. These conductances were - aside from a geometry factor of order unity - equal to the surface conductivities and the quoted values agreed with those reported in the literature for samples with and without surface conductivity, respectively. An overview of these measurements is shown in Fig. 6.2. At first view, these experimental findings seem to indicate that hydrogen termination is equivalent to high surface conductivity.

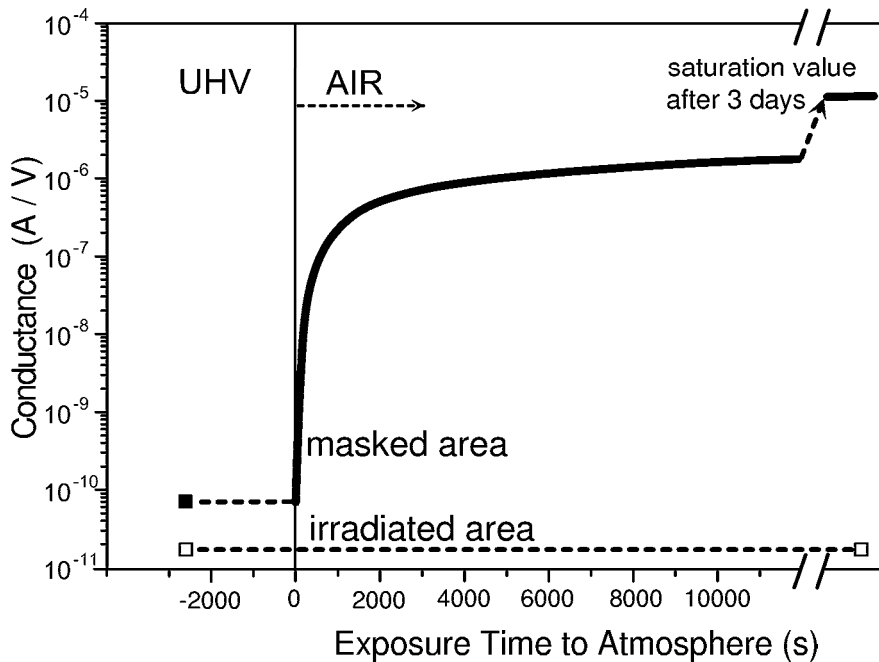


Figure 6.4: Surface conductance of the hydrogenated (masked) and the hydrogen-free (irradiated) part of a homoepitaxial diamond (100) layer in UHV and during exposure to air.

In order to elucidate the role of hydrogen the following experiments were performed. In the first measurement the undoped homoepitaxial (100) diamond layer grown on a type Ib (100) substrate (emphasized in Fig. 6.2) was introduced in the state of high conductance into UHV. The high conductance was confirmed in situ with  $10^{-4}$  A/V and the hydrogenation was established by the fingerprint of negative electron affinity (NEA) of the surface as seen in the total photoelectron yield<sup>1</sup> spectrum [99, 130]. After annealing the sample in UHV at  $410 \pm 20^\circ\text{C}$  for 15 minutes the conductance dropped to  $10^{-10}$  A/V while the hydrogenation remained intact as demonstrated by the NEA property of the surface.

In fact, thermal desorption of chemisorbed hydrogen does not commence below  $700^\circ\text{C}$  [85, 131]. As in the case of the aluminium experiment of the preceding chapter, half of the sample was masked by a tantalum foil and hydrogen from the other half got removed by electron beam (1 keV,  $0.2 \text{ mA/cm}^2$ , 90 min) induced desorption without introducing electrically active defects [88] in addition.

The corresponding yield spectra are shown in Fig. 6.3. The masked area still showed the fingerprint of NEA, namely a steeply rising electron yield at the band gap energy. This feature was absent on the irradiated surface proving that

<sup>1</sup>see also Appendix A

the hydrogen termination has been removed and the electron affinity turned positive. As demonstrated in Fig. 6.4 both halves of the sample were in the low conductance state and remained so as long as they are kept in UHV. Already at this stage, it is obvious that hydrogen termination is **not** equivalent to the highly conducting state of the diamond surface.

However, when the sample was brought up to air the conductance of the masked and thus hydrogenated area rose by four orders of magnitude within the first twenty minutes of exposure and increased more slowly thereafter until it has been reaching the initial value of  $10^{-5}$  A/V after 3 days. By contrast, the dehydrogenated part of the sample remained in its low conductance state with no sign of change whatsoever.

This experiment clearly demonstrates that the hydrogenation of diamond is a necessary but not a sufficient condition for high surface conductivity. An additional ingredient that is obviously coming from the air and that thermally desorbs in UHV above  $400^{\circ}\text{C}$  is necessary.

These findings appear to contradict experiments which show that the surface conductivity is irretrievably lost if a sample is annealed above  $\sim 200^{\circ}\text{C}$  in air [132]. According to the results obtained in UHV, one would expect that the conductivity returns upon cooling because the hydrogen termination is expected to be stable up to much higher temperatures. Therefore, the thermal stability of the RT surface conductivity of a plasma hydrogenated IIa C(100) single crystal *in air* was investigated while simultaneously monitoring the hydrogen coverage by multiple internal reflection infrared spectroscopy (MIRIRS). MIRIRS provides monolayer sensitivity for the C-H stretching vibrations around  $2800\text{ cm}^{-1}$  [53]. The RT conductance of the sample as a function of annealing temperature is plotted in Fig. 6.5a). Up to  $200^{\circ}\text{C}$  annealing temperature the conductance remained in the  $10^{-6} - 10^{-5}$  A/V range but dropped below  $10^{-10}$  A/V after annealing at  $230^{\circ}\text{C}$ . The IR signature of the hydrocarbon bonds at the surface is displayed for three selected cases in Fig. 6.5b). The first spectrum obtained immediately after plasma hydrogenation shows the characteristic stretching mode of the diamond (100) 2x1:H surface at  $2896\text{ cm}^{-1}$  [133] and in addition the symmetric ( $2851\text{ cm}^{-1}$ ) and the antisymmetric ( $2920\text{ cm}^{-1}$ ) stretching mode of  $\text{CH}_2$  groups of physisorbed n-alkanes [134]. The spectrum obtained after annealing at  $190^{\circ}\text{C}$  shows only the monohydride mode characteristic for the surface hydrogen termination but no more hydrocarbon adsorbates. At that stage the conductance of the sample was still in the  $10^{-6}$  A/V range. Hydrocarbon adsorbates are thus not responsible for the high surface conductivity. Finally, after the  $230^{\circ}\text{C}$  annealing step hydrogen was obviously desorbed from the surface because C-H stretching modes are no longer observed (Fig. 6.5 b). At this stage the conductance of the sample has dropped to  $2 \times 10^{-11}$  A/V. These measurements show that hydrogen desorbs in air at much lower temperatures than in UHV. They also confirm that hydrogen



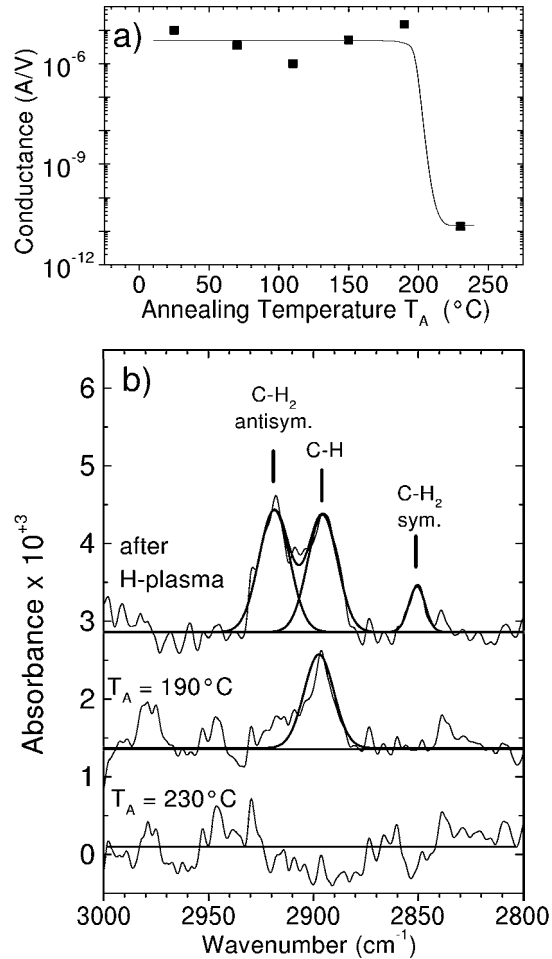


Figure 6.5: a) Surface conductance of a plasma hydrogenated (100) diamond single crystal as a function of annealing temperature in air. b) Infrared spectra in the region of the C-H-stretching modes after the hydrogen plasma treatment and after 190°C and 230°C annealing temperature, respectively. The spectra are offset for clarity.

termination is necessary for the high surface conductivity in diamond.

### 6.3 An electrochemical model for the surface conductivity

From these results it appears that an adsorbate from the atmosphere on the hydrogen terminated diamond surface is necessary to induce the surface accumulation layer of  $10^{13} \text{ cm}^{-2}$  holes. As emphasized by Ristein *et al.* [128], this requires an acceptor level of the adsorbate at the VBM of diamond within  $kT$ . With an electron affinity  $\chi_{C:H} = -1.3 \text{ eV}$  for hydrogenated diamond

(111) [93] and (100) (see Chapter 4) this requirement sets a lower limit for the electron affinity  $\chi_{ad}$  of the adsorbate:  $\chi_{ad} = E_g - 1.3 \text{ eV} = 4.2 \text{ eV}$  where  $E_g = 5.5 \text{ eV}$  is the band gap energy of diamond. Electron affinities of molecular atmospheric species lie below 2.5 eV and even for halogen atoms  $\chi_{ad}$  does not exceed 3.7 eV [135]. Thus, direct electron transfer from the diamond into an atmospheric adsorbate appears to be impossible.

However, a thin water layer as it forms naturally on all surfaces which are exposed to atmosphere provides an electron system which can act as a surface acceptor for diamond. Before going into detail, the main idea is very simple. The neutral species from the air are not able to act as an electron acceptor as long as there are no empty states available in the energy range of the VBM of diamond. If, by any ionization process, neutral adsorbates from the air become positively charged new acceptor states in the required energy range provide an electron transfer from diamond to the ionic species. The ionization process does not take place for free adsorbates; however, for species dissolved in water the presence of ions is a typical situation, and therefore, protons which are screened by water molecules ( $H_3O^+$ ) are good candidates to act as acceptors. The rather complex situation we are dealing with is that of a thin water overlayer (or just isolated water clusters) adsorbed at the diamond surface. Though these conditions are quite different to a situation of diamond in contact with an electrolyte of macroscopic dimensions, the latter one is used as a first approximation to describe the fundamental processes involved.

We assume that the electron exchange from diamond to the water layer is governed by the reduction of protons to molecular hydrogen  $2H_3O^+ + 2e^- \rightleftharpoons H_2 + 2H_2O$  [136] where the electrons stem from the diamond valence band. The reaction is driven by the difference in the chemical potential of the liquid phase ( $\mu_e$ ) and that of diamond (Fermi level  $E_F$ ). As long as  $\mu_e$  is below  $E_F$ , electrons are being transferred from diamond to the water layer and thereby reduce  $H_3O^+$  to  $H_2$  and  $H_2O$ . The residual holes in the diamond accumulation layer, and thus the associated surface space charge, lower  $E_F$  with respect to  $\mu_e$  due to the electrostatic potential. In equilibrium  $\mu_e$  and  $E_F$  are equal at the interface as shown schematically in Fig. 6.6. The equilibrium value of  $\mu_e$  relative to the vacuum level as the common reference for the aqueous layer and the solid [137] depends according to Nernst's equation on the concentrations of  $[H_3O^+]$  and  $[H_2]$  as

$$\mu_e = \mu_0 - kT/2 \cdot \ln \left[ \frac{([H_3O^+]/[H_3O^+]_{SHE})^2}{([H_2]/[H_2]_{SHE})} \right] \quad (6.1)$$

Here,  $\mu_0 = -4.44 \text{ eV}$  is the chemical potential for electrons under standard hydrogen electrode (SHE) conditions.  $[H_3O^+]_{SHE}$  and  $[H_2]_{SHE}$  are the oxonium and the hydrogen concentrations of the SHE, respectively. Replacing  $[H_2]$  by the  $H_2$  partial pressure  $p_{H_2}$  and  $[H_3O^+]$  by the pH value of the aqueous layer

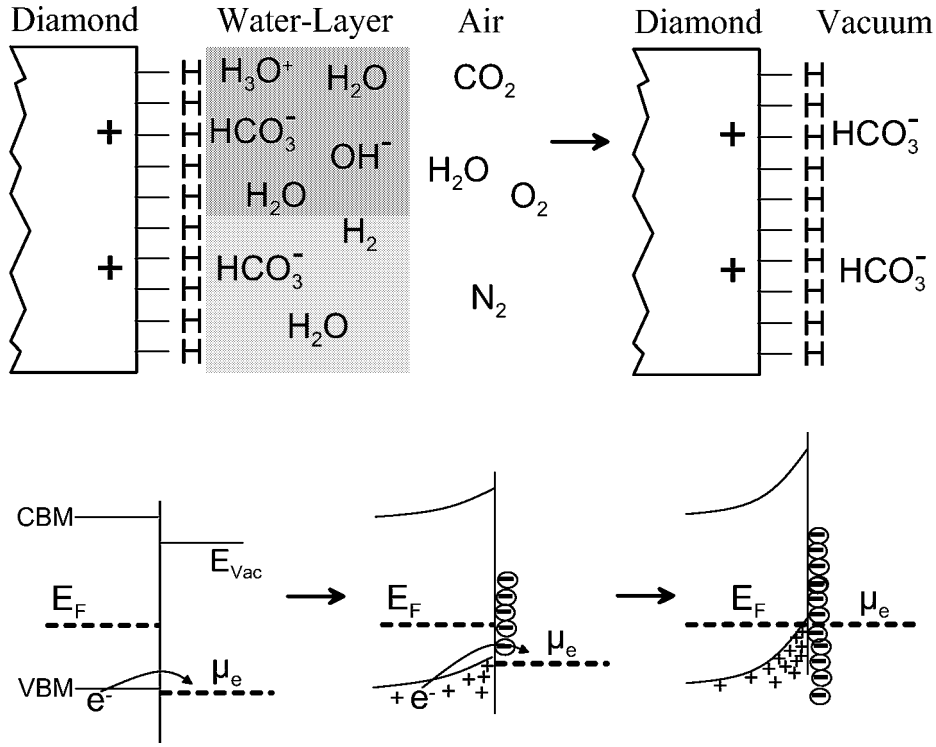


Figure 6.6: Top: Schematic picture of the hydrogenated diamond surface in contact with a water layer as it forms in air (left side) and after introducing the sample into vacuum (right side). Bottom: Evolution of band bending during the electron transfer process at the interface between diamond and the water layer.

yields at RT for Eq. (6.1):

$$\mu_e = -4.44 \text{ eV} + \frac{\ln 10 \cdot kT}{2} \cdot \left[ 2pH + \log \left( \frac{p_{H_2}}{\text{bar}} \right) \right]. \quad (6.2)$$

This relationship is plotted in the insert of Fig. 6.7. Due to the  $\text{CO}_2$  content in air, standard atmospheric conditions lead to a pH value of water around 6 [138]. With a dissolved hydrogen concentration at the interface in the ppm range which would correspond to a partial pressure of  $p_{H_2} \approx 10^{-3}$  mbar the chemical potential  $\mu_e$  of an aqueous wetting layer is  $\mu_0 + 0.18 \text{ eV} = -4.26 \text{ eV}$ . Taking the electron affinity of  $-1.3 \text{ eV}$  for hydrogenated (111) and (100) diamond the pinning position of  $E_F$  at the water/diamond interface lies about 50 meV below VBM (insert of Fig. 6.7). The hole charge is compensated by those anions ( $\text{HCO}_3^-$ ) that are left uncompensated by the reduction of the oxonium ions.

Once surface conductivity has been established the sample can even be put into vacuum and the wetting layer be removed which is depicted in the right part of Fig. 6.6. As long as the anions remain at the surface the hole

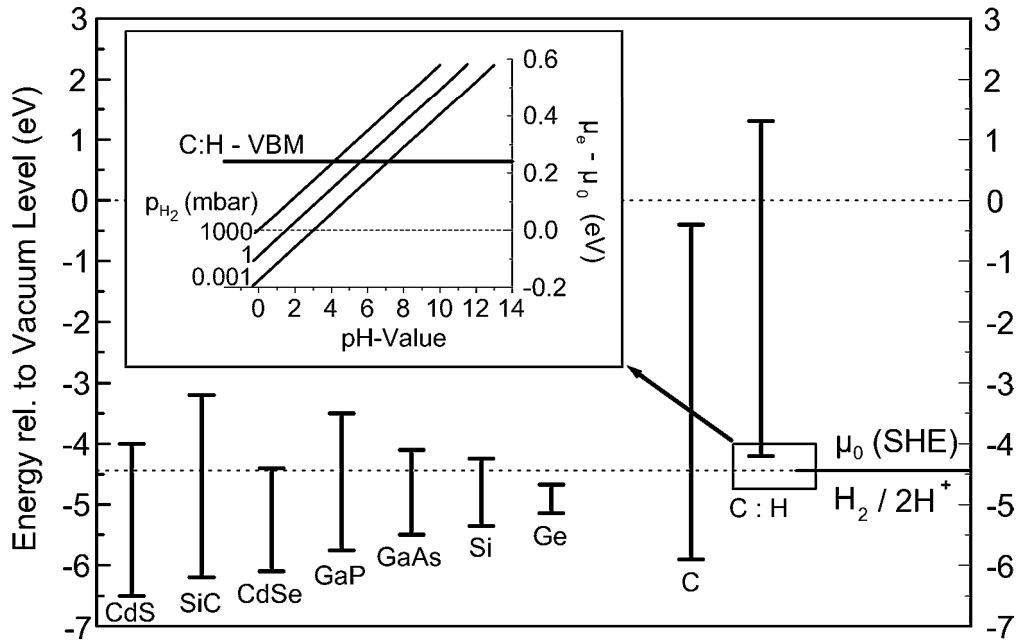


Figure 6.7: Energies of the band edges of several semiconductors and of hydrogenated and hydrogen-free diamond relative to the vacuum level. The chemical potential  $\mu_0$  for electrons under standard hydrogen electrode (SHE) conditions of  $-4.44$  eV is also given. The insert shows the change of the chemical potential  $\mu_e$  relative to  $\mu_0$  as a function of pH-value and of hydrogen concentration expressed as partial pressure. Conditions for atmospheric wetting layers are around  $\text{pH}=6$  and  $p_{\text{H}_2} = 0.001$  mbar.

accumulation will also be preserved. Thermal desorption of the anions which takes place at much lower temperatures ( $\approx 300^\circ\text{C}$ ) than those necessary for surface dehydrogenation in UHV ( $\approx 700^\circ\text{C}$ ) removes the accumulation layer and leaves a hydrogenated but highly resistive surface. On the basis of Eq. 6.2 as plotted in the insert of Fig. 6.7 we readily understand qualitatively why the surface conductivity of hydrogenated diamond increases when the electrolyte becomes more and more acidic as demonstrated by Ri *et al.* [127] and Denisenko *et al.* [29]. Finally, the electrochemical model presented here explains why hydrogenated diamond is the only semiconductor that exhibits this kind of surface conductivity. According to Fig. 6.7 the VBM of all semiconductors lies more than  $0.7$  eV below the  $\mu_0$  [139]. Standard atmospheric conditions will therefore never produce hole accumulation within those materials. The same is true for non hydrogenated diamond surfaces. Only via the strong reduction of the electron affinity by hydrogen termination does the VBM of diamond shift up above the chemical potential of typical surface wetting layers.

## 6.4 Some critical assessments of the electrochemical model

However, a few critical points must be added to the model which are still under investigation. As mentioned earlier, the surface Fermi level is required to be situated near the VBM for highly conductive surface layers. However, some experiments in PES reveal that the surface conductivity is even detected for diamonds with a surface Fermi level that lies several tenths of eV above VBM. It is thus tempting to speculate that this discrepancy is due to the VBM determination by PES which only provides values by averaging over a large area, whereas a high surface conductivity is already measured when few highly conductive current paths are available. If those regions exhibiting  $E_F - E_{VBM} \leq kT$  are small enough, the average VBM position measured by PES is still dominated by the majority of the non-conductive regions, though the transport measurements reveal high surface conductivity. Lateral resolved conductivity measurements on type IIa single crystals indeed show an inhomogenous distribution of highly conductive regions on the surface [140].

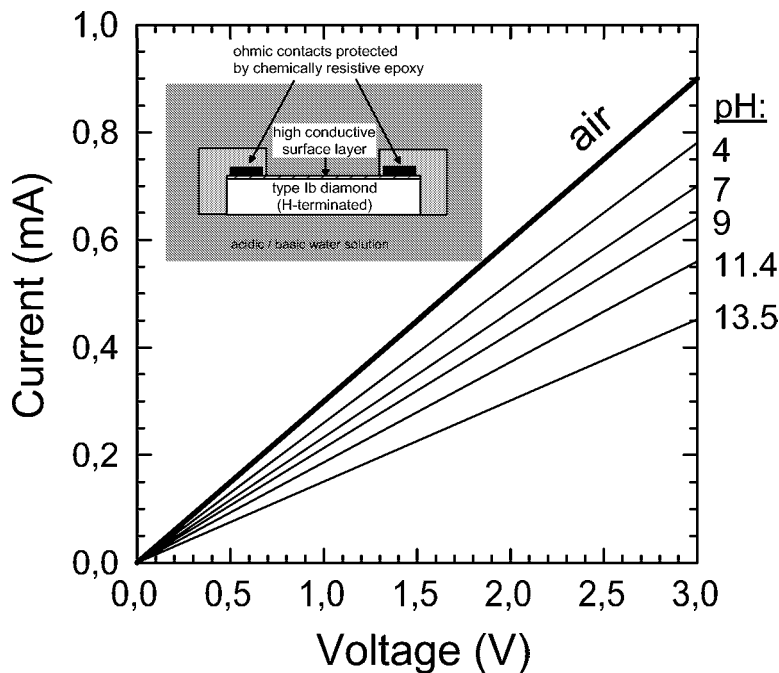


Figure 6.8: I-V characteristics of a pH-sensitive diamond sensor designed by Denisenko *et al.* (the setup is sketched in the insert) in air and in an electrolyte at different pH-values (data are redrawn from Ref. [29]).

The second remark focusses on the quantitative dependence of the surface conductivity on the pH-value and the  $H_2$  partial pressure as described by Eq. 6.2. It is derived under the assumption that only holes in diamond and

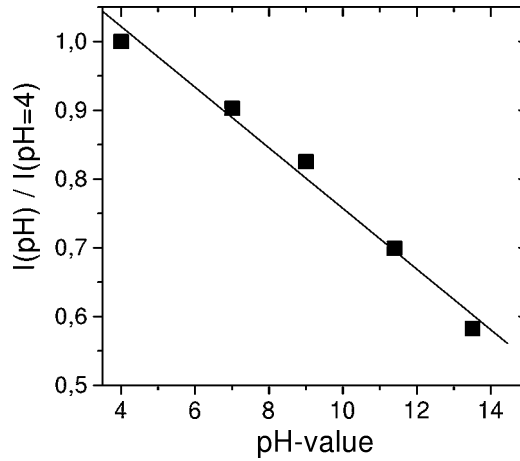


Figure 6.9: Relative change of the current  $I$  at 3 V of Fig. 6.8 with pH-value.

the remaining anions at the surface dominate the equilibrium conditions. The water molecules just act as a “catalyst” for the production of hydronium ions. Furthermore, exchange reactions with the atmosphere of the electrolyte species involved, concentration profiles within the aqueous layer, and the influence of water clusters instead of an extended electrolyte are neglected. Recently, I-V measurements of the surface conductivity depending on the pH-value of an electrolyte have been published by Denisenko and co-workers [29]. Their results are shown in Fig. 6.8; the corresponding setup is depicted in the insert. As expected on the basis of our model, the surface conductance increases with decreasing pH-value because the latter lowers the electrochemical potential  $\mu_e$  relative to VBM and thus increases the hole accumulation density. However, the highest conductance was obtained when the sensor was placed in air. Whether these findings are due to the difference between water clusters and thick water films is not known yet.

The depth-integrated hole density in the accumulation layer, i.e. the surface charge density  $\sigma_{accu}$ , depends on the energy separation of  $E_F$  and  $E_{VBM}$  at the surface [128] as follows

$$\sigma_{accu} \propto \exp((E_{VBM} - E_F)_{surface}/(2kT)). \quad (6.3)$$

In our model, the surface Fermi level  $E_F$  equals  $\mu_e$ . Then,  $\sigma_{accu}$  is simply expressed by inserting Eq. 6.2 in Eq. 6.3 such as

$$\sigma_{accu} \propto \exp(E_{VBM}/(2kT)) \cdot \exp(-pH \cdot \ln(10)/2). \quad (6.4)$$

The surface current density is the product of the carrier mobility times  $\sigma_{accu}$ , and therefore, the conductances measured by Denisenko *et al.* should also

show an exponential dependence of the pH-value. However, the apparent linear relationship between the surface conductivity and the pH-value as shown in Fig. 6.9 seems to contradict the quantitative predictions of our model.

The final remark concerns the relationship between the surface conductivity in the framework of our electrochemical model and the MESFET devices based on the surface conductivity of diamond. By the appropriate choice of the gate contact material [11] either enhancement mode (the active channel is pinched off at zero gate bias and becomes populated applying negative gate bias) or depletion mode (active channel is depleted by applying positive gate voltage) field effect transistor characteristics are possible. In the case of the MESFET with Al gate (enhancement mode) the situation is sketched in Fig. 6.10. When

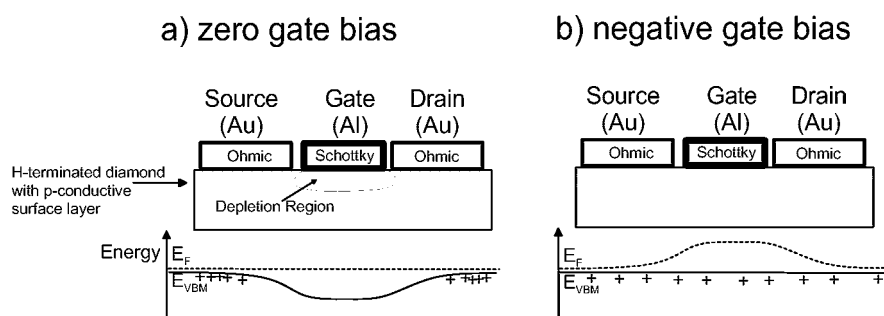


Figure 6.10: Sketch of a MESFET (top) based on the surface conductivity of hydrogenated diamond in the case of an Al gate (enhancement mode) and the corresponding band diagrams (bottom). (a) At zero gate bias the surface channel is depleted of holes (+) and the transistor is pinched off. (b) At negative gate bias, the energy barrier for holes is removed and the current easily flows from the source to the drain electrode.

the gate is negatively biased (Fig. 6.10b), this situation corresponds to a Schottky diode formed by diamond and the aluminium gate that is driven in forward direction. Since our electrochemical model predicts the conductive layer in the vicinity of the diamond surface as it is shown in Fig. 6.6, one would thus expect a substantial tunneling current flow between gate and drain which is, however, not observed for real devices [90]. As it is discussed by Denisenko *et al.*, [24] the observed gate leakage current is at least one order of magnitude too small than expected for a surface conduction layer. Therefore, the authors conclude that the gate contact has to be considered as a metal-insulator-semiconductor (MIS) structure rather than a metal-semiconductor Schottky contact [24, 90] corresponding to band scheme as it is depicted in Fig. 6.1c).

Apparently, the complex situation of diamond for real field effect transistor devices has been oversimplified by our electrochemical model and further improvements are thus required.

## 6.5 Summary

In the last chapter, the fairly high surface conductivity of hydrogen terminated diamond was investigated. This feature of hydrogenated diamond surfaces which is unique among all semiconductors was ascribed to electron transfer reactions that occur at the interface formed between diamond and a mildly acidic water layer. An electrochemical model was deduced from photoemission spectroscopy data and transport measurements which provide evidence that hydrogen is a necessary requirement for the observed surface conductivity but not sufficient; only in combination with exposure to air is surface conductivity observed. In this model dissolved oxonium ions act as electron acceptors by their reduction to molecular hydrogen and water. The observed surface hole density of about  $10^{13}\text{cm}^{-2}$  requires a chemical potential  $\mu_e$  of the water layer that is located at the surface VBM position of diamond. Due to the negative electron affinity of -1.3 eV only hydrogenated diamond surfaces are able to fulfill this condition. Small variations in  $\mu_e$  with respect to VBM and thus variations in conductivity with the pH value of the wetting layer and the  $H_2$  partial pressure are quantitatively accounted for applying Nernst's equation.



# Summary

On account of the considerable progress in chemical vapour deposition techniques of diamond synthesis [1] the application of diamond for electronic devices has stimulated the interest in related surface and interface properties. The object of this thesis is to investigate electronic and structural properties of diamond surfaces and interfaces that play an important role for a special type of field effect transistor. These metal-semiconductor field effect transistor (MESFET) devices are based on a unique property of hydrogenated diamond surfaces, namely an unusual high p-type surface conductivity. The successfully realized devices [25, 26] show promising properties for high power (estimated maximum power density: 10W/mm [90]) and high frequency applications (cut-off frequencies: 2.2 GHz [28]), respectively. In this thesis, we present a novel explanation for the conductivity mechanism and address related questions concerning the electronic properties of diamond surfaces and interfaces.

The diamond surface itself was the starting point of this thesis. Previous investigations on diamond (100) and (111) [54, 55] have been extended to the third of the low-index surfaces, namely diamond (110). It turns out that this particular surface is of inferior quality to the (111) and the (100) surface. Mechanically polished samples always exhibit macroscopic polishing grooves along [001] which are due to the high anisotropy of hardness that is typical for this surface orientation [83]. After hydrogen plasma polishing, the low-energy electron diffraction (LEED) pattern exhibits pronounced streaking in this direction, i.e. the direction perpendicular to the atomic zig-zag chains which are the characteristic structural element of the C(110) surface. Also, angle-resolved valence band spectroscopy (ARUPS) data show no dispersion of valence band states along [001], pointing towards a substantial loss in translation symmetry along this crystallographic direction. Furthermore, the investigation of the local surface configuration by means of core-level photoemission spectroscopy (XPS) does not permit to distinguish clearly between a surface superficially covered by adsorbed hydrocarbons and a surface only terminated by hydrogen after annealing in UHV, as is the case for C(111) and C(100).

Despite these limitations a number of structural and electronic information has

been deduced from LEED and ARUPS data.

- (i) The (110) surface is not reconstructed, neither in its hydrogenated nor in its hydrogen free form.
- (ii) The hydrogenated and the bare (110) surface exhibit zig-zag chains of C-atoms running along the  $[1\bar{1}0]$  that are clearly not dimerized as proven by symmetry related extinctions of definite LEED reflexes. There is, however, compelling evidence that the C-C bond length in the surface chains are substantially different from its bulk value. This is consistent with *ab initio* calculations which predict a reduced in-plane bond length.
- (iii) The streaking of LEED spots in  $[001]$  direction is due to a high density of monoatomic steps running along  $[1\bar{1}0]$ .
- (iv) By means of ARUPS, a weakly dispersing surface state S has been unambiguously detected between  $\bar{\Gamma}$  and  $\bar{J}$  in the surface Brillouin zone of the dehydrogenated (110) surface, i.e. the direction along the chains. Comparing the dispersion relation of S with *ab initio* calculations [64] the band width of S is considerably smaller than expected from theory. This surface state remains entirely below the valence band maximum (VBM).
- (v) As in the case of diamond (111) the metallic nature of the (110) surface, as predicted by theory, is not confirmed experimentally.
- (vi) In the perpendicular direction, however, an appreciable increase in density of occupied states has been detected by ARUPS after dehydrogenation. This is consistent with the high step density observed by LEED reflecting the disordered state of the surface. From that point of view, the fairly large band bending of more than 1 eV during hydrogen desorption may be ascribed to the high number of defect states.

One of the outstanding properties of hydrogenated diamond surfaces is the negative electron affinity  $\chi$ . In contrast to C(111)-(1x1):H with  $\chi = -1.3$  eV [93] absolute values for the technologically more important C(100)-(2x1):H surface were missing. By studying the diamond (100) surface with photoemission and work function measurements values of the electron affinity of the clean C(100)-(2x1) (+0.5 eV) and the hydrogenated C(100)-(2x1):H (-1.3 eV) surface are obtained with an accuracy of  $\pm 0.1$  eV. An analysis of the electron affinity in the framework of adsorbate induced dipole layers shows good agreement with experimental findings when depolarization effects are taken into account. From the change of  $\chi$  during thermal annealing vertical dipole moments of the C-H ( $0.08 \pm 0.01$  eÅ) and the C-O ( $-0.10 \pm 0.01$  eÅ) bonds are derived. For the plasma hydrogenated surface it is shown that physisorbates (most probably hydrocarbons) increase the electron affinity by a few tenths of an electron volt compared to the contamination-free, hydrogenated surface. The measured electron affinity of the chemically oxidized C(100) of +1.7 eV represents a lower limit for a purely oxidized (100)-(1x1):O diamond surface

because residual hydrogen provided by the acid treatment could not be avoided. From the magnitude of the C-O dipole the bridge-site bonding configuration of oxygen on the C(100) surface is unambiguously deduced.

In addition, the influence of adsorbed hydrogen and oxygen on the electron emission properties of diamond (100) are investigated by total photoelectron yield spectroscopy. It is shown that electrons excited with sub-band gap light mainly originate from graphitic patches that develop during thermal annealing.

In the context of electronic devices, the interface between a semiconductor and a metal is of decisive importance. The MESFETs mentioned at the beginning are realized by the evaporation of gold (as ohmic source and drain contacts) and of aluminium (as gate electrode exhibiting Schottky characteristics) on hydrogenated diamond surfaces [90]. In this context, the role of hydrogen at the interface between diamond and gold, magnesium, and aluminium and its effect on Schottky barrier heights are investigated.

Summarizing the main result for gold on hydrogenated diamond (111) surfaces, it is shown that all experiments clearly point towards the preservation of hydrogen at the gold-diamond interface under the conditions of our investigation. Gold evaporation at room temperature leads to layer-by-layer growth. The measured value of 0.3 eV for the Schottky barrier height (SBH) of gold on C(111)-(1x1):H does not constitute an energy barrier for hole transport from diamond to the metal, which is in agreement with transport measurements [117]. Annealing at moderate temperatures (500°C) transforms the Au layer into islands, re-exposing the hydrogenated diamond surface in between. The islands themselves are highly mobile and do suffer from good adhesion to the substrate. Nevertheless, they are highly inert against the attack of *aqua regia* in contrast to isolated gold.

As in the case of gold, there is no indication that the interface C-H dipole layer is attenuated by magnesium on C(100)-(2x1):H. Whether this fact is related to the presence of magnesium oxide as witnessed by the Mg 2p core levels has not been unambiguously resolved yet. Furthermore, the formation of three-dimensional islands is apparently favored, which points towards a low interface tension between C(100)-(2x1):H and magnesium. Taking the lateral inhomogeneous distribution of magnesium into account, a Schottky barrier height of  $0.85 \pm 0.15$  eV is deduced for a magnesium film of nominally 25Å thickness which matches the data from the literature [119, 120].

In order to study the influence of hydrogen termination on the formation of the aluminium-diamond Schottky barrier, aluminium was evaporated on a diamond (111) surface that was structured by electron bombardment and thus partly hydrogenated while half of it was hydrogen-free. An island formation is likely to occur for aluminium on diamond for the hydrogenated surface in particular. As it is the case for gold and magnesium no chemical interaction of aluminium with carbon is detected by core level spectroscopy. In addition, no

influence of aluminium on the interface hydrogen is observed in electron yield microscopy. The small shift of the spectra reveal minor charge transfer, both for the hydrogenated and the dehydrogenated surface. The measured value of the SBH of 0.7 eV is smaller than obtained by other groups [126].

In the last chapter the fairly high surface conductivity of hydrogen terminated diamond is investigated. This feature of hydrogenated diamond surfaces which is unique among all semiconductors is ascribed to electron transfer reactions that occur at the interface formed between diamond and a mildly acidic water layer. An electrochemical model is deduced from photoemission spectroscopy data and transport measurements which provide evidence that hydrogen is a necessary requirement for the observed surface conductivity but not sufficient; only in combination with exposure to air is surface conductivity observed. In this model dissolved oxonium ions act as electron acceptors by their reduction to molecular hydrogen and water. The observed surface hole density of about  $10^{13}\text{cm}^{-2}$  requires a chemical potential  $\mu_e$  of the water layer that is located at the surface VBM position of diamond. Due to the negative electron affinity of -1.3 eV only hydrogenated diamond surfaces are able to fulfill this condition. Small variations in  $\mu_e$  with respect to VBM and thus variations in conductivity with the pH value of the wetting layer and the  $H_2$  partial pressure are quantitatively accounted for via Nernst's equation. However, this model still needs further modifications to account quantitatively for pH-sensitive experiments [29].

Diamond interfaces - for sure a never ending story! Working in this field I could not help to notice that this simplest of all semiconductors with its four valence electrons and two core electrons again and again reveals surprising properties. And, moreover, most of them are mainly related to hydrogen which is really the simplest of all elements.

# Zusammenfassung

Die beachtlichen Fortschritte auf dem Gebiet der Diamantabscheidung aus der Gasphase (chemical vapor deposition) [1] und den damit verbundenen Einsatzmöglichkeiten von Diamant für elektronische Bauelemente haben das Interesse an Oberflächen- und Grenzflächeneigenschaften von Diamant beflügelt. Ein Schwerpunkt dieser Arbeit war deshalb die Untersuchung elektronischer und struktureller Eigenschaften, die in Zusammenhang mit einem bestimmten Typ von Metall-Halbleiter Feldeffekt-Transistor (MESFET) stehen. Diese MESFETs beruhen auf einer einzigartigen Eigenschaft von Diamant. Obwohl undotierter Diamant bei Raumtemperatur ein elektrischer Isolator ist, zeigen die mit Wasserstoff abgesättigten Oberflächen eine ungewöhnlich hohe, p-artige Leitfähigkeit [12, 13]. Die angesprochenen MESFETs [25, 26] sind äußerst vielversprechend für Hochleistungs- und Hochfrequenzanwendungen. So wurden bereits Leistungsdichten von  $6\text{W/mm}$  mit  $1\mu\text{m}$  Gate-Länge bei Durchbruchfeldstärken bis  $2 \cdot 10^6\text{V/cm}$  [90] und Grenzfrequenzen bis  $2.2\text{GHz}$  [28] gemessen. Im Rahmen dieser Doktorarbeit wurde ein neues Modell vorgestellt, das den grundsätzlichen Leitfähigkeitsmechanismus erklärt und damit verbundene Eigenschaften von Diamantoberflächen bzw. -grenzflächen untersucht.

Der Ausgangspunkt dieser Arbeit war die Diamantoberfläche selbst, also die Grenzschicht Diamant-Vakuum. Dabei wurden die vorangegangenen Untersuchungen von Diamant (100) und (111) [54, 55] auf die (110) Oberfläche ausgedehnt, zu der bis zu diesem Zeitpunkt noch vergleichsweise wenig bekannt war. Charakteristisch für diese Oberfläche sind planare Kohlenstoff-Zick-Zack-Ketten, welche senkrecht zu der [001]-Richtung des Kristalls verlaufen. Es stellte sich im Laufe der Arbeit heraus, dass die kristalline Ordnung der (110) Oberfläche im Vergleich zur (111) und (100) Oberfläche deutlich reduziert ist. Nach der "Politur" in einem Mikrowellen-Wasserstoffplasma zeigten sich mittels Beugung langsamer Elektronen (LEED) stark elongierte Reflexprofile in [001]-Richtung. Zusätzlich konnte in der winkelaufgelösten UV-induzierten Photoelektronenspektroskopie (ARUPS) keine Dispersion von besetzten Zuständen in dieser Richtung nachgewiesen werden. Beides deutet auf einen erheblichen Verlust der Translationssymmetrie an der Oberfläche entlang der [001]-Richtung

hin, d.h. senkrecht zu den Zick-Zack-Ketten. Ebenso ist die Nahordnung der (110) Oberfläche weniger ausgeprägt als im Falle der beiden anderen niederindizierten Oberflächen von Diamant. So war es nicht möglich - im Gegensatz zu (111)- und (100)-Oberflächen - mittels röntgeninduzierter Photoelektronenspektroskopie (XPS) klar zwischen einer ausschließlich mit Wasserstoff terminierten Oberfläche und einer zusätzlich mit Kohlenwasserstoffen kontaminierten Oberfläche zu unterscheiden.

Trotz dieser Einschränkungen konnten eine ganze Reihe von strukturellen und elektronischen Fragestellungen mittels LEED und ARUPS geklärt werden.

(i) Weder die reine, noch die mit Wasserstoff passivierte (110) Oberfläche zeigt eine Rekonstruktion.

(ii) Eine Dimerisierung innerhalb der Zick-Zack-Ketten der Oberfläche ist sowohl für die saubere als auch für die hydrierte Oberfläche anhand symmetriebedingter Reflex-Auslöschungen im LEED auszuschließen. In Übereinstimmung mit *ab initio* Rechnungen [64] gibt es zusätzlich deutliche Hinweise auf eine Verringerung der C-C Bindungslänge innerhalb der Ketten der Oberfläche.

(iii) Anhand der Energieabhängigkeit der LEED-Reflex-Profile in [001] Richtung, konnte eine hohe Dichte von monoatomaren Stufen entlang der  $[1\bar{1}0]$  abgeleitet werden.

(iv) Entlang der Zick-Zack-Ketten ( $[1\bar{1}0]$ ) der dehydrierten (110) Oberfläche wurde mittels ARUPS ein dispergierender Zustand  $S$  zwischen  $\bar{\Gamma}$  und  $\bar{J}$  der Oberflächen-Brioullinzone eindeutig als Oberflächenzustand identifiziert. Im Vergleich zu *ab initio* Rechnungen [64] weist das von  $S$  gebildete Oberflächenband eine deutlich geringere energetische Breite auf; außerdem liegt  $S$  vollständig unterhalb des Valenzbandmaximums (VBM) und kreuzt nicht, wie vorhergesagt, das Fermi-Niveau entlang der  $[1\bar{1}0]$  Richtung.

(iv) Damit zeigt die reine (110) Oberfläche, wie übrigens auch die saubere (111) Oberfläche, spektroskopisch keine metallischen Eigenschaften entgegen theoretischer Vorhersagen [64, 80].

(v) In der senkrecht zu den Ketten verlaufenden Richtung ( $[001]$ ) war in den ARUPS Daten nach dem Abheizen des Wasserstoffs eine erhebliche Zunahme der Zustandsdichte am VBM zu erkennen, und damit ein weiterer Hinweis auf die Unordnung der Oberfläche in dieser Richtung. Die mit XPS und ARUPS gemessene Bandverbiegung während des thermischen Anlassens von mehr als 1 eV wird deshalb auf die starke Zunahme von (zuvor mit Wasserstoff passivierten) Defektzuständen an der Oberfläche zurückgeführt.

Eine herausragende Eigenschaft von hydrierten Diamantoberflächen ist die negative Elektronenaffinität  $\chi$ . Mit anderen Worten, die Leitungsband-Kante von mit Wasserstoff terminierten Diamantoberflächen liegt energetisch oberhalb des Vakuumniveaus. Während für die hydrierte, unrekonstruierte (111) Oberfläche (C(111)-(1x1):H)  $\chi$  bereits früher bestimmt wurde ( $\chi = -1.3$  eV [93]), lagen für die hydrierte, 2x1-rekonstruierte (100) Oberfläche (C(100)-

(2x1):H) noch keine absoluten Werte zu  $\chi$  vor.

(i) Mittels kombinierter Photoemissions- und Austrittsarbeitsmessungen konnten für die technologisch interessantere (100) Fläche sowohl im hydrierten Zustand (C(100)-(2x1):H;  $\chi = -1.3$  eV) als auch für die reine Oberfläche (C(100)-(2x1);  $\chi = +0.5$  eV), die nasschemisch oxidierte Oberfläche ( $\chi = +1.7$  eV) und die ideal Sauerstoff-terminierte Oberfläche (C(100)-(1x1):O;  $\chi = +2.2$  eV) Elektronenaffinitäten mit einer Genauigkeit von  $\pm 0.1$  eV bestimmt werden.

(ii) Der Zusammenhang zwischen Elektronenaffinität und Adsorbatbedeckung wurde im Rahmen eines elektrostatischen Dipolmodells erfasst. Unter Berücksichtigung von Depolarisationseffekten zeigen die experimentellen Werte und die Theorie sehr gute Übereinstimmung.

(iii) Aus der Änderung der Elektronenaffinität während des thermischen Anlassens konnten Werte für die senkrechten Dipolmomente der C-H-Bindung ( $0.08 \pm 0.01$  eÅ) und der C-O-Bindung ( $-0.10 \pm 0.01$  eÅ) abgeleitet werden. Aus dem senkrechten C-O-Dipolmoment ergibt sich eindeutig, dass der Sauerstoff bevorzugt auf (100) Brückenplätzen adsorbiert ist.

(iv) Ferner erwiesen sich Physisorbate (höchstwahrscheinlich Kohlenwasserstoffe) in der Lage,  $\chi$  im Vergleich zur mit Wasserstoff abgesättigten, kontaminationsfreien (100)-Oberfläche um 0.3 bis 0.6 eV zu erhöhen.

(v) Zusätzlich wurde der Einfluss von Wasserstoff und Sauerstoff auf die Elektronenemission von C(100) mittels Photoelektronenausbeutespektroskopie untersucht und dabei gezeigt, dass Elektronen, die mit Licht einer Energie unterhalb der Bandlücke von Diamant (5.5 eV) angeregt wurden, aus graphitischen Bereichen an der Oberfläche stammen. Diese Bereiche konnten sowohl durch Hydrierung im Mikrowellenplasma als auch durch nasschemische Oxidation der Oberfläche deutlich reduziert werden und bildeten sich größtenteils erst beim Heizen der Oberfläche.

Die Grenzschicht zwischen Halbleiter und Metallen spielt bei elektronischen Bauelementen im allgemeinen und bei den auf Diamant basierenden MESFETs im besonderen eine fundamentale Rolle. Gold dient als ohmscher Kontakte für Source und Drain und Aluminium als Schottky-Kontakt für die Gate-Elektrode [90]. In dieser Arbeit wurde der Einfluss des Wasserstoffs an der Grenzschicht zwischen Diamant und Gold, Aluminium und Magnesium auf die strukturellen Eigenschaften (z.B. Haftverhalten des Metalls) und auf die Schottky-Barrierrhöhe (SBH) untersucht.

(i) Zusammenfassend läßt sich für das System "Gold auf C(111)-(1x1):H" feststellen, dass die ursprüngliche Wasserstoffbedeckung der (111)-Oberfläche durch Gold mit großer Sicherheit nicht verändert wird. Bei Raumtemperatur aufgedampft, zeigt Gold auf der hydrierten (111) Oberfläche ein homogenes Lagewachstum. Der spektroskopisch bestimmte Wert für die SBH (+0.3 eV) von Gold auf hydriertem Diamant stellt keine Energiebarriere für den Transport von Löchern dar, was gut mit dem ohmschen Kontaktverhalten aus Transportmes-

sungen übereinstimmt [117]. Schon bei relativ niedrigen Anlass-Temperaturen ( $500^{\circ}\text{C}$ ) zerfällt der zweidimensionale Goldfilm in isolierte Inseln. Die hydrierte Diamantoberfläche liegt dazwischen frei. Diese Inseln sind sehr mobil, was auf eine schlechte Adhäsion von Gold am Substrat hindeutet. Im Vergleich zu Gold in massiver Form erweisen sich die Inseln gegenüber einer Behandlung mit Königswasser (*aqua regia*) als sehr resistent.

(ii) Wie im Fall Gold auf C(111)-(1x1):H gibt es keine Hinweise darauf, dass die Wasserstoff-Terminierung durch Magnesium auf C(100)-(2x1):H beeinträchtigt wird. Ob dieser Befund in Zusammenhang mit einem zusätzlichen Anteil von Magnesiumoxid steht, der anhand des Mg2p Rumpfniveaus identifiziert wurde, ist noch nicht vollständig geklärt. Schon während des Aufdampfens bildet Magnesium dreidimensionale Inseln auf der hydrierten C(100) Oberfläche, was auf eine schwache Wechselwirkung an der Grenzschicht zwischen Metall und Diamant hinweist. Unter Berücksichtigung der stark inhomogenen Verteilung des Metalls konnte eine SBH für einen nominell  $25\text{\AA}$  dicken Magnesiumfilm auf C(100)-(2x1):H von  $0.85 \pm 0.15$  eV bestimmt werden, was wiederum gut mit Literaturwerten übereinstimmt [119, 120].

(iii) Um den Einfluss der Wasserstoff-Terminierung auf die SBH von Aluminium-Diamant-Grenzschichten zu untersuchen, wurde Aluminium auf eine Diamant (111) Oberfläche aufgedampft, die zuvor mittels Elektronenstrahl zu Hälfte dehydriert worden war. Auch hier zeigt sich eine Tendenz zur Inselbildung, die besonders stark auf dem mit Wasserstoff abgesättigten Teil ausgeprägt ist. Wie schon bei Gold und Magnesium ergeben Rumpfniveauspektren keine Hinweise auf eine chemische Bindung von Aluminium an Kohlenstoff. Zusätzlich konnte kein Einfluss von Aluminium auf die Wasserstoff-Terminierung anhand der Elektronenausbeute im Rasterelektronenmikroskop festgestellt werden. Die geringe energetische Verschiebung der Photoemissionsspektren mit zunehmender Aluminiumbedeckung ist unabhängig von der Terminierung der Oberfläche und spiegelt damit den geringfügigen Ladungstransfer zwischen Diamant und Aluminium wider.

Das abschließende Kapitel dieser Arbeit behandelte die Oberflächenleitfähigkeit von mit Wasserstoff abgesättigtem Diamant. Mittels spektroskopischer Daten in Verbindung mit Transport-Messungen wurde bewiesen, dass die Terminierung der Diamant-Oberfläche mit Wasserstoff nur eine notwendige, aber keine hinreichende Voraussetzung für eine hohe Oberflächenleitfähigkeit darstellt. Nur in Kombination mit Adsorbaten aus der Atmosphäre ist diese bei Halbleitern einmalige Eigenschaft beobachtbar. Aus den experimentellen Ergebnissen wurde ein elektrochemisches Modell entwickelt, welches die Oberflächenleitfähigkeit mit Elektronentransfer-Prozessen an der Grenze von Diamant und einem schwach sauren Wasserfilm erklärt. Im Rahmen dieses Modells wirken die im Wasserfilm gelösten Oxoniumionen ( $\text{H}_3\text{O}^+$ ) als Akzeptoren für Elektronen aus dem Diamanten. Dabei werden die Ionen zu molekuli-



larem Wasserstoff und Wasser reduziert. Die im Valenzband verbleibenden Löcher werden durch Anionen an der Oberfläche (z.B.  $\text{HCO}_3^-$ ) kompensiert. Aufgrund der Löcherdichte von  $10^{13}\text{cm}^{-2}$  [18, 20] muss das chemische Potential  $\mu_e$  des Wasserfilms mit der Position des VBM von Diamant an der Oberfläche energetisch entartet sein. Nur Wasserstoff-terminierter Diamant mit seiner negativen Elektronenaffinität von -1.3 eV kann diese Bedingung erfüllen, da bei anderen Halbleitern  $\mu_e$  weit oberhalb des VBM liegt. Kleine Änderungen in  $\mu_e$  relativ zum VBM und damit Änderungen in der Oberflächenleitfähigkeit lassen sich quantitativ mit der Nernst-Gleichung beschreiben, wobei in dieser Arbeit nur der pH-Wert des Wasserfilms und der  $\text{H}_2$ -Partialdruck berücksichtigt wurde. In einer kritischen Analyse wurde schließlich gezeigt, dass besonders in Zusammenhang mit pH-abhängigen Messungen [29] das Modell noch weiterer Verbesserungen bedarf.

Diamant Grenzflächen - sicherlich ein unerschöpfliches Thema! Es hat mich im Verlauf der ganzen Arbeit immer wieder verblüfft, wie oft dieser einfach gebaute Halbleiter mit seinen vier Valenzelektronen und seinen zwei Rumpfelektronen unerwartete Eigenschaften zeigte, und dass letztere hauptsächlich mit Wasserstoff in Verbindung standen, dem wirklich Einfachsten aller Elemente.



# Appendix A

## Low-threshold Electron Emission of Diamond (100)

The modification of the electron affinity  $\chi$  by hydrogen and oxygen has been thoroughly discussed in Chapter 4 for diamond (100) single crystal surfaces.  $\chi$  does not only play an important role for diamond-metal contact properties as shown in Chapter 5; as the electron affinity represents the energy step at the surface that has to be overcome by electrons escaping into vacuum,  $\chi$  also influences the electron emission properties of diamond decisively. In particular, the negative electron affinity (NEA) of hydrogenated diamond surfaces considerably enhances the photoelectron yield making diamond possibly a good candidate for cold cathode emitter and photocathode devices [89] once the problem of n-type doping has been resolved. This strong increase in electron yield has already been demonstrated in Chapter 5 for the hydrogenated diamond (100) surface by the low-energy cutoff of the photoemission spectra that has a characteristic peak when the surface is in its NEA state (Fig. 5.13). This so-called NEA-peak originates from thermalized electrons at the bottom of the conduction band that are released into vacuum. In addition to UPS, Total Photoelectron Yield Spectroscopy (TPYS) is another way to investigate the electron emission characteristics of the surface in detail as will be shown below. After a short introduction to the technique, TPY spectra of the hydrogenated and the chemically oxidized C(100) surface will be presented. These spectra have been recorded simultaneously to the work function and PES measurements shown in Chapter 4.

## A.1 Total photoelectron yield spectroscopy and electron affinity: general remarks

The total yield is defined as the number of emitted electrons from the surface per incident photon of an energy  $h\nu$  regardless of the kinetic energy of the photoelectrons. Applying the three-step model of photoemission as it has been described in Chapter 2.1.1, the dominant aspects in TPYS for the following discussion are the transport of excited electrons to the surface (step 2) and their release into vacuum (step 3). Electrons that are optically excited from occupied states into the conduction band may dissipate their excess kinetic energy by inelastic scattering with electrons and phonons. This thermalization process

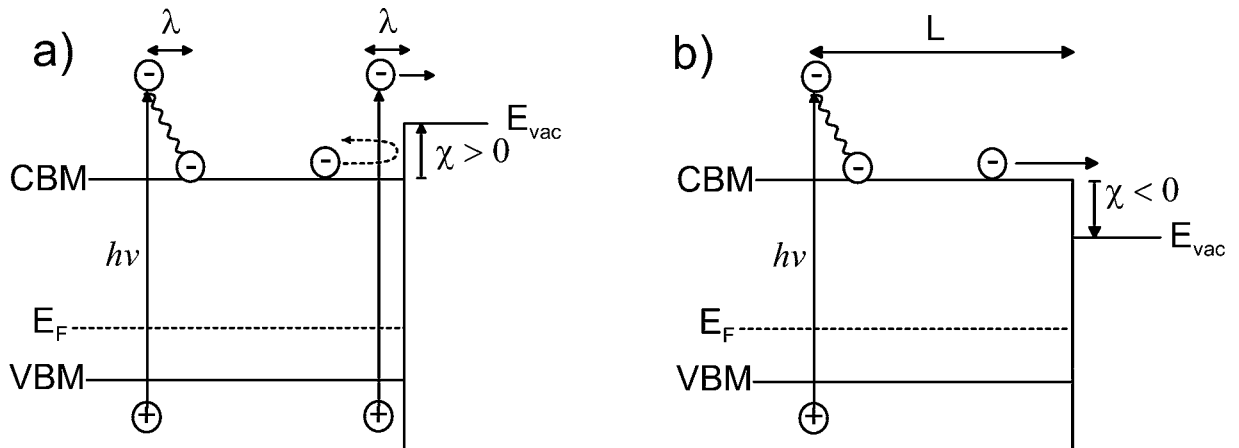


Figure A.1: Scheme of electron emission from a semiconductor under flat band conditions in the case of PEA (a) and NEA (b). For PEA, only electrons that are excited within the inelastic scattering length  $\lambda$  contribute to the electron yield. The situation is different in the case of NEA where the potential barrier is absent and thus, thermalized electrons within the diffusion length  $L$  are able to leave the surface.

occurs on a sub-picosecond time scale and within a spatial range corresponding to the inelastic scattering length  $\lambda$  of the order of 10-100Å [141]. Therefore, the vast majority of electrons in the conduction band are fully thermalized before reaching the surface and are thus repelled from the surface energy barrier in the common case of positive electron affinity (PEA) as depicted in Fig. A.1a. Hence, only electrons that are excited above the vacuum level within a distance  $\lambda$  from the surface contribute to the yield intensity. For surfaces exhibiting NEA, there is no surface barrier (see Fig. A.1b) and the escape depth is no longer limited by inelastic scattering but instead by the recombination rate of the electrons with holes. The corresponding diffusion length  $L$  is orders of magnitudes larger than  $\lambda$  and lies in the range of tenths of millimeters [130].

It is thus obvious that the surface sensitivity of TPYS is quite different for NEA and PEA. On account of the large diffusion length, the yield spectra reflect bulk rather than surface excitations in the case of NEA; for PEA, the spectra originate exclusively from processes that occur near the surface within the inelastic scattering length  $\lambda$ . Consequently, for exciting photon energies above the band gap energy  $E_{gap}$ , the electron yield is much higher in the case of NEA than in the case of PEA as demonstrated in Fig. A.2 for the diamond (100) surface. Plotting the spectra in particular on a linear scale (see insert), the strong increase in yield intensity at  $h\nu = E_{gap}$  is evident and it has been used as a fingerprint to indicate  $\chi < 0$  and thus for hydrogen termination (see Chapter 6.2).

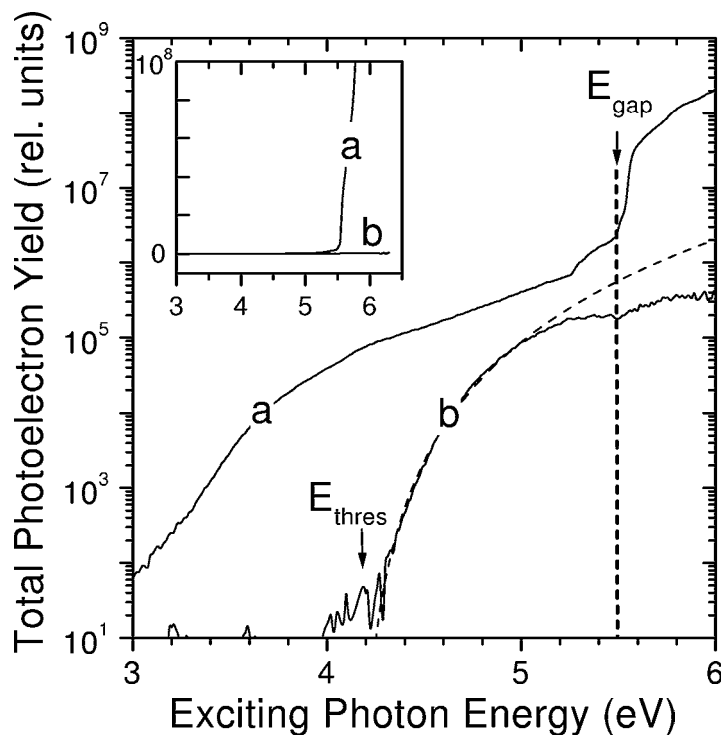


Figure A.2: Total photoelectron yield spectra of the C(100) surface after hydrogenation and annealing at 900°C in the state of NEA (a) and after chemical oxidization and annealing at 900°C in the state of PEA (b). The dashed line of spectrum b is an empirical fit of the sub-band gap emission according to Eq. A.1 with  $E_{thres} = 4.18 \pm 0.05$  eV. Plotted on a linear scale (insert), the large difference in yield intensity is clearly visible.

The photon energy regime between 5.25 eV and 5.6 eV (band gap regime) is dominated by the release of electrons at the CBM directly into vacuum states as sketched in Fig. A.1 or under participation of excitons that break up at the

surface. Both contributions give rise to the fine structure around the band gap energy of 5.5 eV as thoroughly discussed elsewhere [99, 130, 141–144]. For the following discussion, the shape of the yield spectra in the energy range around  $E_{gap}$  is only important in so far as it gives a clear indication of a PEA or NEA surface. In particular, the drop in intensity at the band gap energy of spectrum b in Fig. A.2 is characteristic for a diamond surface exhibiting clearly PEA as shown in previous experiments [130, 143, 144].

In the following, we shall focus on the energy range below 5.25 eV that will be further denoted as sub-band gap regime. The emitted electrons can originate from defect states in diamond (homogeneous emission) [141] or from *extrinsic* defect states of a non-diamond phase located at the surface (inhomogeneous emission) [143]. In the first case, one has to distinguish between bulk and surface defect states in diamond. Then, the photoemission threshold coincides either with the energy separation between the bulk defect level state  $E_d$  and the CBM or between the surface defect level state  $E_d$  and the vacuum level  $E_{vac}$  of diamond, respectively. The different scenarios for emission from occupied bulk and surface defects of diamond (“homogeneous emission model”) and the relationship between the electron affinity  $\chi$  and the photoelectric threshold  $E_{thres}$  are summarized in Fig. A.3.

The second case, namely the “inhomogeneous emission model” was first proposed by Cui *et al.* [143] analyzing yield spectra of diamond (111) surfaces with different electron affinities. The authors proved that the yield thresholds of hydrogenated and dehydrogenated C(111) single crystal surfaces do indeed track the changes in work function of diamond. In the framework of this inhomogeneous emission model [143], they proposed that the dominating defect states which give rise to the sub-band gap yield spectra originate from extended surface regions covered with a nondiamond phase as being graphite (or  $sp^2$ -rich amorphous carbon). We will label these surface regions “graphitic patches” as it was introduced by Cui *et al.* [143]. Provided that the extension of the patches are large enough to develop their own band structure (which we assume to be close to that of graphite in following), the semimetallic properties of graphite imply that the highest occupied  $\pi$  states and the lowest empty  $\pi^*$  states touch at the Fermi level. The main idea of this model relies to the fact that emitted electrons from the border of extended patches “see” effectively not the work function of graphite (5 eV) but the work function of the surrounding diamond matrix. As long as the work function of diamond is smaller than that of graphite, the threshold emission originates from electrons that are excited from the border of these patches, and the threshold  $E_{thres}$  coincides with the work function of diamond  $E_{thres} = \phi_{diamond}$ . When  $\phi_{diamond}$  exceeds the work function of graphite, the threshold is determined by electron emission from the center of the patches, and thus  $E_{thres} = \phi_{graphite}$  as shown in Fig. A.4 on top. Cui *et al.* gave a rough estimation of the lateral extension of the border zone

# homogeneous emission model (electron emission from occupied defect states)

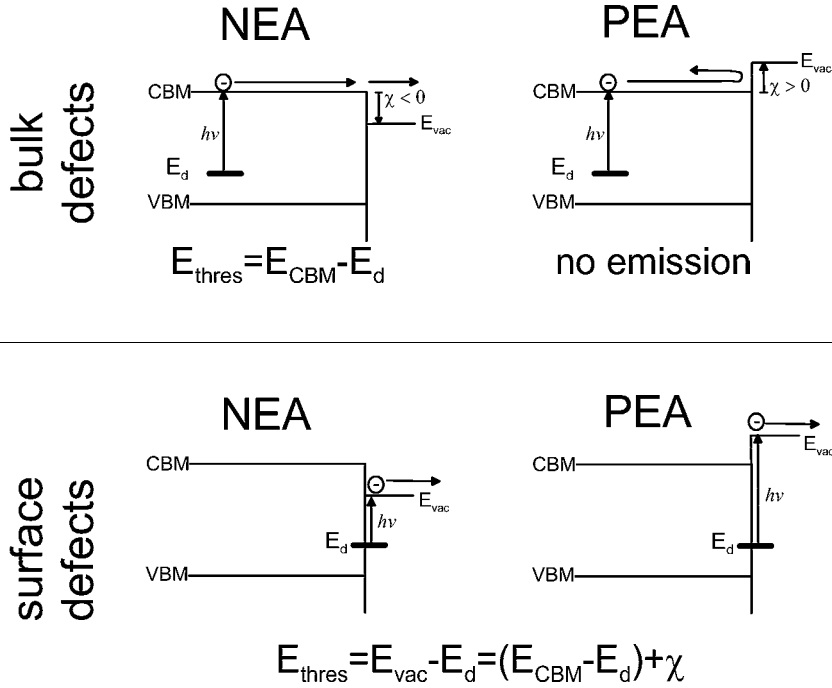


Figure A.3: Schematic diagrams of the energies involved in the homogeneous electron emission model (for details, see text).

of interest here which amounts to  $20\text{\AA}$  [143]. For patch diameters considerably less than  $40\text{\AA}$  (but large enough that the highest occupied states are located at  $E_F$ ), only the work function of diamond remains for electrons emitted from the whole area of the patches (see bottom panels of Fig. A.4).

To extract the threshold energies from the sub-band gap part of the yield spectra, Cui *et al.* demonstrated that the yield intensity  $Y(h\nu)$  is well described by a power law such as

$$Y(h\nu) = A \cdot (h\nu - E_{thres})^4, \quad (\text{A.1})$$

where  $A$  is the “amplitude” of the emission intensity and  $E_{thres}$  the threshold energy, respectively. As an example, the sub-band gap yield of spectrum b in Fig. A.2 is fitted by the dashed line according to Eq. A.1 with  $E_{thres} = 4.18 \pm 0.05$  eV. <sup>1</sup>

<sup>1</sup>It should be mentioned that a detailed theoretical analysis of yield spectra from semicon-

## inhomogeneous emission model (electron emission from graphitic patches)

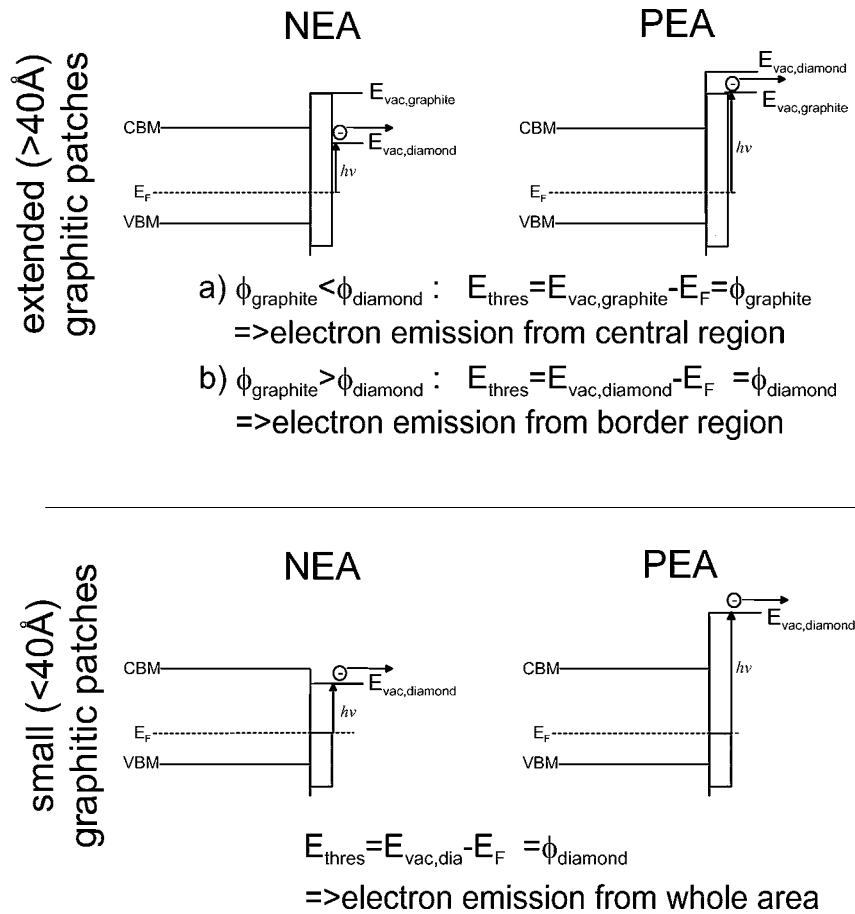


Figure A.4: Schematic diagrams of the energies involved in the inhomogeneous electron emission model (for details, see text).

As shown in Chapter 4, the work function depends strongly on the adsorbate coverage and varies between 3.5 eV for the fully hydrogen terminated (100) surface and 6.4 eV for the chemically oxidized surface. In the case of emission from isolated defects in diamond (homogeneous electron emission) or in the case of the inhomogeneous emission model, significant variations in threshold energies are thus expected.

ductor surfaces by Kane [145] also gives a power law behavior for the yield near threshold. Exponents between 1 and 2.5 are assigned to different processes involved such as direct or indirect optical excitations, excitations from volume or surface states, and presence or absence of  $k$ -conservation during the photoemission process. Although he never found an exponent of four in his analysis, we adapt the parameterization of the sub-band gap diamond yield spectra according to Eq.A.1 as proposed by Cui *et al.* [143].



Finally, it should be mentioned that TPYS is very similar to photoconductivity measurements where charge carriers are excited out of defects or by the formation of electron-hole pairs, and generate a photocurrent between two contacts. In TPYS, one contact is replaced by the free surface of the sample and, in contrast to conductivity experiments, only electrons are detected. The technique can thus be used as a very sensitive tool (note the logarithmic scale in Fig. A.2) for spectroscopic investigations of occupied bulk defect states located in the gap region of diamond with a NEA surface.

The reported yield spectra were measured in UHV for photon energies between 2.0 and 6.0 eV using a xenon arc lamp for excitation. The light was passed through a double grating monochromator for stray light reduction better than  $10^{-9}$ , and was focused onto the sample through a UV transparent window. Part of the light was deflected by a beam splitter to measure the incident photon flux for the normalization of the electron count rate. Photoelectrons regardless of their kinetic energy are focused by optimized electron optics into a channeltron (for details, see Ref. [47]).

## A.2 Total photoelectron yield spectra of the hydrogenated diamond (100) surface

In Fig. A.5, yield spectra of the plasma hydrogenated and mildly annealed C(100) surface are depicted. All surfaces had NEA as indicated by the fingerprint in yield at  $h\nu = 5.5$  eV. The “as-prepared” surface (spectrum 1) did not

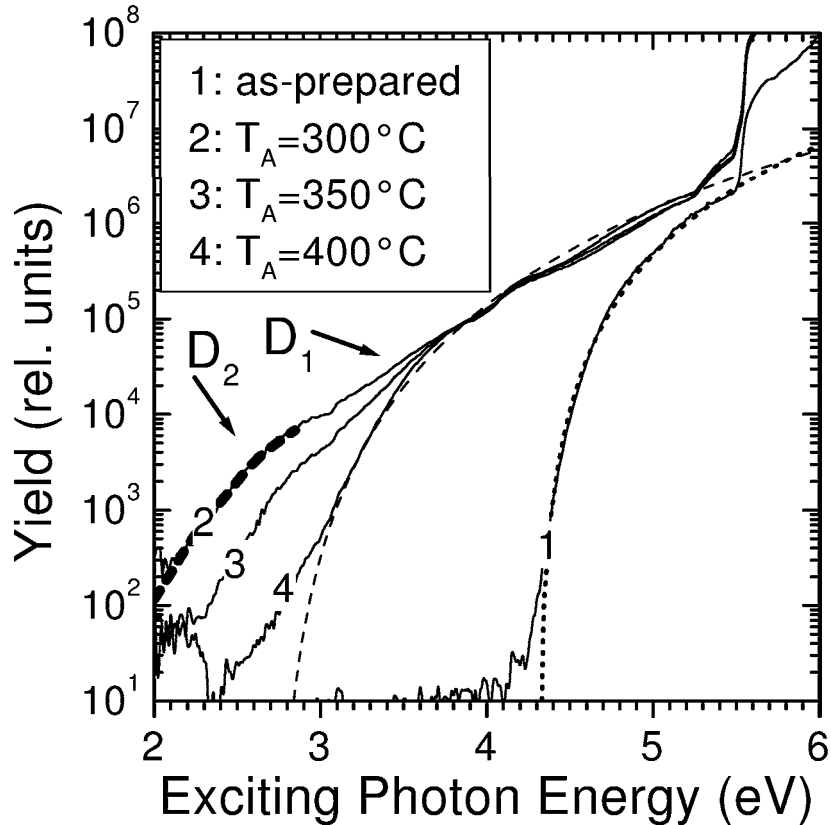


Figure A.5: TPY spectra of the diamond (100) single crystal surface after hydrogen plasma treatment (spectrum 1) and after annealing in UHV at different annealing temperatures  $T_A$  up to 400°C (spectra 2-4). The dashed lines along spectrum 2 and 4 are fits according to Eq. A.1. The dotted line along spectrum 1 is fitted using an exponent 3 instead of 4 in Eq. A.1 (for details, see text).

show considerable intensity in the photon energy range between 2 and 4 eV. In addition, it was not possible to fit the sub-band gap band of spectrum 1 according to Eq. A.1. However, an excellent fit was achieved by an exponent 3 instead of 4 in the power law (dotted line in Fig. A.5) which was close to 2.5 as predicted by Kane in the case of indirect optical excitations from bulk or surface states [145]. It is thus reasonable to assume that the plasma treated

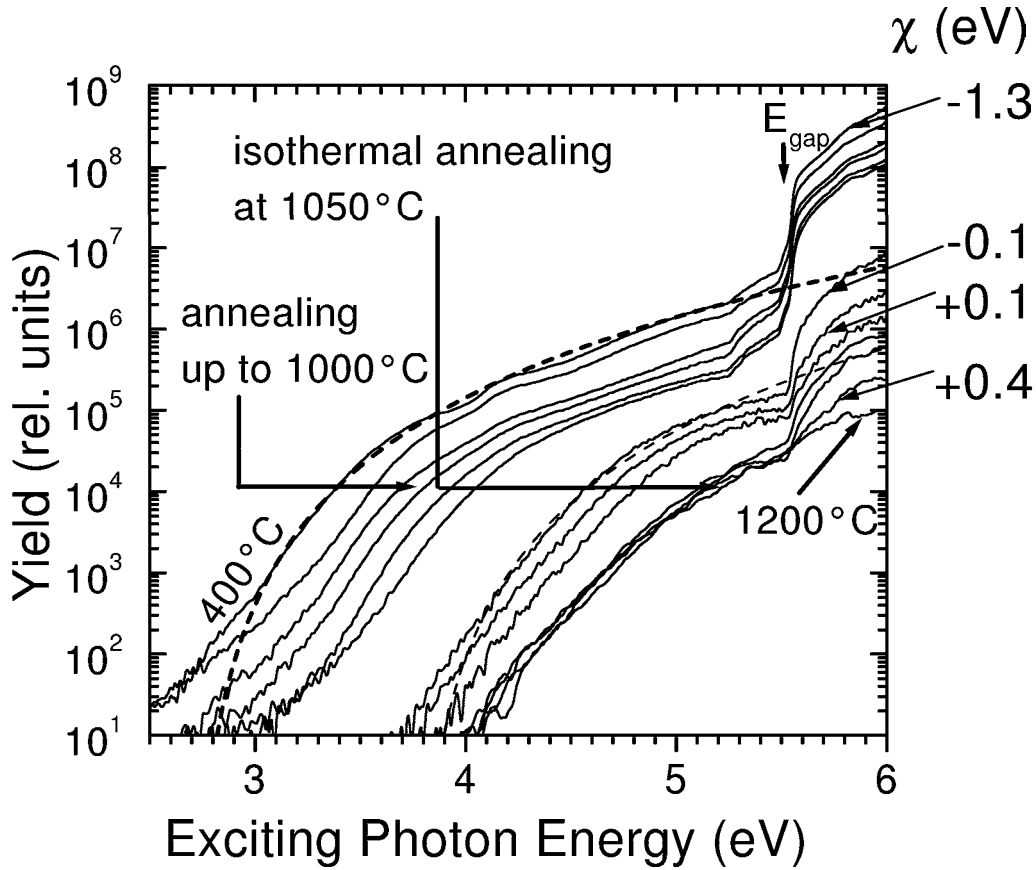


Figure A.6: Selected total photoelectron yield spectra of the plasma hydrogenated C(100) surface during annealing up to 1200°C. The dashed lines are empirical fits to the sub-band gap emission band according to Eq. A.1. The spectra corresponding to surfaces with minimum (-1.3 eV) and maximum (+0.4 eV) electron affinity and the crossing from negative to positive electron affinity (-0.1 and +0.1 eV) as measured in Chapter 4.3 are indicated.

surface contained but a very low concentration of defects and the yield spectrum was thus dominated by emission from valence band states of diamond itself.

After the first annealing step the sub-band gap yield intensity extended below 2 eV photon energy, and two defect related thresholds  $D_1$  and  $D_2$  were discernible as shown in Fig. A.5. The threshold energies derived from Eq. A.1 corresponded to  $1.5 \pm 0.1$  eV (thick dashed line,  $D_1$ ) and  $2.5 \pm 0.2$  eV ( $D_2$ ), respectively. These defect states have also been observed in single crystals with (111) surface orientation [130] and CVD films [141]. Excitation with photon energies around 2 eV implied that these defect states with energies well above mid-gap and thus far above the Fermi level were occupied. Therefore, they were obviously not in thermal equilibrium. Ristein and co-workers showed, that

they are optically pumped by the probe light of the experiment itself [141]. It is interesting to note that this effect was only observed in our experiment on C(100) after the first annealing step and not for the “as-prepared” surface. One can speculate that partial desorption of physisorbates which are present after plasma preparation [54] is related with the presence of the  $D_2$  defect band. The  $D_2$  band intensity decreased during subsequent annealing, and after the 400°C annealing step, the  $D_1$  band dominated the yield spectrum (spectrum 4 in Fig. A.5). It is the  $D_1$  band that is ascribed to emission from graphite-like surface defects in the framework of the inhomogeneous emission model by Cui *et al.* [143].

In the following, the C(100) surface was annealed up to 1200°C. Selected yield spectra of the whole annealing sequence that was already discussed in Chapter 4.3 are shown in Fig. A.6. Starting from the first spectrum after 400°C annealing, the shape of the sub-band gap spectra remained very similar; even the 1200°C spectrum did not show significant changes in the sub-band gap regime despite the fact of increased surface graphitization as witnessed by an increase in diffuse background LEED intensity. Apparently, the spectra shifted rigidly towards higher photon energies. No significant change in emission intensity as witnessed by the parameter  $A$  in Eq. A.1 were observed. By adaption of Eq. A.1 to the sub-band gap yield, the corresponding threshold energies  $E_{thres}$  were extracted as shown by the dashed lines in Fig. A.6 for two selected spectra (spectrum after 400°C annealing and when the surface exhibited  $\chi = -0.1$  eV). As it was already observed on C(111) [143], the changes in threshold energies on C(100) obtained were within the error bars identical with the changes in work function as determined by the Kelvin method (see Fig. A.7). In fact, the constant difference between work function and threshold energy  $\phi - E_{thres} = 0.7 \pm 0.15$  eV is due to the thermal occupation of states above  $E_F$  which is known from the photoyield of metals<sup>2</sup> [46]. Therefore, the threshold energies measured virtually coincided with the work function. As long as the work function of diamond was below that of graphite, no conclusions could be drawn with respect to the lateral extension of the graphitic patches (remember Fig. A.4 for a NEA surface!). However, after the 1200°C annealing step (last spectrum in Fig. A.7) the work function increased by 0.4 eV to 5.5 eV whereas the threshold did not change. Hence, in this case, the electrons were thus emitted from the center region of extended patches and the threshold was determined by the lower work function (5 eV) of graphite (see Fig. A.4). At this annealing temperature, the yield spectrum shown in Fig. A.6 was completely structureless around 5.5 eV, and the shape of the spectrum was very similar in shape to one obtained from graphite [143]. This supports the existence of extended graphitic regions as deduced from the yield threshold,

---

<sup>2</sup>An example of a yield spectrum of gold is depicted in Fig. 2.7; in this case the difference between  $\phi$  and  $E_{thres}$  is estimated to  $0.4 \pm 0.2$  eV.

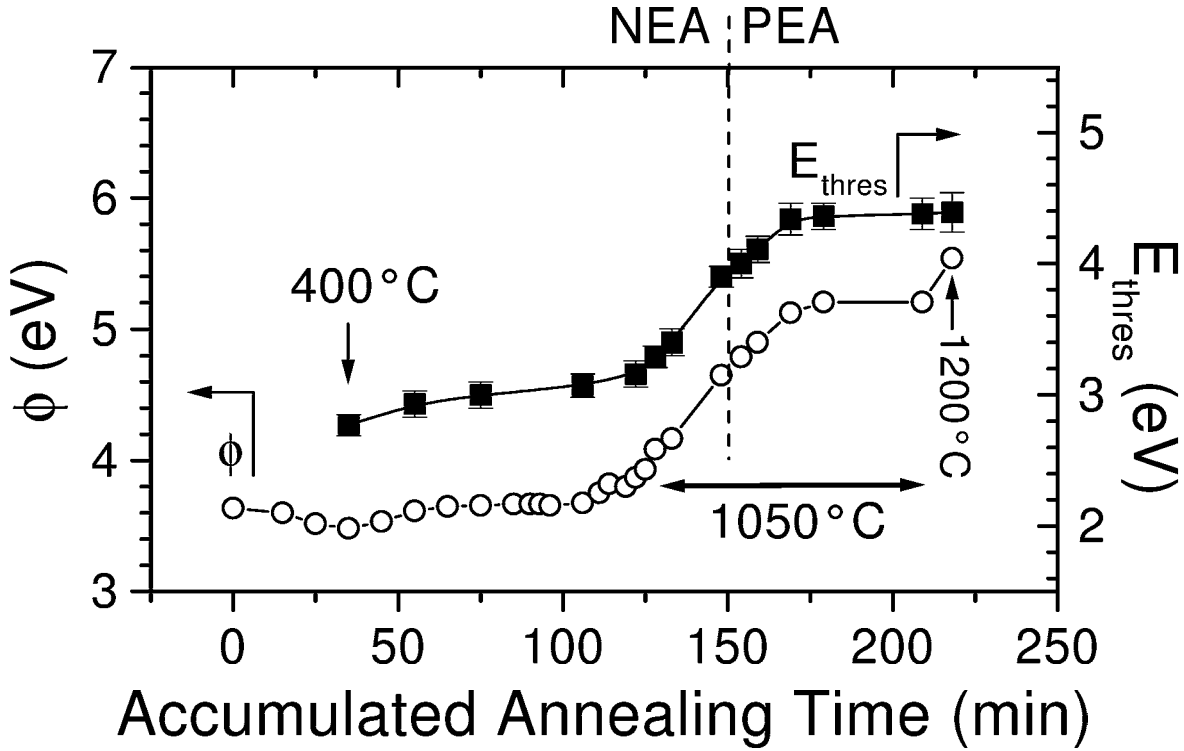


Figure A.7: Work function  $\phi$  and photoelectric yield threshold  $E_{thres}$  of the sub-band gap part of the spectra as a function of accumulated annealing time.

and is in concordance with surface graphitization after 1200°C annealing as witnessed by LEED.

Our results on C(100) thus corroborate the inhomogeneous emission model of Cui *et al.* which has been derived for yield spectra of C(111) in a similar experiment [143].

However, comparing the yield spectra measured by Cui (Fig. A.8) during the transition from NEA to PEA for C(111) with those presented in Fig. A.6 for C(100), the most significant differences were detected in the photon energy range between 5.2 and 6 eV. On C(111), the PEA spectra in Fig. A.8 clearly showed a dip at  $E_{gap}$ , and the yield was considerable lower between 5.5 and 6 eV photon energy than the extrapolation of the sub-band gap yield into this energy range (dotted line in Fig. A.8). As already mentioned, these spectral features are typical of a well-defined diamond surface exhibiting PEA. Contrary to C(111), all spectra of C(100) in Fig. A.6 with the exception of the spectrum after annealing at 1200°C had the sharp increase in yield at  $h\nu = 5.5$  eV which was typical for a NEA surface.

The differences between C(111) and C(100) are probably due incomplete hydrogen desorption. Under the assumption that dehydrogenation during an-

nealing occurs less homogeneously on C(100) than on C(111), most of the (100) surface can be dehydrogenated, and the surface exhibit PEA as measured by an area averaging method such as the Kelvin method. Nevertheless, the residual hydrogenated parts of the surface with lower emission thresholds will still give rise to the steep increase in yield above 5.5 eV photon energy due to the high sensitivity of TPYS for surfaces with NEA (see Fig. A.1). However, there is no indication from the literature that dehydrogenation during annealing of C(111) and C(100) is significantly different with respect to homogeneity.

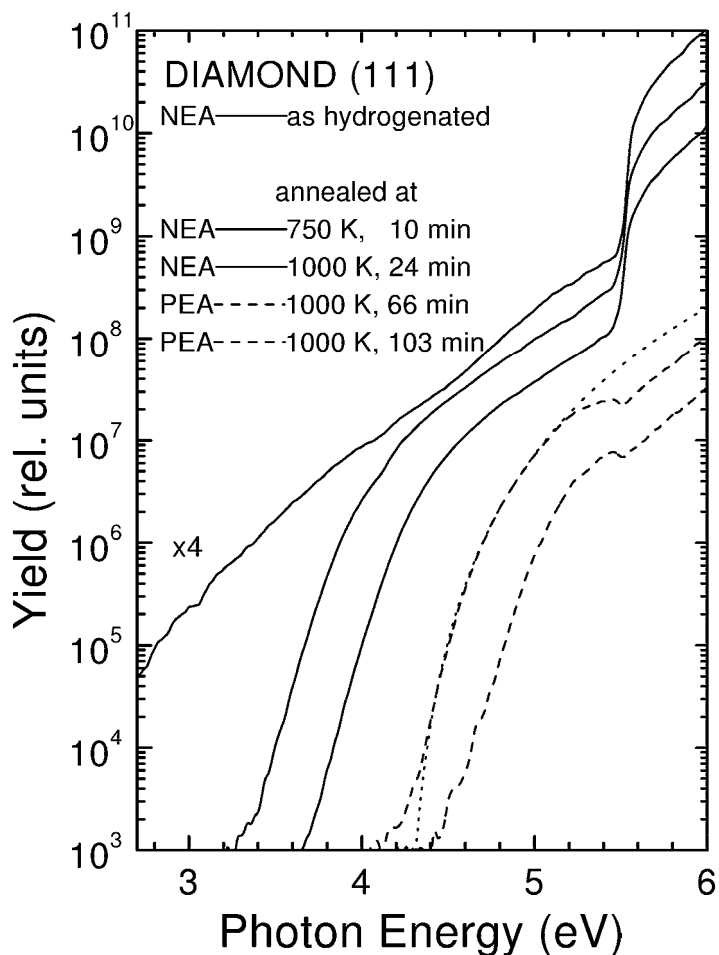


Figure A.8: Evolution of yield spectra of the plasma hydrogenated C(111) surface during annealing (data are taken from Ref. [143]). The annealing temperature and time are indicated in the figure together with the status of electron affinity (solid lines for NEA and dashed lines for PEA). The dotted line is an empirical fit according to Eq. A.1.

### A.3 Total photoelectron yield spectra of the chemically oxidized diamond (100) surface

As shown in Chapter 4.4, the work function of the hydrogenated C(100) surface drastically changed from 3.4 eV to 5.8 eV when the sample was chemically oxidized. The corresponding yield spectra are depicted in Fig. A.9. It is obvious

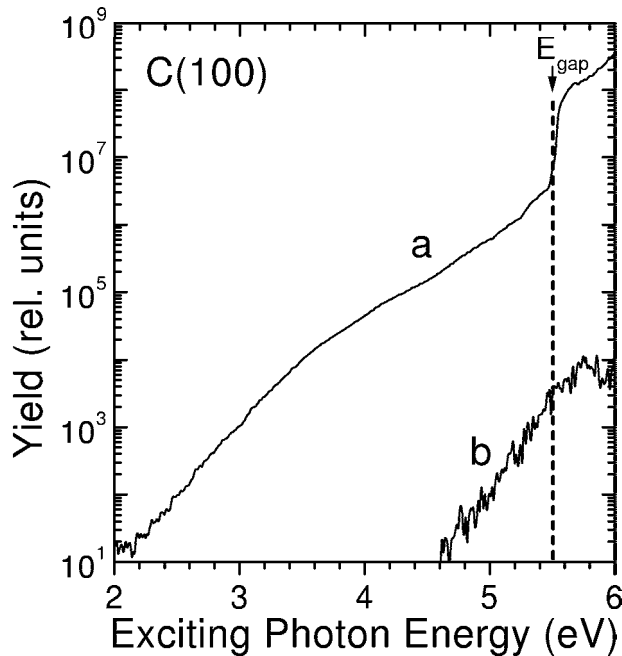


Figure A.9: Total photoelectron yield spectra of the plasma hydrogenated C(100) surface after mild annealing at 400°C (spectrum a) and after subsequential boiling in a mixture of H<sub>2</sub>SO<sub>4</sub> and HNO<sub>3</sub> for oxidation (spectrum b).

that the chemical treatment effectively reduced the electron yield at least by three orders of magnitude in the sub-band gap range<sup>3</sup>. In fact, spectrum b of Fig. A.9 was recorded at the detection limit of our TPYS setup and did not provide significant photoelectric threshold values. One could thus only deduce a lower limit for  $E_{thres}$  of  $5.1 \pm 0.3$  eV.

In order to investigate the evolution of the TPY spectra in the sub-band gap range, an initially dehydrogenated (100) diamond was chemically oxidized and subsequently annealed in UHV from 430°C up to 900°C. The corresponding yield spectra are shown in Fig. A.10. All spectra had the characteristics of PEA. Even the dip at  $h\nu = E_{gap}$  was clearly visible. Contrary to the hydrogenated C(100) surface, the sub-band gap emission shifted rigidly towards

<sup>3</sup>A comparable decrease in photocurrent was already observed in photoconductivity measurements of CVD films when oxygen had been added to the growth process [146]

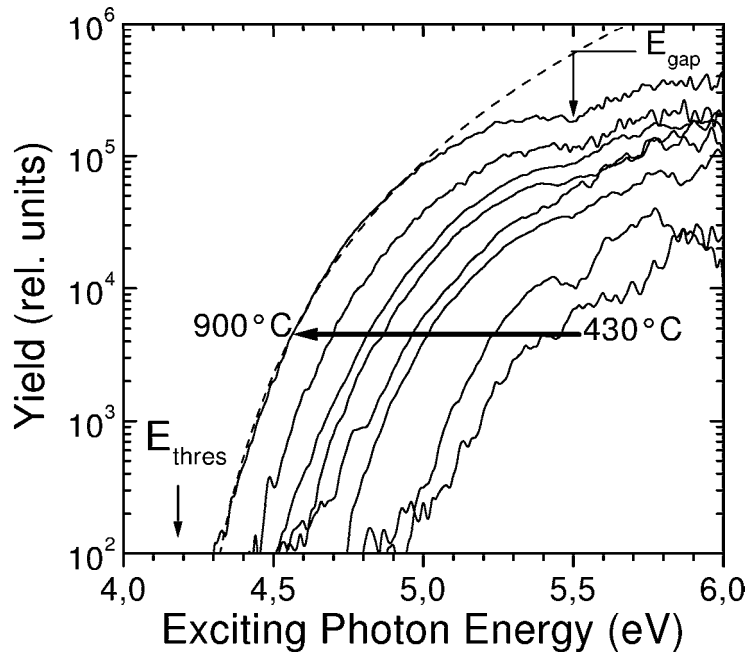


Figure A.10: Selected total photoelectron yield spectra of the chemically oxidized C(100) surface during annealing up to 900°C. The dashed line represents an empirical fit to the sub-band gap emission band according to Eq. A.1.

lower photon energies with increasing annealing temperature, i.e. towards lower photoelectric threshold  $E_{thres}$ .

In Fig. A.11b,  $E_{thres}$  and the work function  $\phi$  measured with the Kelvin probe are plotted versus the accumulated annealing time  $t_A$ . As seen in the previous experiment for the hydrogenated C(100) surface,  $E_{thres}$  and  $\phi$  of the oxidized surface changed simultaneously during the experiment. During the whole experimental sequence, the work function  $\phi$  of diamond exceeded the work function of graphite (5 eV). Since the threshold varies with the work function of diamond, the electron emission cannot stem from extended graphitic patches; otherwise, one would expect a constant threshold at 5 eV (Fig. A.4). Therefore, the defect states that gave rise to the sub-band gap yield in the case of the PEA surface were either isolated surface defects of diamond (see Fig. A.3) or small (diameter  $< 40\text{\AA}$ ) graphitic patches on the surface (Fig. A.4). Since the shape of the sub-band gap spectra of the oxidized surface was very similar to that measured during annealing of the hydrogenated one (which was ascribed to emission from surface graphitic patches), the second scenario of inhomogeneous emission from small graphitic patches most probably holds true for the oxidized surface as well. The offset  $\phi - E_{thres} = 0.7 \pm 0.2$  eV was thus due to thermal occupation statistics as it was the case for the hydrogenated C(100) surface.



The increase in emission intensity as witnessed by the change in parameter  $A$  of Eq. A.1 during the annealing sequence as shown in Fig. A.11a) indicated an increasing number of graphitic patches. Thus, most of the low-threshold emission sites were formed during thermal annealing itself and were effectively reduced by the preceding acid treatment. In this context, surface graphitization of diamond can thus be observed by means of total photoelectron yield spectroscopy.

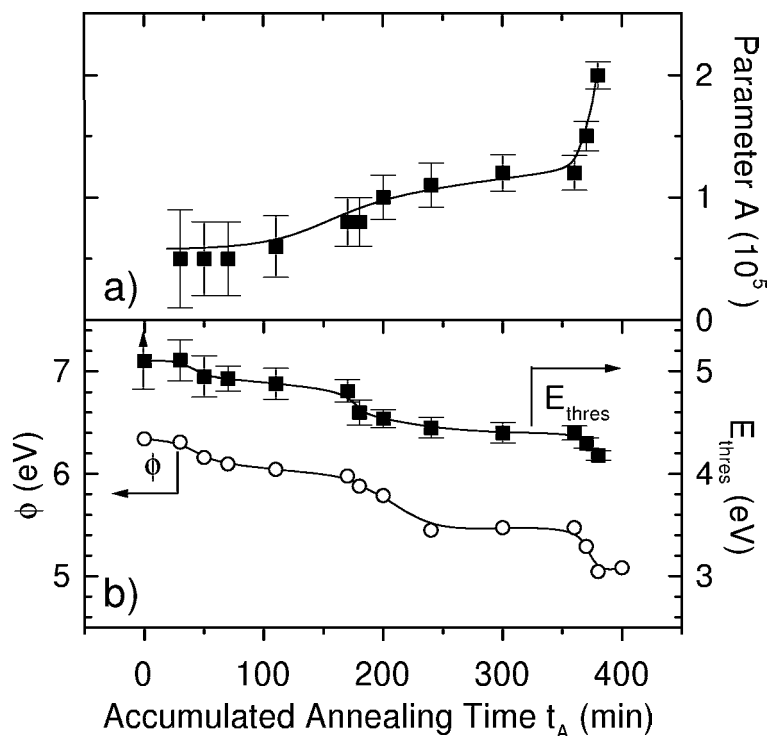


Figure A.11: Emission amplitude parameter  $A$  (a) and work function  $\phi$  and photoelectric yield threshold  $E_{thres}$  (b) of the chemically oxidized C(100) surface as a function of accumulated annealing time  $t_A$ .  $A$  and  $E_{thres}$  are derived by fitting the whole set of yield spectra according to Eq. A.1.

## A.4 Summary

Our results observed for the sub-band gap electron emission properties from hydrogenated and oxidized diamond (100) surfaces by means of total photoelectron yield spectroscopy are well described by the inhomogeneous emission model that has been proposed by Cui and co-workers [143] taking the lateral extensions of the emission sites into account. In this model, the dominant electron emission does not originate from diamond but from graphitic patches at the surface which provide a finite density of occupied states at the Fermi level. The surrounding diamond matrix, however, influences the photoelectric threshold  $E_{thres}$  of the emission sites by its work function  $\phi$ . In the case of the hydrogenated and the chemically oxidized C(100) surface,  $\phi$  and  $E_{thres}$  change simultaneously with adsorbate coverage; both quantities are - apart from an offset of  $0.7 \pm 0.2$  eV that is explained by occupation statistics - identical. Both, hydrogen plasma and acid treatment, effectively reduce the sub-band gap intensity.

# Bibliography

- [1] *Low-Pressure Synthetic Diamond - Manufacturing and Applications*, Springer Series in Materials Processing, edited by B. Dischler and C. Wild (Springer, Berlin, 1998).
- [2] *The Properties of Natural and Synthetic Diamond*, edited by J. E. Field (Academic Press, San Diego, 1992).
- [3] *Properties and Applications of Diamond*, edited by E. Wilks and J. Wilks (Butterworth-Heinemann Ltd., Oxford, 1994).
- [4] R. F. Davis, *Diamond Films and Coatings* (Noyes Publications, New Jersey, 1993).
- [5] H. Okushi, *Diamond Relat. Mater.* **10**, 281 (2001).
- [6] K. Janischowsky, M. Stammler, R. Stöckel, and L. Ley, *Appl. Phys. Lett.* **75**, 2094 (1999).
- [7] K. Janischowsky, M. Stammler, and L. Ley, *Diamond Relat. Mater.* **8**, 179 (1999).
- [8] S. Koizumi, M. Kamo, Y. Sato, H. Ozaki, and T. Inuzuka, *Appl. Phys. Lett.* **71**, 1065 (1997).
- [9] I. Sakaguchi, M. Nishitani-Gamo, Y. Kikuchi, E. Yasu, H. Haneda, T. Suzuki, and T. Ando, *Phys. Rev. B* **60**, R2139 (1999).
- [10] M. Nishitani-Gamo, C. Xiao, Y. Zhang, E. Yasu, Y. Kikuchi, I. Sakaguchi, T. Suzuki, Y. Sato, and T. Ando, *Thin Solid Films* **382**, 113 (2001).
- [11] E. Kohn and W. Ebert, in *Low-Pressure Synthetic Diamond*, edited by B. Dischler and C. Wild (Springer, Berlin, 1998).
- [12] M. I. Landstrass and K. V. Ravi, *Appl. Phys. Lett.* **55**, 975 (1989).
- [13] M. I. Landstrass and K. V. Ravi, *Appl. Phys. Lett.* **55**, 1391 (1989).

- [14] S. A. Grot, G. S. Gildenblatt, C. W. Hatsfield, C. R. Wronski, A. R. Badzian, T. Badzian, and R. Messier, *IEEE Electron Device Lett.* **11**, 100 (1990).
- [15] T. Maki, S. Shikama, M. Komori, Y. Sakagushi, K. Skuta, and T. Kobayashi, *Jpn. J. Appl. Phys.* **31**, L1446 (1992).
- [16] Y. Mori, M. Deguchi, A. Hatta, T. Ito, T. Sasaki, and A. Hiraki, *Jpn. J. Appl. Phys.* **32**, L987 (1993).
- [17] S. Albin and L. Watkins, *Appl. Phys. Lett.* **56**, 1454 (1990).
- [18] K. Hayashi, S. Yamanaka, and H. Watanabe, *J. Appl. Phys.* **81**, 744 (1997).
- [19] N. Jiang and T. Ito, *J. Appl. Phys.* **85**, 8267 (1999).
- [20] S. Yamanaka, D. Takeuchi, H. Watanabe, H. Okushi, and K. Kajimura, *Appl. Surf. Sci.* **159-160**, 567 (2000).
- [21] F. Maier, M. Riedel, B. Mantel, J. Ristein, and L. Ley, *Phys. Rev. Lett.* **85**, 3472 (2000).
- [22] K. Tsugawa, K. Kitatani, H. Noda, A. Hokazono, M. Tajima, and H. Kawarada, *Diamond Relat. Mater.* **8**, 927 (1999).
- [23] S. G. Ri, K. Tashiro, S. Tanaka, T. Fujisawa, H. Kimura, T. Kurosu, and M. Iida, *Jpn. J. Appl. Phys.* **38**, 3492 (1999).
- [24] A. Denisenko, A. Aleksov, A. Pribil, P. Gluche, W. Ebert, and E. Kohn, *Diamond Relat. Mater.* **9**, 1138 (2000).
- [25] H. Kawarada, M. Aoki, and M. Ito, *Appl. Phys. Lett.* **65**, 1563 (1994).
- [26] W. Ebert, A. Vescan, P. Gluche, T. Borst, and E. Kohn, *Diamond Relat. Mater.* **6**, 329 (1997).
- [27] H. Kawarada, *Surf. Sci. Rep.* **26**, 205 (1996).
- [28] H. Kawarada, *proc. The First Crest Symposium, Ohhtemachi, Japan* (unpublished).
- [29] A. Denisenko, A. Aleksov, and E. Kohn, *Diamond Relat. Mater.* **10**, 667 (2001).
- [30] M. Adamschik, M. Hinz, C. Maier, P. Schmid, H. Seliger, E. P. Hofer, and E. Kohn, *Diamond Relat. Mater.* **10**, 722 (2001).

- [31] M. Henzler and W. Göpel, *Oberflächenphysik des Festkörpers* (Teubner, Stuttgart, 1991).
- [32] D. P. Woodruff and T. A. Delchar, *Modern Techniques of Surface Science* (Cambridge University Press, Cambridge, 1990).
- [33] G. Ertl and J. Küppers, *Low Energy Electrons and Surface Chemistry* (Verlag Chemie, Weinheim, 1974), p. 168.
- [34] M. Cardona and L. Ley, in *Photoemission in Solids I, Topics in Applied Physics* **26**, edited by M. Cardona and L. Ley (Springer, Berlin Heidelberg New York, 1978).
- [35] S. Hüfner, *Photoelectron Spectroscopy, Springer Series in Solid-State Science 82* (Springer, Berlin, 1995).
- [36] A. Einstein, *Ann. Phys.* **17**, 132 (1905).
- [37] W. Mönch, *Semiconductor Surfaces and Interfaces, Springer Series in Surface Science 26* (Springer, Berlin, 1995).
- [38] J. Ristein, F. Maier, M. Riedel, J. B. Cui, and L. Ley, *Phys. Stat. Sol. (a)* **181**, 65 (2000).
- [39] G. S. Painter, D. E. Ellis, and A. R. Lubinsky, *Phys. Rev. B* **4**, 3610 (1971).
- [40] R. Graupner, Ph.D. thesis, Universität Erlangen-Nürnberg, 1997.
- [41] J. Faul, G. Neuhold, L. Ley, J. Fraxedas, S. Zollner, J. D. Riley, and R. C. G. Leckey, *Phys. Rev. B* **47**, 12625 (1993).
- [42] J. J. Yeh, *Atomic Calculation of Photoionization Cross-Sections and Asymmetry Parameters* (Gordon and Breach Science Publishers, Langhorne, 1993).
- [43] J. W. F. Egelhoff Jr., *Surf. Sci. Rep.* **6**, 253 (1987).
- [44] J. Hölzl and F. K. Schulte, *Solid Surface Physics, Springer Tracts in Modern Physics* **85** (Springer, Berlin, 1979).
- [45] N. W. Ashcroft and N. D. Mermin, *Solid State Physics*, international ed. (W. Saunders Company, Philadelphia, 1976), p. 342.
- [46] R. H. Fowler, *Phys. Rev.* **38**, 45 (1931).
- [47] J. Schäfer, J. Ristein, L. Ley, and H. Ibach, *Rev. Sci. Instrum.* **64**, 653 (1993).

- [48] M. A. van Hove, W. H. Weinberg, and C. M. Chan, *Low-Energy Electron Diffraction* (Springer, Berlin, Heidelberg, 1986).
- [49] R. Graupner, J. Ristein, and L. Ley, *Surf. Sci.* **320**, 201 (1994).
- [50] B. D. Thoms, M. S. Owens, J. E. Butler, and C. Spiro, *Appl. Phys. Lett.* **65**, 2957 (1994).
- [51] O. M. Küttel, L. Diederich, E. Schaller, O. Carnal, and L. Schlapbach, *Surf. Sci.* **337**, L812 (1995).
- [52] J. Kinsky, private communication (unpublished).
- [53] B. F. Mantel, M. Stammer, J. Ristein, and L. Ley, *Diamond Relat. Mater.* **9**, 1032 (2000).
- [54] R. Graupner, F. Maier, J. Ristein, L. Ley, and C. Jung, *Phys. Rev. B* **57**, 12397 (1998).
- [55] R. Graupner, M. Hollering, A. Ziegler, J. Ristein, and L. Ley, *Phys. Rev. B* **55**, 10841 (1997).
- [56] F. Maier, R. Graupner, M. Hollering, L. Hammer, J. Ristein, and L. Ley, *Surf. Sci.* **443**, 177 (1999).
- [57] R. E. Stallcup and J. M. Perez, *Phys. Rev. Lett.* **86**, 3368 (2001).
- [58] J. Ristein, *Electronic Properties of Diamond Surfaces* (Universität Erlangen-Nürnberg, Erlangen, 1998).
- [59] G. Kern, J. Hafner, J. Furthmüller, and G. Kresse, *Surf. Sci.* **357-358**, 422 (1996).
- [60] G. Kern, J. Hafner, and G. Kresse, *Surf. Sci.* **366**, 464 (1996).
- [61] K. C. Pandey, *Phys. Rev. B* **25**, 4338 (1982).
- [62] J. Furthmüller, J. Hafner, and G. Kresse, *Phys. Rev. B* **53**, 7334 (1996).
- [63] J. Furthmüller, J. Hafner, and G. Kresse, *Phys. Rev. B* **53**, 7334 (1996).
- [64] G. Kern and J. Hafner, *Phys. Rev. B* **56**, 4203 (1997).
- [65] J. Ristein and R. Graupner, *Adv. Solid State Phys.* **36**, 77 (1997).
- [66] B. B. Pate, *Surf. Sci.* **165**, 83 (1986).
- [67] G. Kern, J. Hafner, and G. Kresse, *Surf. Sci.* **366**, 445 (1996).

- [68] C. J. Chu, M. P. D'Evelyn, R. H. Hauge, and J. L. Margrave, *J. Appl. Phys.* **70**, 1695 (1991).
- [69] C. L. Cheng, C. H. Chang, J. C. Lin, and K. L. Song, *Phys. Rev. Lett.* **78**, 3713 (1997).
- [70] T. W. Mercer, J. N. Russell, and P. E. Pehrsson, *Surf. Sci.* **392**, L21 (1997).
- [71] C. C. Battaile, D. J. Srolovitz, and J. E. Butler, *Diamond Relat. Mater.* **6**, 1198 (1997).
- [72] C. C. Battaile, D. J. Srolovitz, and J. E. Butler, *J. Crystal Growth* **194**, 353 (1998).
- [73] K. E. Spear and M. Frenklach, *Pure Appl. Chem.* **66**, 1773 (1994).
- [74] P. G. Lurie and J. M. Wilson, *Surf. Sci.* **65**, 453 (1977).
- [75] M. I. Heggie, G. Jungnickel, and C. D. Latham, *Diamond Relat. Mater.* **5**, 236 (1996).
- [76] H. M. Strong and R. M. Chrenko, *J. Phys. Chem.* **75**, 1838 (1971).
- [77] R. C. Burns, V. Cvetkovic, C. N. Dodge, D. J. F. Evans, M. T. Rooney, P. M. Spear, and C. M. Welbourn, *J. Crystal Growth* **104**, 257 (1990).
- [78] J. Ristein, *6<sup>th</sup> International Workshop on Surface and Bulk Defects of CVD Diamond Films* (Conf. Proceedings, Hasselt, Belgium, March 2001).
- [79] B. N. Davidson and W. E. Pickett, *Phys. Rev. B* **49**, 11253 (1994).
- [80] D. R. Alfonso, D. A. Drabold, and S. E. Ulloa, *Phys. Rev. B* **51**, 14669 (1995).
- [81] S. V. Pepper, *J. Vac. Sci. Technol.* **20**, 213 (1981).
- [82] G. Francz, P. Kania, G. Ganter, H. Stupp, and P. Oelhafen, *Phys. Stat. Sol. A* **154**, 91 (1991).
- [83] M. R. Jarvis, R. Perez, F. van Boulen, and M. C. Payne, *Phys. Rev. Lett.* **80**, 3428 (1998).
- [84] R. C. G. Leckey and J. D. Riley, *Appl. Surf. Sci.* **22**, 195 (1985).
- [85] J. B. Cui, J. Ristein, and L. Ley, *Phys. Rev. B* **59**, 5847 (1999).
- [86] K. Heinz and L. Hammer, *Z. Kristallogr.* **213**, 615 (1998).

- [87] M. Henzler, Surf. Rev. Lett. **4**, 489 (1997).
- [88] J. Ristein, Diamond Relat. Mater. **9**, 1129 (2000).
- [89] M. W. Geis and J. C. Twichell, Appl. Phys. Lett. **67**, 1328 (1995).
- [90] P. Gluche, A. Aleksov, A. Vescan, W. Ebert, and W. Kohn, IEEE Electr. Dev. Lett. **18**, 547 (1997).
- [91] Y. M. Wang, K. W. Wong, S. T. Lee, M. Nishitani-Gamo, I. Sakaguchi, K. P. Loh, and T. Ando, Diamond Relat. Mater. **9**, 1582 (2000).
- [92] F. J. Himpsel, J. A. Knapp, J. F. van der Veen, and D. E. Eastman, Phys. Rev. B **20**, 624 (1979).
- [93] J. B. Cui, J. Ristein, and L. Ley, Phys. Rev. Lett. **81**, 429 (1998).
- [94] P. K. Bachmann, D. Leers, and H. Lydtin, Diamond Relat. Mater. **1**, 1 (1991).
- [95] T. Ando, private communication.
- [96] P. E. Phersson and T. W. Mercer, Surf. Sci. **460**, 49 (2000).
- [97] R. E. Thomas, R. A. Rudder, and R. J. Markunas, J. Vac. Sci. Technol. A **10**, 2451 (1992).
- [98] G. Francz and P. Oelhafen, Surf. Sci. **329**, 193 (1995).
- [99] C. Bandis and B. B. Pate, Phys. Rev. B **52**, 12056 (1995).
- [100] L. Diederich, O. M. Küttel, E. Schaller, and L. Schlapbach, Surf. Sci. **349**, 176 (1996).
- [101] P. K. Baumann and R. J. Nemanich, Surf. Sci. **409**, 320 (1998).
- [102] L. Diederich, O. M. Küttel, P. Aebi, and L. Schlapbach, Surf. Sci. **418**, 219 (1998).
- [103] E. V. Albano, Applications Surf. Sci. **14**, 183 (1983).
- [104] J. Topping, Proc. Roy. Soc. (London) A **114**, 67 (1927).
- [105] K. Bogrov, H. Shechter, M. Folman, and A. Hoffman, Diamond Relat. Mater. **7**, 170 (1998).
- [106] J. Robertson and M. J. Rutter, Diamond Relat. Mater. **7**, 620 (1998).
- [107] R. C. Weast (Ed.), *Handbook of Chemistry and Physics* (CRC Press, Boca Raton, 1978).



- [108] C. Bandis and B. B. Pate, *Surf. Sci.* **350**, 315 (1996).
- [109] T. P. Humphreys, R. E. Thomas, D. P. Malta, J. B. Posthill, M. J. Mantini, R. A. Rudder, G. C. Hudson, R. J. Markunas, and C. Pettenkofer, *Appl. Phys. Lett.* **70**, 1257 (1997).
- [110] J. Bardeen, *Phys. Rev.* **71**, 717 (1947).
- [111] W. Schottky, *Z. Physik* **118**, 539 (1942).
- [112] N. F. Mott, *Proc. Camb. Philos. Soc.* **34**, 568 (1938).
- [113] W. Schottky, *Z. Physik* **113**, 367 (1939).
- [114] *Contacts to Semiconductors - Fundamentals and Technology*, edited by L. J. Brillson (Noyes Publications, Park Ridge, New Jersey, 1993).
- [115] R. T. Tung, in *Contacts to Semiconductors - Fundamentals and Technology*, edited by L. J. Brillson (Noyes Publications, New Jersey, 1993), Chap. 3 *Schottky barriers and ohmic contacts*, p. 176ff.
- [116] H. K. Henisch, *Semiconductor contacts - An approach to ideas and models* (Clarendon Press, Oxford, 1985).
- [117] Y. Mori, H. Kawarada, and A. Hiraki, *Appl. Phys. Lett.* **58**, 940 (1991).
- [118] A. F. Hollemann, E. Wiberg, and N. Wiberg, *Lehrbuch der anorganischen Chemie*, 100 ed. (Walter de Gruyter, Berlin, New York, 1985), p. 907ff.
- [119] M. Aoki and H. Kawarada, *Jpn. J. Appl. Phys.* **33**, L708 (1994).
- [120] K. Okano, H. Kiyota, T. Kurosu, and M. Iida, *Diamond Relat. Mater.* **3**, 35 (1993).
- [121] H. Kawarada, M. Aoki, H. Sasaki, and K. Tsugawa, *Diamond Relat. Mater.* **3**, 961 (1994).
- [122] O. M. Küttel, E. Schaller, J. Osterwalder, and L. Schlapbach, *Diamond Relat. Mater.* **4**, 612 (1995).
- [123] J. B. Cui, J. Ristein, M. Stammler, K. Janischowsky, G. Kleber, and L. Ley, *Diamond Relat. Mater.* **9**, 1143 (2000).
- [124] B. V. Christ, *Handbook of monochromatic XPS spectra series* (XPS International Inc., Kawasaki, 1999), Vol. 1: The elements and native oxides.
- [125] J. P. Sullivan, R. T. Tung, and M. R. Pinto, *J. Appl. Phys.* **70**, 7403 (1991).

- [126] W. Mönch, *Europhys. Lett.* **27**, 479 (1994).
- [127] S. G. Ri, T. Mizumasa, Y. Akiba, Y. Hirose, T. Kurosu, and M. Iida, *Jpn. J. Appl. Phys.* **34**, 5550 (1995).
- [128] J. Ristein, F. Maier, M. Riedel, M. Stammler, and L. Ley, *Diamond Relat. Mater.* **10**, 416 (2001).
- [129] B. Koslowski, S. Strobel, and P. Ziemann, *Appl. Phys. A* **72**, 311 (2001).
- [130] J. Ristein, W. Stein, and L. Ley, *Phys. Rev. Lett.* **78**, 1803 (1997).
- [131] C. Su and J. C. Lin, *Surf. Sci.* **406**, 149 (1998).
- [132] H. J. Looi, R. B. Jackman, and J. S. Ford, *Appl. Phys. Lett.* **72**, 353 (1998).
- [133] T. Anzai, *J. Mol. Struct.* **352/353**, 455 (1995).
- [134] N. B. Colthup, in *The Handbook of Infrared and Raman Characteristic Frequencies of Organic Molecules*, edited by D. Lin-Vien (Academic Press, San Diego, 1991), p. 478.
- [135] T. M. Miller, in *CRC Handbook of Chemistry and Physics*, edited by D. R. Lide and H. P. R. Frederikse (CRC Press, Boca Raton, Florida, 1995), pp. Table 10–180.
- [136] H. Gerischer, in *Physical Chemistry*, edited by H. Eyring (Academic Press, New York, 1970), Vol. 9A, p. 463.
- [137] A. J. Bard, R. Memming, and B. Miller, *Pure Appl. Chem.* **63**, 569 (1991).
- [138] A. F. Hollemann and E. Wiberg, *Lehrbuch der Anorganischen Chemie*, 90 ed. (W. de Gruyter, Berlin, 1976), p. 513.
- [139] A. L. Linsebigler, G. Lu, and J. T. Yates Jr., *Chem. Rev.* **95**, 735 (1995).
- [140] C. Sauerer, C. E. Nebel, and M. Stutzmann, presented at the 65<sup>th</sup> DPG-Conference on Solid States Physics, Hamburg, 2001 (unpublished).
- [141] J. Ristein, W. Stein, and L. Ley, *Diamond Relat. Mater.* **7**, 626 (1998).
- [142] C. Bandis and B. B. Pate, *Phys. Rev. Lett.* **74**, 777 (1995).
- [143] J. B. Cui, J. Ristein, and L. Ley, *Phys. Rev. B* **60**, 16135 (1999).
- [144] J. B. Cui, J. Ristein, and L. Ley, *Diamond Relat. Mater.* **9**, 1036 (2000).

- [145] E. O. Kane, Phys. Rev. **127**, 131 (1962).
- [146] B. Gan, C. Kerlit, Q. Zhang, J. Ahn, S. F. Yoon, J. Yu, Q. F. Huang, and V. A. Ligatchev, Phy. Stat. Sol. A **181**, 17 (2000).

# Publikationsliste

*Resonant magnetic scattering study of the 50% Ho-Tb alloy,*  
A. Stunault, C. Vettier, F. de Bergevin, F. Maier, G. Grubel, R.M. Galera,  
S.B. Palmer  
J. Magnetism Magn. Mater. **140-144**, 753 (1995).

*A simple design for a helium scattering apparatus,*  
F. Maier, S. Kneitz, H. Koschel, H.P. Steinrück,  
Surf. Sci. **377-379**, 1101 (1997).

*High-resolution surface-sensitive C1s core-level spectra of clean and  
hydrogen-terminated diamond (100) and (111) surfaces,*  
R. Graupner, F. Maier, J. Ristein, L. Ley, and C. Jung,  
Phys. Rev. B **57**, 12397 (1998).

*Electronic and atomic structure of the C-terminated 6H-SiC surface,*  
M. Hollering, B. Mattern, F. Maier, L. Ley, A.P.J. Stampfl, J. Xue, J.D.  
Riley, and R.C.G. Leckey  
Mat. Sci. For. **264-268**, 331 (1998).

*The hydrogenated and bare diamond (110) surface: a combined LEED-, XPS-,  
and ARPES-study*  
F. Maier, R. Graupner, M. Hollering, L. Hammer, J. Ristein, and L. Ley,  
Surf. Sci. **443**, 177 (1999).

*Electronic states of an ordered oxide on C-terminated 6H-SiC,*  
M. Hollering, F. Maier, N. Sieber, M. Stammler, J. Ristein, L. Ley, A.P.J.  
Stampfl, J.D. Riley, R.C.G. Leckey, F.P. Leisenberger, and F.P. Netzer,  
Surf. Sci. **442**, 531 (1999).

*Surface electronic properties of diamond,*  
J. Ristein, F. Maier, M. Riedel, J.B. Cui, and L. Ley,  
Phys. Stat. Sol. A **181**, 65 (2000).

*Origin of surface conductivity in diamond,*  
F. Maier, M. Riedel, B. Mantel, J. Ristein, and L. Ley,  
Phys. Rev. Lett. **85**, 3472 (2000).

*Electronic and atomic structure of an ordered silicate adlayer on hexagonal SiC,*

M. Hollering, N. Sieber, F. Maier, J. Ristein, L. Ley, J.D. Riley, R.C.G. Leckey, F.D. Leisenberger, and F.P. Netzer,  
Mat. Sci. For. **338-342**, 387 (2000).

*Spectroscopic investigations of diamond/hydrogen/metal and diamond/metal interfaces,*

F. Maier, M. Riedel, J. Ristein, and L. Ley,  
Diamond Relat. Mater. **10**, 506 (2001).

*Diamond surface conductivity measurements and photoelectron spectroscopy,*

J. Ristein, F. Maier, M. Riedel, M. Stammer, and L. Ley,  
Diamond Relat. Mater. **10**, 416 (2001).

*The electron affinity of plasma hydrogenated and chemically oxidized diamond (100) surfaces,*

F. Maier, J. Ristein, and L. Ley,  
submitted to Phys. Rev. B.

# Danksagung

Vielen Dank an alle, die zum Gelingen dieser Arbeit in vielfältigster Weise beigetragen haben.

Mein erster Dank gilt Prof. Lothar Ley für die Möglichkeit der Promotion an seinem Lehrstuhl, für seine intensive Betreuung in jeder Phase der Arbeit und für die gegenseitigen Sticheleien, die den Alltag immer wieder erfrischend gestaltet haben.

Ebenso möchte ich mich bei Dr. Jürgen Ristein für die freundschaftliche und gute Zusammenarbeit bedanken, und vor allem für seine Bereitschaft, mir bei experimentellen Problemen und theoretischen Fragestellungen immer mit Rat und Tat zur Seite zu stehen.

Ein ganz herzlicher Dank geht an Dr. Ralf Graupner, der mich zu Beginn der Arbeit in die geheimnisvolle Welt der Photoemission und der Halbleiterphysik eingeführt hat. Ich fürchte, ohne seine Hilfe wäre mir vieles über den Kopf gewachsen.

Ein großes Dankeschön an alle Freunde und Mitarbeiter hier am Institut, an der Universität und am Berliner Synchrotron BESSY I. Ihr Beitrag zu dieser Arbeit ist riesig!

Meinen Eltern, Geschwistern und Großeltern verdanke ich mehr, als ich hier aufzählen kann, vor allem aber das Gefühl der Sicherheit durch ihren unbedingten Rückhalt in allen Lebenssituationen.

Und schließlich bleibt noch meinem Mo für seine liebevolle Begleitung zu danken, die ich nicht mehr missen möchte.

# Lebenslauf

Name: Florian Maier

Geburtsdatum/-ort: 16.1. 1969 in Passau

Schulbildung: 1975 - 1988 Gymnasium Untergriesbach  
29.6.1988 Allgemeine Hochschulreife

Berufsausbildung: 1990 Beginn des Studiums der Physik an der Universität Würzburg  
7.9.1992 Vordiplom  
1992 - 1993 Auslandsstudium "Maitrise de Physique" an der Universität Joseph-Fourier in Grenoble, Frankreich  
1993 Viermonatiges Forschungspraktikum an der European Synchrotron Radiation Facility  
1993 - 1996 Hauptstudium Physik in Würzburg  
2.7.1996 Diplom  
Diplomarbeit bei Prof. Dr. H.-P. Steinrück  
Thema der Diplomarbeit:  
*Entwicklung einer einfachen Helium-Streueinheit zu Oberflächencharakterisierung - Aufbau und erste Untersuchungen an einer Ru(001) Oberfläche*

seit Sept. 1996 wissenschaftlicher Mitarbeiter am Institut für Technische Physik bei Prof. Dr. L. Ley, Erlangen

1996 - 2000 jeweils mehrwöchige Messzeiten am Berliner Elektronensynchrotron BESSY I

